BERGISCHE
UNIVERSITÄT
WUPPERTAL

Fakultät für Mathematik
und Naturwissenschaften

# Performance tests of depleted CMOS sensors for application at HL-LHC

## Dissertation

Christian Johann Riegel

Eingereicht am 27. April 2018

Verteidigt am 01. Oktober 2018

Die Dissertation kann wie folgt zitiert werden:

urn:nbn:de:hbz:468-20181205-110315-0
[http://nbn-resolving.de/urn/resolver.pl?urn=urn%3Anbn%3Ade%3Ahbz%3A468-20181205-110315-0]

*The only way to make sense out of change is to plunge into it, move with it, and join the dance.*

*Alan Watts*

# Contents

# 1. Introduction

The field of Elementary Particle Physics is the scientific discipline of the fundamental building blocks of nature and the forces between them. For more than a century, great theoretical and experimental effort has been leading to discoveries and has been increasing our understanding of nature. The Standard Model has been confirmed time and again with huge success and a large community is involved in searches and measurements to further deepen our understanding of nature.
Physics programs keep pushing technological boundaries, improving the performance of particle detectors in terms of precision and data collection rate. Silicon detectors have been an important component of modern tracking systems for several years. This technology is constantly improved and it seems not to have yet reached its final potential. Ambitious physics programs motivate upgrades of particle accelerators, resulting in increased requirements for detector components. Being in close proximity to particle collisions, tracking detectors operate in high-radiation environments with high track density.
Aside from particle physics, silicon sensors are a modern technology with a significant market-share in, for example, consumer-electronics. This offers opportunities to include commercial components in applications of particle physics. A **D**epleted **M**onolithic **A**ctive **P**ixel **S**ensor (DMAPS) technology produced in a **C**omplementary **M**etal-**O**xide **S**emiconductor (CMOS) imaging process is investigated as a promising alternative to more expensive and power-consuming hybrid pixel sensors. The main challenge of DMAPS is to ensure efficient operation over years of radiation exposure. This thesis describes the beginning of an R&D project to investigate DMAPS of a low-capacitance design, produced in the TowerJazz 180 nm technology and their potential for the new ATLAS **I**nner **T**rac**k**er (ITk).
A new setup was planned and built, focussing on a high timing resolution and a compact design to enable tests at facilities inside and outside of CERN.
The project started by testing sensors of a so-called standard process, and showed great performance and potential before irradiation. Unfortunately, severe degradation of sensor performance was observed after being exposed to radiation fluences comparable to the expectations in the outer layers of the ATLAS ITk and the sensors proved unsuitable for a high-radiation environment. In order to enhance radiation hardness, the process was modified by including an additional n-layer in the pixel. Performance parameters like charge-collection behaviour, hit-detection efficiency, signal rise time and charge sharing were investigated using different measurement methods. The impact of geometric design parameters were studied to optimise the performance. The knowledge gained in the presented R&D project was then used in the design of the next generation of test chips to further explore the limits of radiation-hard DMAPS.

This thesis is structured as follows: Chapter 2 introduces the Standard Model of Elementary Particle Physics as well as experiments of High Energy Physics. The basic principles of silicon detectors and of the CMOS technology as well as radiation damage in semiconductor sensors are described in Chapter 3. Further, the new ATLAS ITk, its requirements and different detector concepts are presented. Chapter 4 introduces the TowerJazz Investigator test chip and the process modification for enhanced depletion in high-radiation environments. Chapter 5 describes the Time-precision setup and presents results of validation studies. The performance of sensors produced in the standard process in laboratory and testbeam measurements before and after irradiation are presented in Chapter 6. The performance of sensors produced in the modified process are presented and compared in Chapter 7. The impact of the n-layer doping concentration on the detector performance is studied and presented in Chapter 8. Chapter 9 closes the thesis with a summary and an outlook on the next generation of test chips.

# 2. Standard Model and High Energy Physics experiments

The basis of the field of Elementary Particle Physics is the **S**tandard **M**odel of Elementary Particle Physics (SM). It describes the fundamental particles and their interactions, and is a very successful theory that has predicted particles even before their discoveries in **H**igh **E**nergy **P**hysics (HEP) experiments.
The elementary particles of the SM are shown in Figure 2.1. In the SM, the building blocks of matter form one group of half-integer spin particles; the fermions. The fermions themselves contain six different quarks, and six different leptons, organised in three generations with increasing mass. The time needed to discover all (currently) known fermions spans over a century from the discovery of the electron in 1897 [1] until the discovery of the tau neutrino in 2001 [2].

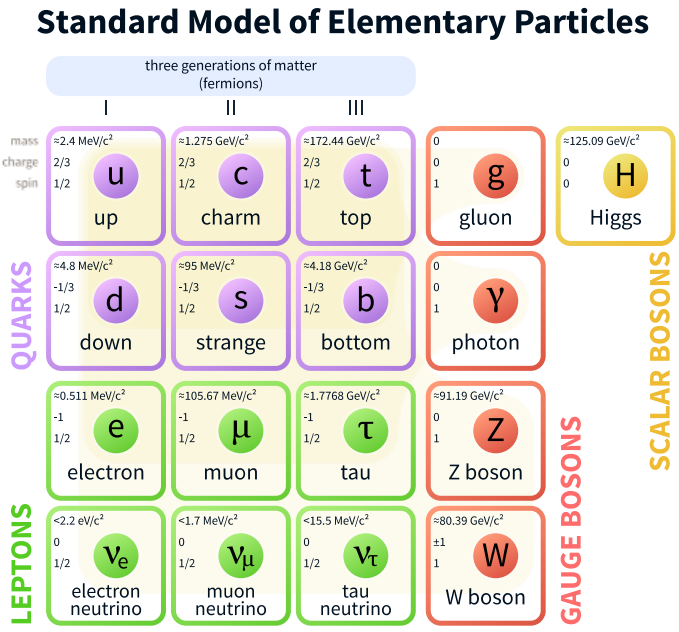


**Figure 2.1.** *In the Standard Model of Elementary Particle Physics, the fermions – quarks and leptons – are the building blocks of matter and the bosons transmit the fundamental interactions [3].*

As the fermions form the components of matter, another group of particles in the SM, the bosons, transmit the fundamental interactions. Bosons have an integer spin. The photon is the force carrier of the electromagnetic interaction, the $W^{\pm}$ and $Z$ gauge bosons are the force carriers of the weak interaction and the gluon is the force carrier of the strong interaction.

The fermions and heavy gauge bosons get their mass by electroweak symmetry breaking. A spin 0 particle is responsible for this effect: the Higgs boson. It was postulated in 1964 [4] but it took decades of intensive detector development and experimental effort leading to its discovery in 2012 [5, 6].
Despite its enormous success, the SM is not capable of providing explanations for all observations in nature. Examples for open questions are the matter–antimatter asymmetry in the universe and a dark matter particle. Furthermore, the fundamental force of gravity is not (yet) included in the SM.

Trying to answer these open questions experimentally requires the continuously improved measurement of parameters in the SM, such as coupling constants and particle masses, as well as the search for potential unknown particles in higher energy regimes. These searches can take decades and include intensive R&D effort regarding experimental setups and particle detectors. High-precision measurements and the hunt for rare particles and phenomena require precise detectors capable of recording a significant amount of data with increasing rate.

## 2.1. The Large Hadron Collider

The **L**arge **H**adron **C**ollider (LHC) is currently the most powerful particle accelerator on Earth and is located at the European Organisation for Nuclear Research CERN near Geneva, Switzerland. The LHC was built into the former tunnel of the **L**arge **E**lectron-**P**ositron Collider (LEP), which was in operation from 1989 to 2000, when it was closed to allow construction of the LHC [7].
The LHC tunnel is located underneath the border of Switzerland and France and has a circumference of 26.7 km. The LHC is the last element in the accelerator chain at CERN, shown in Figure 2.2. It receives its particles – protons or ions – from the **S**uper **P**roton **S**ynchrotron (SPS) at an energy of 450 GeV. In addition to the LHC, the SPS also provides particles for other experiments and for the SPS testbeam facilities used to test potential future detector technologies.
The particles in the LHC move in packages, so-called "bunches", inside two beam pipes in opposite directions. The four LHC experiments are constructed around interaction points at which the accelerated particles collide. At the interaction points, bunches cross and in case of a collision, new particles are created out of the center-of-mass energy of the interacting particles. For proton–proton collisions, the design energy of the LHC is 14 TeV. Up to $10^{11}$ protons per bunch are intended to collide 40 million times per second [8]. The particles created in these collisions as well as any decay products fly outwards and are measured by the particle detectors built around the interaction region.

During 2017, the LHC was operated at an energy of 13 TeV and exceeded its target by providing the ATLAS and CMS experiments with data corresponding to an integrated luminosity of 50 $\mathrm{fb}^{-1}$ [9].

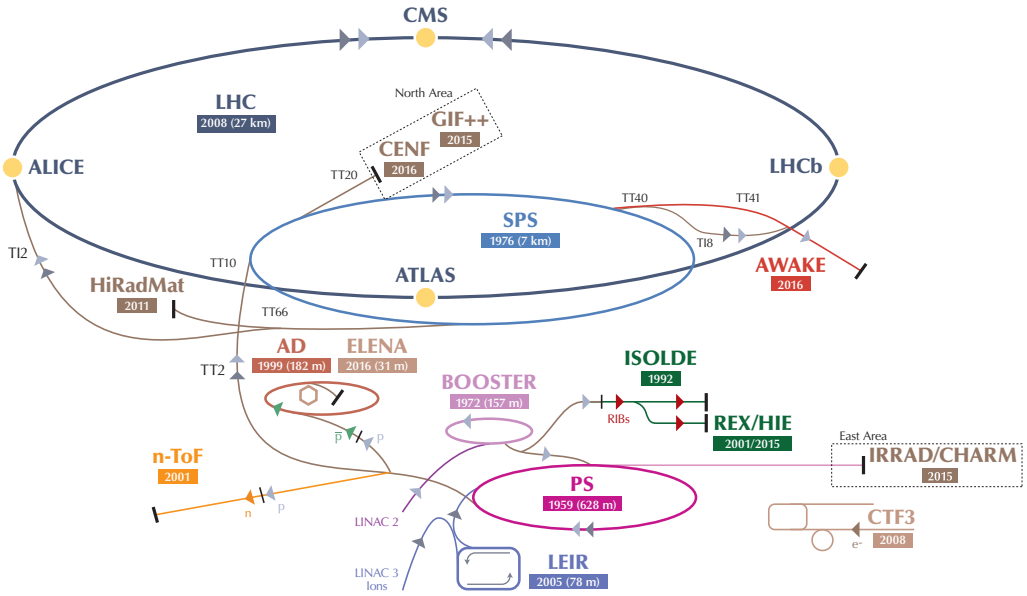


**Figure 2.2.** *The LHC is the biggest accelerator in the CERN accelerator complex. The four big experiments of the LHC are in clockwise order starting at Point 1: ATLAS, ALICE, CMS and LHCb [10].*

The inverse of the unit barn ($1\,\mathrm{b} = 10^{-28}\,\mathrm{m}^2$) is used to express the integrated luminosity:

$$L = \int_{t_0}^{t^1} f \cdot \frac{n_1 n_2}{4\pi\sigma_x\sigma_y} dt \tag{2.1}$$

In order to increase the number of potential collisions per bunch crossing, the collision frequency $f$ and numbers of particles per colliding bunch, $n_1, n_2$ for the two beams respectively, can be increased. A higher beam focus by reduction of the transverse bunch dimensions – given here as standard deviations in the horizontal and vertical directions $\sigma_x, \sigma_y$ – also increases the instantaneous luminosity [11]. The record of the instantaneous luminosity reached a value of $2.06{\cdot}10^{34}\,\mathrm{cm}^2\mathrm{s}^{-1}$, twice the nominal value [9].

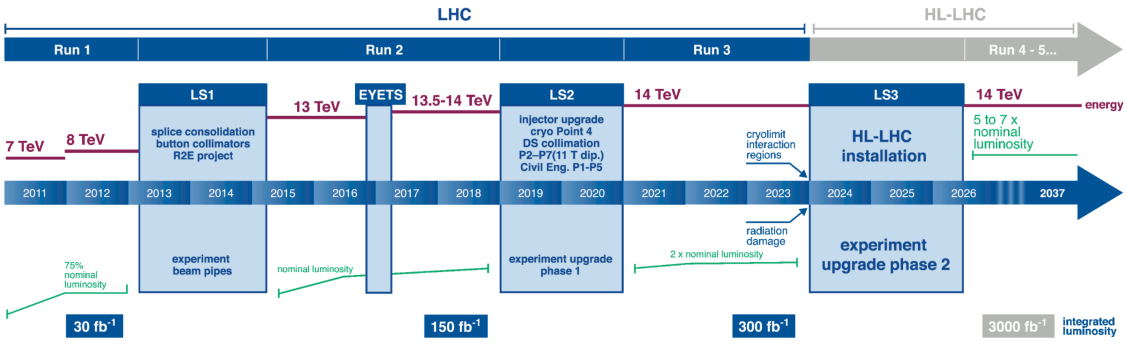


**Figure 2.3.** *LHC timeline with data taking periods – the so-called Runs – and long shutdowns [12].*

The outstanding performance of the LHC is based on the continuous effort of innovation and improvement. The schedule of the LHC program as set in 2012 is shown in Figure 2.3. The schedule contains data-taking periods, interrupted by **L**ong **S**hutdown (LS) periods planned for maintaining and upgrading the accelerator and the experiments.

The current data-taking period between LS1 and LS2 is called Run 2. The LHC is currently running at an energy of 13 TeV. The upcoming periods of LS2 in 2019/20 and LS3 starting at the end of 2023 with their corresponding upgrade plans will enhance the LHC further in terms of particle energy and luminosity. With LS3, the program of the **H**igh **L**uminosity **L**arge **H**adron **C**ollider (HL-LHC) will start and is planned to provide the experiments with higher instantaneous and integrated luminosity for their physics programs. The aim is a nominal luminosity of $5 \cdot 10^{34} \mathrm{cm}^2 \mathrm{s}^{-1}$ and thus increasing the total collected data ten-fold [12].

The increasing accelerator performance results in more demanding requirements for the experiments. The collaborations work intensively on crucial upgrade programs to cope with the higher particle rates and higher radiation levels in the future. R&D, production, integration and commissioning require several years of effort and the work presented in this thesis is part of the ATLAS R&D program for the HL-LHC.

## 2.2. The ATLAS detector

The biggest experiment operating at the LHC is the ATLAS detector. It is designed as a high luminosity experiment and multi-purpose detector, collecting high-statistic data in the search for new particles and the measurement of the properties of SM particles. The ATLAS detector is constructed in a barrel structure with concentric detector components. A cut-away view of its structure is given in Figure 2.4. The entire detector measures 25 m in diameter and 44 m in length [8]. The interaction point of the particle collisions is located at its center. Closest to the interaction point is the **I**nner **D**etector (ID) consisting of the **I**nsertable **B**-**L**ayer (IBL), the Pixel Detector, the **S**emi**c**onductor **T**racker (SCT) and the **T**ransition **R**adiation **T**racker (TRT). These layers are immersed in a solenoidal field of 2 T, bending trajectories of electrically charged particles and allowing measurements of their momentum.
Located outside of the tracking subdetectors of the ID are the electromagnetic and hadronic calorimeters. These provide energy measurements for particles using electromagnetic and hadronic interactions, respectively. The outermost components are the muon chambers.

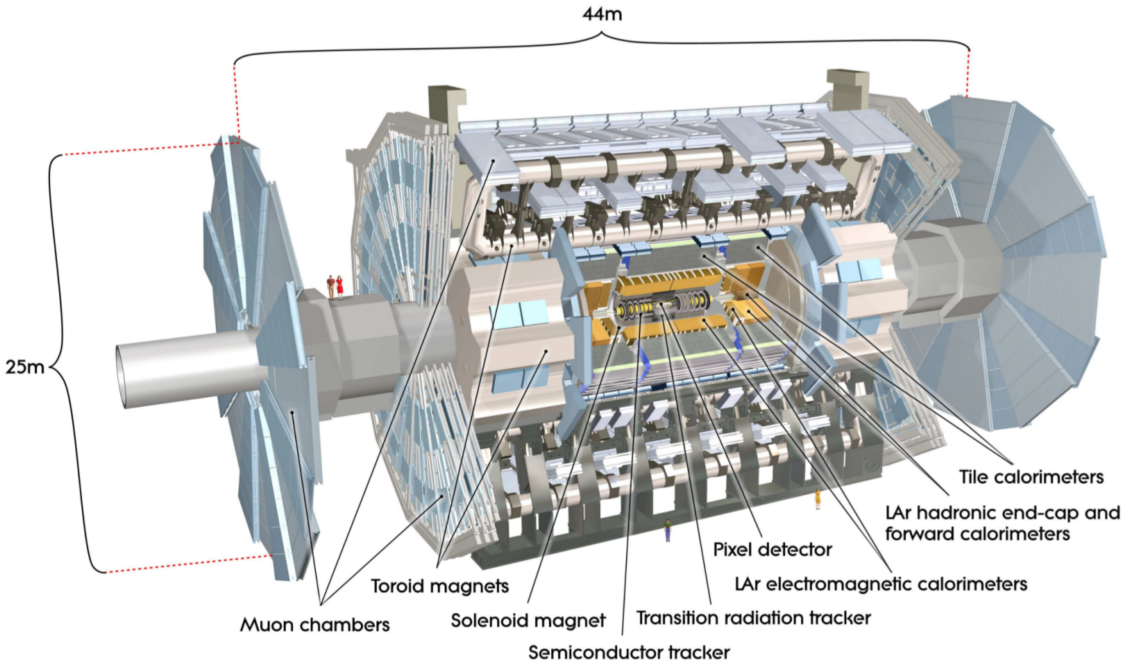


**Figure 2.4.** *The barrel structure of the ATLAS detector: The Inner Detector containing tracking layers is surrounded by electromagnetic and hadronic calorimeters. The outer-most components are the muon chambers. End-caps are added to provide full angular coverage [8].*

## 2.3. The ALICE detector

Another experiment at the LHC is **A** **L**arge **I**on **C**ollider **E**xperiment (ALICE). A cut-away view of its structure is given in Figure 2.5. The dimensions of the ALICE detector are a diameter of 16 m and a length of 26 m [13]. The detector consists of a barrel region with an **I**nner **T**racking **S**ystem (ITS) and two electromagnetic calorimeters (PHOS and EMCal). In addition, the ALICE detector is equipped with a forward muon arm at $2^\circ - 9^\circ$. The arm consists of absorbers, a dipole magnet and further tracking and triggering chambers.

The physics program of the ALICE collaboration focuses on strongly interacting matter, specifically on the properties of the quark–gluon plasma at high values of energy density and temperature, reproduced in nucleus–nucleus collisions, for example Pb–Pb. The program focuses on "physics at or close to midrapidity, that is, the region of lowest baryon density and maximum energy density", [13] which motivated the design of the forward muon arm.

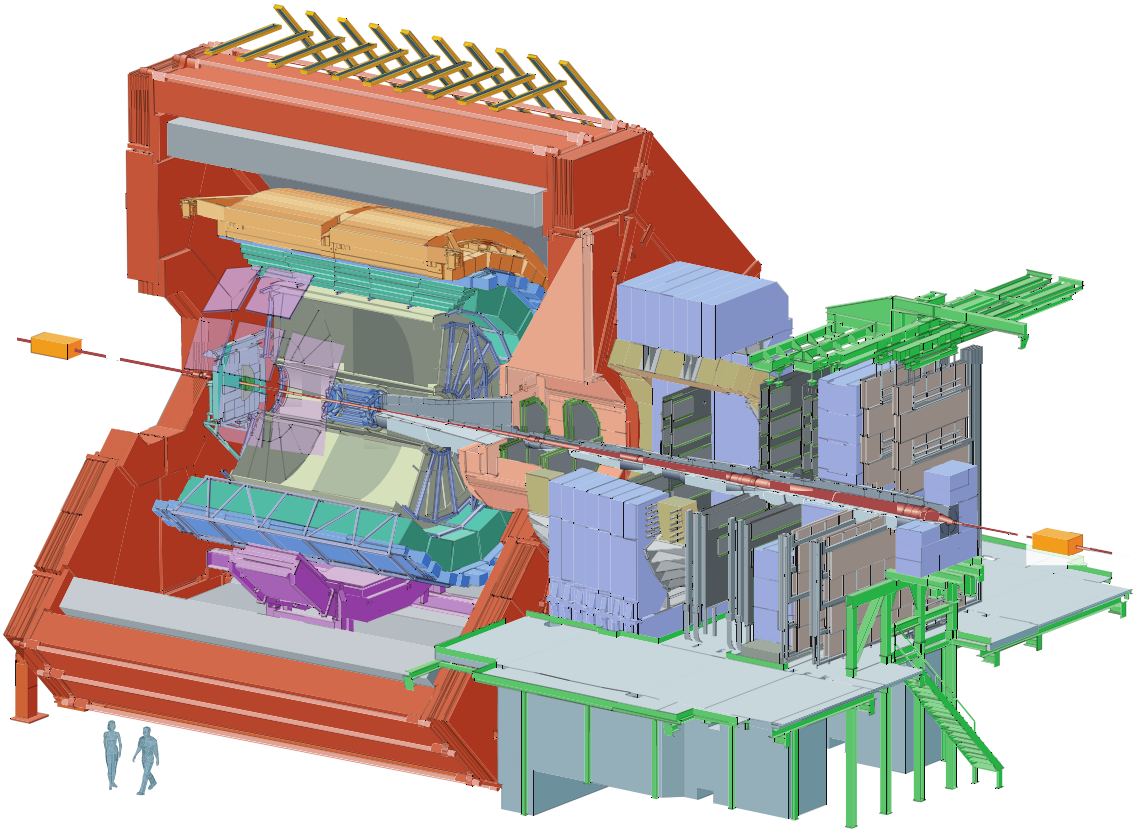

**Figure 2.5.** *The ALICE detector consists of a central barrel region and an additional forward muon arm [13].*

# 3. Particle detection with silicon detectors

Silicon is one of the most common elements in the crust of the earth, second only to oxygen. Silicon is also the fundamental component of modern technology, from consumer electronics to data applications to solar energy. The versatility of silicon is connected to its properties as a semiconductor. The electrical properties of silicon can easily be modified by adding different elements into the crystal structure.
In this chapter, first the properties and physical principles of doped silicon and a pn-junction are introduced. Then, the interaction of particles with matter and particle detection by segmentation are discussed. Furthermore, the consequences of radiation damage and the associated challenges for HEP experiments are discussed and different concepts of silicon detectors in HEP are compared. The mentioned topics are only covered briefly in this chapter, more profound presentations are available in literature, for example [14, 15, 16].

## 3.1. Silicon properties

Silicon is a semiconductor material, forming a regular lattice at room temperature. Its electrical properties are best described in the energy band structure which consists of a valence band, a conduction band and the band gap in between. Silicon is an element with four valence electrons that are bound in a lattice. The probability to excite charge carriers into the other band is negligible at room temperature and intrinsic (pure mono-elemental) silicon acts as an insulator due to the absence of charge carriers in the conduction band. This can be altered by creating additional energy levels in the band gap; a procedure called "doping". Doping can be performed in two directions: By adding elements with a higher number of valence electrons, this "donor impurity" leads to an excess of electrons and a so-called "n-type" doping. On the other hand, by adding elements with a lower number of valence electrons, the "acceptor impurity" leads to an excess of vacancies of an electron. These vacancies are called holes and behave like positive charge carriers. A material with this doping is "p-type" doped. Examples for additional energy levels are given in Figure 3.1. The energy needed to excite charge carriers from one band to the other is decreased, depending on the inserted impurity. The doping concentration can vary by several orders of magnitude, for example $10^{12} - 10^{20}\,\mathrm{cm}^{-3}$ [14], depending on the purpose of the doped volume.

In the case of thermal equilibrium at a given temperature $T$, each energy state $E$ has an occupation probability given by the Fermi–Dirac statistics:

$$f(E,T) = \frac{1}{e^{(E-E_F)/k_BT} + 1} \tag{3.1}$$

In Eq. (3.1), $k_B$ is the Boltzmann constant and $E_F$ is the Fermi level at which the probability of occupation is 0.5, meaning that exactly half of the levels are occupied. Doping of the silicon determines $E_F$ and influences the number of free charge carriers:

$$n = \int_0^{\text{inf}} D(E) \cdot f(E,T) \cdot dE \tag{3.2}$$

In this equation, $D(E)$ represents the density of states, the distribution of all levels up to the value of $E$. Since the free charge carriers are caused by doping, the concentration of the majority charge carriers – either electrons or holes – is identical to the dopant concentration.

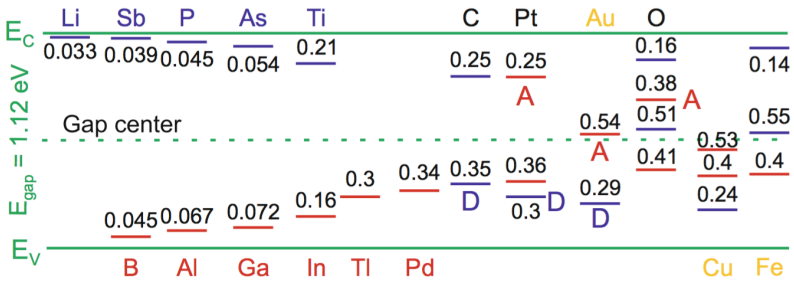


**Figure 3.1.** *Additional energy levels between valence band energy $E_V$ and conduction band energy $E_C$ created by acceptors (A) or donors (D): The excitation energy is reduced to lower values than $E_{gap}$= 1.12 eV, depending on the inserted impurity [14].*

### Mobility and drift velocity

The electrical resistivity $\rho$ of the material depends on the mobilities $\mu_e$ and $\mu_h$ of electrons and holes, and on their densities $n$ and $p$ as given in Eq. (3.3a). In case of a dominant dopant density $N_x$, it can be simplified to Eq. (3.3b)

$$\rho = \frac{1}{e(\mu_e n + \mu_h p)} \tag{3.3a}$$

$$\approx \frac{1}{e(\mu_x N_x)} \tag{3.3b}$$

The resistivity of pure intrinsic silicon at room temperature is around $\rho = 235\,\text{k}\Omega\text{cm}$. As given in Eq. (3.3b) this value can be significantly lowered by doping [14].
In silicon detectors, charges are created and collected. Therefore, mobility $\mu$ and drift velocity $v_D = \mu E$ in an electric field $E$ are important quantities. The mobility of charge carriers depends on the time $\tau_s$ between two scattering processes that take place at lattice vibrations and impurities in the form of doping atoms or crystal defects. Assuming highly pure silicon being used for the production of the sensor, intrinsic impurities and also the effects of the doping atoms are negligible. Then, crystal defects created by irradiation become the limiting factor for the sensor performance in the detector.

## 3.2. The pn–junction

The basic principle of a semiconductor sensor is a diode in reverse bias. Two differently doped volumes of a crystal create a pn-junction. In thermal equilibrium, the Fermi energy of both parts must be constant, leading to the creation of a **S**pace **C**harge **R**egion (SCR) in the connecting volume, as emphasised in Figure 3.2.

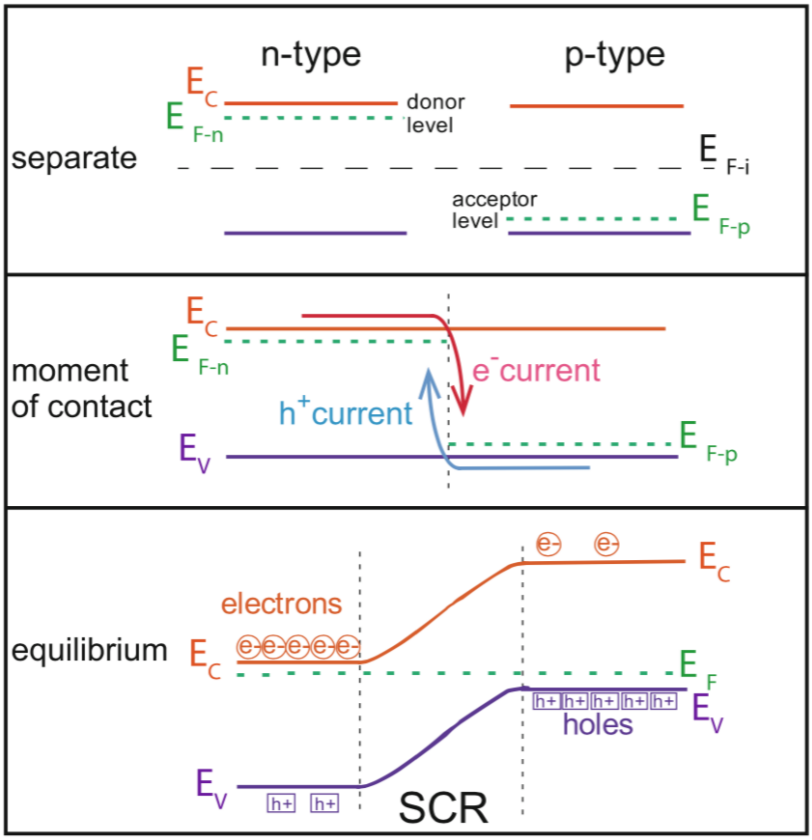


**Figure 3.2.** *The Fermi energies $E_{F-n}$ and $E_{F-p}$ differ due to doping in the separate materials. The free charge carriers move until an equilibrium is reached resulting in a constant Fermi energy over the pn-junction. The "moment of contact" is a theoretical picture since the regions are created in a single original crystal by different doping [14].*

Differences in potentials lead to a movement of the charge carriers – electrons move to the p-type material, holes to the n-type material – until an equilibrium with a constant Fermi energy is reached. The SCR is very localised at the contact area, but can be altered by applying an external voltage. Depending on the polarity of the voltage, the pn-junction can be in "forward" or "reverse" bias. In the first case, the barrier gets smaller and the charges can flow. In the latter case, the barrier gets higher and the pn-junction becomes insulating.This mode is used for silicon sensors. The concentration of intrinsic free charge carriers is significantly reduced, leaving only a leakage current caused by thermal excitation of charge carriers. In reverse bias it is insignificant for unirradiated sensors but increases with radiation-induced crystal defects.

## 3.3. Interaction of ionising particles with matter

Particle detection always demands an interaction between a particle and a detector. In the case of tracking detectors, charged particles are detected by ionising the detector medium, for example silicon. For this interaction of "intermediate range of moderately relativistic charged heavy particles" [17], the average energy loss is described by the Bethe formula given in Eq. (3.4) [14]:

$$-\frac{dE}{dx} = 4\pi N_A r_e^2 m_e c^2 z^2 \frac{Z}{A}\frac{1}{\beta^2} - \left[\frac{1}{2}\ln\left(\frac{2m_e c^2\beta^2\gamma^2 T_{max}}{I^2}\right) - \beta^2 - \frac{\delta(\gamma)}{2}\right] \tag{3.4}$$

Here, $N_A$ is Avogadro's number, $m_e$ and $r_e$ are the mass and the classical radius of an electron, $c$ is the speed of light, $\beta = v/c$, $\gamma = (\sqrt{1-\beta^2})^{-1}$ is the Lorentz factor and $\delta$ is a density effect correction. Further, $z$ is the integer charge number of the incident particle, $Z$ the atomic number of the medium, $A$ its atomic mass, $I$ is the mean excitation energy and $T_{max}$ is the maximum kinetic energy transferable to a free electron in one collision.
An example trend for muons traversing copper is shown in Figure 3.3. The intermediate region $0.1 \lesssim \beta\gamma \lesssim 1000$ is described by the Bethe formula. Faster particles have a shorter effective interaction time, leading to a dominating $\frac{1}{\beta^2}$ term for $\beta\gamma \lesssim 1$. For $\beta\gamma \gtrsim 10$, other effects start to dominate: More energy can be possibly transferred per single interaction and the transverse component of the electric field increases, leading to a higher impact parameter and a dependence of the $\ln(\beta^2)$ term [15].

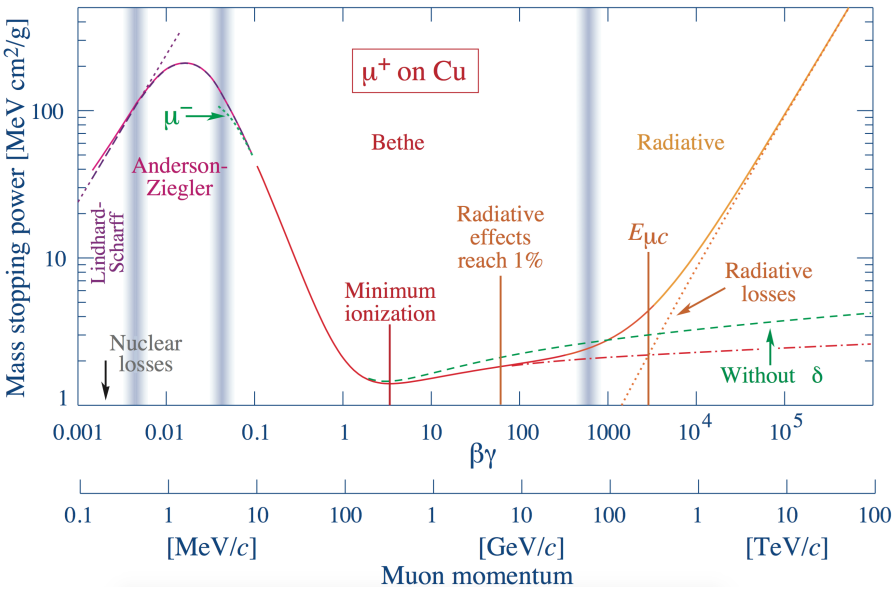


**Figure 3.3.** *Average energy loss of charged particles on the example of muons traversing copper. The deposited energy of MIPs is independent of the particle type but depends on the traversed material (Pb, Fe, Cu, ...) [17].*

Between both regions, the point of minimum ionisation at around $\beta\gamma = 3$ is of high importance for particle detectors.

Since **M**inimum **I**onizing **P**articles (MIPs) deposit the lowest amount of energy in the detector, it is important that their signals can still be detected above the background noise.

The energy is deposited in several collisions along the path of the particle through the medium and the total deposited energy is a statistical quantity, described by a Landau distribution as shown in Figure 3.4. The long tail to higher energies is caused by rare cases at which a large amount of energy is transferred to the medium. Due to these so-called $\delta$-electrons or $\delta$-rays, the maximum of the distribution, the **M**ost **P**robable **V**alue (MPV), is significantly lower than the average value.

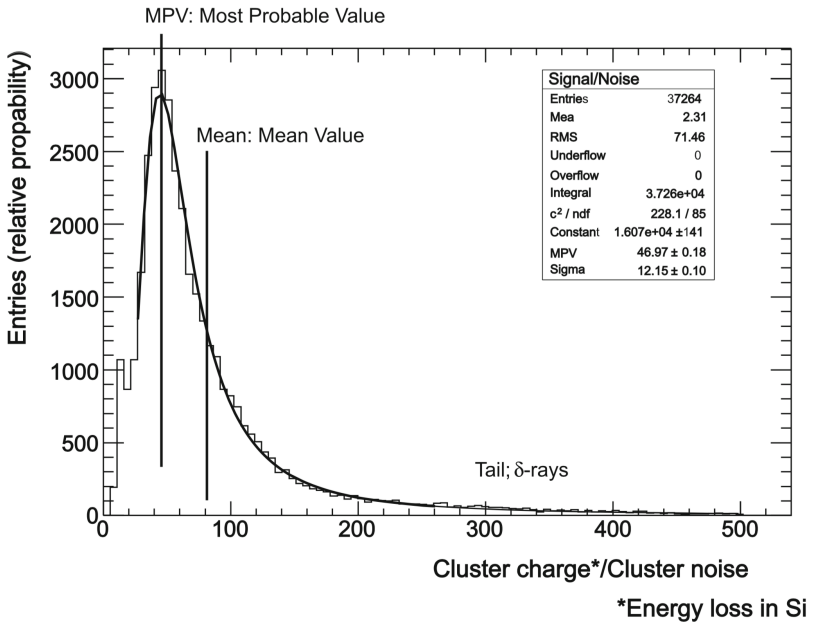


**Figure 3.4.** *Landau distribution of the total energy deposition along the path of the traversing particle [14].*

Aside from charged particles, also photons can ionise the sensor material. Three different kinds of interaction can be distinguished and their probabilities depend on the energy of the photon: In the first kind of interaction – the "Photoelectric effect" – the photon is absorbed by an electron bound to an atom, creating an electron–hole pair. For this, the photon energy must be slightly higher than the atom's ionisation energy. In the second case of a higher photon energy, the photon is "Compton scattered" on an electron, leading to the ionisation of the atom and the deflection of the photon. In the third case of the photon energy exceeding twice the center-of-mass energy of an electron, the photon can be transformed via "Pair production" into a pair of electron and positron.
Since the ionisation of the detector material is the main principle, the chosen material has an impact on the resolution of the detector. In silicon, 3.6 eV is the average energy to create an electron–hole pair, enabling a better energy resolution compared to the ionisation energy in gas detectors of 30 eV [14]. Furthermore, charges created in a gas detector need to be amplified whereas already the primary charges in a silicon detector are large enough to be detected.

## 3.4. Charge collection and Segmentation

The creation of ionisation charges in the silicon volume is also referred to as "deposition of charges" in the context of particle detection. In the case of a photon, a small localised charge cloud is created when the photon interacts completely with the material. In the case of a traversing particle, the charge cloud is stretched along the particle track trough the detector volume due to the statistical nature of multiple scattering processes. Although the term "charge collection" is used to describe the creation of the signal, it is actually the movement of charge carriers relative to the "collection electrode" which induces a signal [15]. The size of the signal depends on the amount of moving charges and the velocity of the movement. For an efficient collection, the depletion of the volume is of importance. When created inside a region with a strong electric field, these charge carriers drift in the electric field. Movement by drift is fast and therefore induces a high current signal.

When created in a non-depleted region of silicon, the charge carriers mainly move by diffusion. The disadvantages of "charge collection by diffusion" are a slower and less directed movement without common direction but along the density gradient. The induced signals are significantly lower. Due to the longer transport time, the charges are more likely to recombine with free intrinsic charges in which case the induction stops [14].

The purpose of tracking detectors is the determination of the particle position per sensor to reconstruct the particle trajectory in the entire tracker. In order to obtain the position information, semiconductor strip and pixel sensors contain a segmentation as motivated in Figure 3.5.

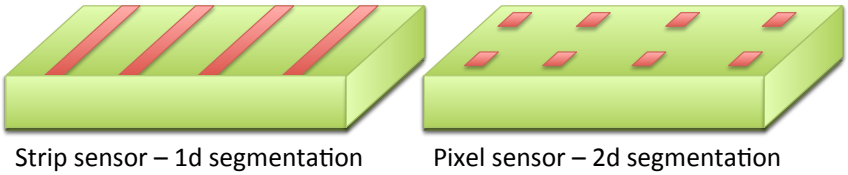


**Figure 3.5.** *By segmentation of the collection electrode into strips, 1d position information is obtained. By segmentation into pixels, 2d position information is obtained.*

In the case of a strip detector, long parallel electrodes are connected on one side of the sensor. The signal induction into specific electrodes provides one-dimensional position information about the particle hit. In the case of a pixel detector, the second spatial dimension is segmented as well and collection electrodes are positioned in regular distances, providing two-dimensional information.

## 3.5. Complementary Metal-Oxide Semiconductor (CMOS) technology

The foundation of modern microelectronics is the **M**etal **O**xide **S**emiconductor (MOS) structure. By controlled doping and oxidation, transistor structures are created as shown in Figure 3.6. Similar to bipolar transistors, different polarities – NMOS and PMOS structures respectively – are possible. Main difference is the type of charge carrier in the transistor: positive holes in PMOS and negative electrons in NMOS transistors. Areas of n-type doping in a p-type area serve as source and drain for an NMOS transistor (Figure 3.6a) and the opposite is used to create a PMOS transistor (Figure 3.6b). Commercial processes enabling both polarities on the same substrate are called CMOS. A "Full CMOS" chip is shown in Figure 3.6c. Areas of opposite doping – so-called wells – contain structures as seen by the n-well containing the PMOS transistor while being embedded in the global p-type substrate.

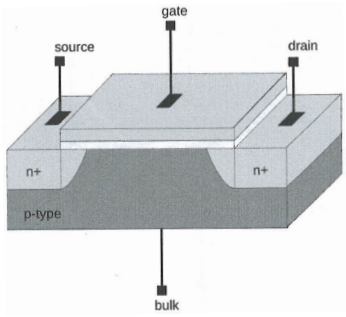


**(a)** *NMOS [18]*

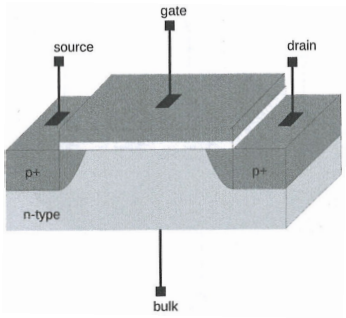


**(b)** *PMOS [18]*

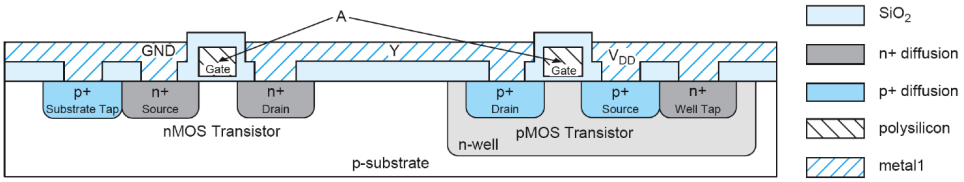


**(c)** *CMOS structure on a p-type substrate [19]*

**Figure 3.6.** *Individual NMOS (a) and PMOS (b) transistors can be combined to a CMOS structure (c). The p-type substrate contains an NMOS transistor on the left-hand side and a PMOS transistor in an n-well on the right-hand side.*

CMOS technology is both a well-established commercial product with applications in the entire range of modern electronics, and also a cutting-edge segment of economy with continuous improvement in miniaturisation and optimisation. More information on CMOS technology can be found in literature, for example in Refs. [18, 19].

## 3.6. Radiation damage of semiconductor sensors

Detectors of large, complex experiments are designed to be installed and then operated over a long period of time without being replaced. During this time, sensors are exposed to a high level of radiation in form of the charged particles they are meant to detect as well as electrically neutral particles. The radiation flux to which tracking detectors are exposed scale quadratically with their distance to the interaction point, differing significantly between the first layer only a few centimetres away and the tracker's outer layers.

Two different kinds of radiation effects on semiconductor detectors are distinguished.

- Damage of the crystal lattice in the bulk: Scattering of the traversing particles on the bulk atoms and the corresponding **N**on-**I**onizing **E**nergy **L**oss (NIEL) can result in both phonons and lattice deplacements.
- Damage of surface and interface layers: **I**onizing **E**nergy **L**oss (IEL) of charged particles and photons affect transistor structures and therefore readout electronics.

During operation, the detector is exposed to both effects at the same time. Charged, heavy particles like protons cause both effects to the material simultaneously and are also used to investigate this combined damage. In addition, separate measurements are a significant part of detector R&D to disentangle the effects [15].

### 3.6.1. Radiation damage in the bulk - NIEL damage

Since the interaction of the traversing particles is not limited to the electrons of the detector material, the lattice atoms are also affected by the particle flux. Electromagnetic and strong interactions between particles and nuclei lead to phonons and displace lattice atoms leading to vacancies and interstitials in the structure.

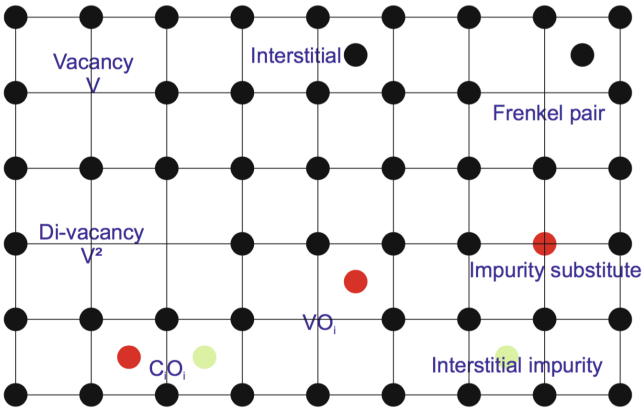


**Figure 3.7.** *Lattice defects caused by NIEL damage, lattice atoms and misplaced silicon atoms are shown in black, impurity atoms in colour [14].*

A selection of possible defects is shown in Figure 3.7. The non-ionising interaction can displace lattice atoms leading to vacancies (V) and interstitials (I). Since the energy levels of these states are less favourable than the pure lattice structure, these primary point-defects are not stable and lattice damages can recover (anneal) over time. But they can also form stable impurities in combination with present foreign atoms such as oxygen or phosphorus, which do not anneal over time [14, 15].

#### 3.6.1.1. The NIEL hypothesis

The creation probabilities of certain defects depend on both type and energy of the particle. Simulations of different particle beams are shown in Figure 3.8. In all three simulations, 10 MeV protons (a), 24 GeV protons (b) and 1 MeV neutrons (c), the hadrons have the same fluence of $10^{14}\,\mathrm{cm}^{-1}$. The neutrons produce more isolated dense clusters while the 10 MeV protons produce uniformly distributed point defects. The 24 GeV protons in the middle produce defects of a kind of intermediate configuration. The differences are caused by the different interactions between hadrons and silicon nuclei [20].

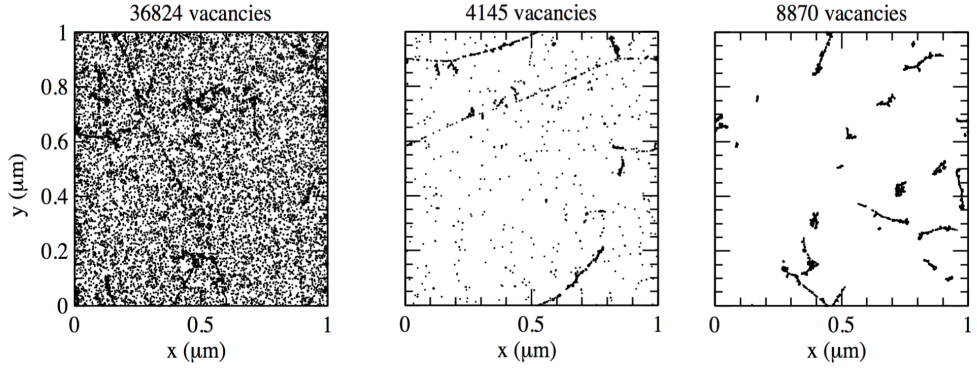


**(a)** *10 MeV protons* **(b)** *24 GeV protons* **(c)** *1 MeV neutrons*

**Figure 3.8.** *Initial vacancies over 1 µm depth of silicon material for a hadron fluence of $10^{14}$ $cm^{-2}$ produced by different particles and energies [20].*

According to the NIEL hypothesis, radiation damage in the bulk only depends on the transferred energy, independent of particle type and energy. The total displacement damage is given by:

$$D(E) = \sum_{\nu} \sigma_{\nu}(E) \int_{0}^{E_R^{max}} f_{\nu}(E, E_R) P(E_R) dE_R \tag{3.5}$$

The function is the sum over all possible interactions $\nu$, weighted by the cross–sections $\sigma_\nu(E)$ for a traversing particle of energy $E$. The function $f_\nu(E, E_R)$ gives the probability to transfer the recoil energy $E_R$ to a primary knock-on atom. The Lindhard partition function $P(E_R)$ [21] gives the fraction of the energy actually going into the displacement of the silicon atom.
This damage function is used to convert radiation damage caused by particles of a given energy into a common standard, the "1 MeV neutron equivalent fluence" $\Phi_{eq}$.

The value of the damage function this standard is $D_{neutron}(1\text{MeV}) = 95\,\text{MeV mb}$. By comparing the actual damage of a given irradiation fluence $\Phi = \int \Phi(E)dE$ with the 1 MeV neutron equivalent fluence, a numerical "hardness factor" $\kappa$ is defined as given in Eq. (3.6a) which is then used to calculate $\Phi_{eq}$ for each irradiation [14]

$$\kappa = \frac{\int D(E)\Phi(E)dE}{95\,\text{MeVmb} \cdot \Phi} = \frac{\Phi_{eq}}{\Phi} \tag{3.6a}$$

$$\Rightarrow \Phi_{eq} = \kappa\Phi \quad . \tag{3.6b}$$

The unit of the 1 MeV neutron equivalent fluence is $[\Phi_{eq}] = n_{1\text{Mev}}/\text{cm}^2$ but is often also referred to as $n_{eq}/\text{cm}^2$ or simply $n/\text{cm}^2$. All irradiation fluences in this thesis are given in values of 1 MeV neutron equivalent fluence.

The NIEL hypothesis provides the possibility to compare bulk damage caused by different irradiations. Apart from this, it also enables the practical investigation of long–term irradiation damage. Since the dominant parameter determining the damage is the transferred energy, independent of the time scale of the transfer, ageing and degradation of the sensor can be accelerated. The basic principle of irradiation campaigns is based on sensors being exposed to high irradiation fluences in a short amount of time to investigate the detector performance after years of operation. Bulk damage anneals over time due to thermal diffusive movements in the lattice and the annealing is significantly reduced in cold environments. Radiation hardness of a sensor is investigated by irradiation to a certain fluence and then storing and handling the sensor cooled to preserve the caused damage.

#### 3.6.1.2. Effects of NIEL damage

Point defects and lattice damages of the bulk change the properties of the semiconductor material over time and influence the detector performance [15].

**Microscopic effects on the detector material** All types of lattice defects populate new energy levels inside the band gap and change the properties of the semiconductor material. This can lead to different microscopic effects inside the bulk as summarised below.

- The newly created acceptors or donors can change the effective doping concentration. It is even possible for the material to change the doping type from n-type to p-type by removing electrons from the valence band, binding them in created acceptors.
- At niveaus close to or in the middle of the band gap, electron–hole pairs are generated thermally or leave the bands and recombine. The generation directly changes the corresponding concentrations and increase the leakage current of the substrate. In the worst case, the higher leakage current raises the temperature of the crystal which increases the thermal generation of electron–hole pairs. This positive feedback loop is called "thermal runaway" and can cause the destruction of the detector cell.

**Macroscopic effects on detector performance** Bulk damages and newly created energy levels lead to macroscopic effects on the overall detector performance.

- Apart from the danger of a thermal runaway, the increasing leakage current affects the **S**ignal-to-**N**oise ratio (S/N) in the cell and limits possible thresholds for particle detection.
- If the trapping time exceeds the signal shaping time, the signal is lost. The charge then instead increases noise during subsequent readout cycles.
- The creation of additional acceptor levels influences the depletion of the charge-collection volume. Changes in the doping concentration effect the electric field and can endanger the complete depletion. In combination with an increased trapping probability, this significantly reduces the performance of the detector.

### 3.6.1.3. Depletion after irradiation

Depletion of the collection volume is one key mechanism to ensure charge collection and charge-collection efficiency after irradiation. The bias voltage needed to deplete a certain depth $d$ depends on the effective space charge concentration. An example for the voltage needed to deplete $d$=300 µm of n-type silicon is given in Figure 3.9. Before type inversion, the voltage needed to deplete the n-type material decreases with particle fluence until reaching an intrinsic level. After type inversion, the voltage needed to deplete the p-type material increases again. If possible, adapting the bias voltage is used to counter NIEL damage in the bulk and maintain high charge-collection efficiency in the sensor. Depending on technology and sensor design, the bias voltage might be limited to protect the device.

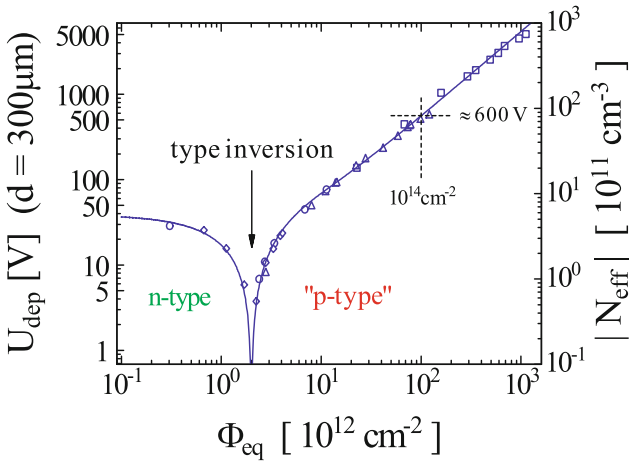


**Figure 3.9.** *The development of the effective space charge concentration (right y-axis) and bias voltage needed to deplete d=300 µm (left y-axis) show a minimum at type inversion. Before irradiation the bulk is n-type material [14].*

### 3.6.2. Radiation-induced surface damage - IEL damage

In addition to the damage in the bulk, radiation also effects $SiO_2$ surfaces and $SiO_2$-Si interface layers, present in AC coupled sensors and in the NMOS and PMOS transistors of the electronics. The IEL damage is not caused by interaction with the atomic nuclei and lattice displacements but by ionisation and the creation of electron–hole pairs. Unlike in the silicon bulk, strong electric fields and the properties of the insulating layers can prevent recombination completely. The mobility of the holes is especially low, leading to an accumulation of positive charges at the interface. The accumulated effect is expressed and investigated as **T**otal **I**onising **D**ose (TID). The additional charges effect the threshold voltage, leakage current and transconductance of the MOS transistors and can even create parasitic transistor structures. Concerning the sensor performance, IEL damage leads to an increase of noise and cross-talk between strips and pixels. It also affects the electronics of the detector with the risk of false signals and logic failure [14, 15].

More detailed information on IEL damage can be found in Ref. [22, 23, 24]. In the context of this thesis, only NIEL damage in the bulk was investigated. IEL damage is best investigated on either very simple structures, for example, separate test transistors resembling the transistors in the electronics, or on specific structures similar to a final electronics design. The test chip used in the context of this thesis consists of several very different substructures and therefore contains a level of complexity not suited to investigate IEL damage. The chip is presented in further detail in the next chapter.

### 3.6.3. ATLAS semiconductor tracking system

With exception of the TRT, which consists of tubes filled with gas, all sensors of the current ATLAS ID are silicon–based. In the case of IBL and Pixel Detector, pixelated sensors at known radial positions are used to obtain high position resolution in the remaining directions, parallel and perpendicular to the longitudinal $z$-axis of the detector. In the case of the SCT, silicon strips are used. Two strip sensors are used together per SCT layer to obtain position information in both directions.

The ATLAS Pixel Detector started its operation in 2008 and consists of three barrel layers. The radial positions of the barrel layers are shown in Figure 3.10. The innermost Barrel Layer 0 has a distance of $R_0 = 50.5\,\text{mm}$ to the interaction point in the middle of the beam pipe. The other two layers are positioned at a distance of $R_1 = 88.5\,\text{mm}$ (Barrel Layer 1) and $R_2 = 122.5\,\text{mm}$ (Barrel Layer 2). In total, the Pixel Detector contains 1744 identical pixel sensors with a nominal pixel size of $50\times400\,\mu\text{m}^2$ and has over 80 million pixels [8, 25].

The measured sensor thickness is $(256 \pm 3)\,\mu\text{m}$ and the sensors are biased with 150 V. The spatial resolution was determined in testbeam measurements to be $10\,\mu\text{m}$ in the direction of the $50\,\mu\text{m}$ pitch and to be $115\,\mu\text{m}$ in the direction of the $400\,\mu\text{m}$ pitch. The Pixel Detector typically provides three measurement points for particles from the interaction point up to $|\eta| = 2.5$ [26].

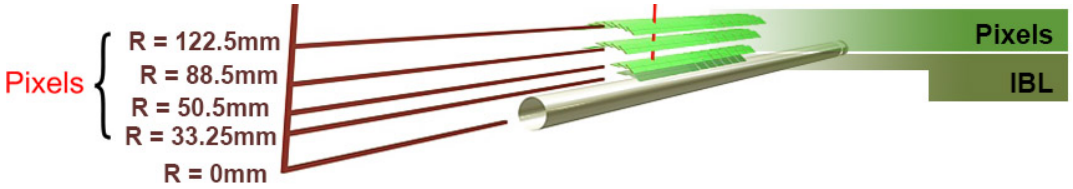


**Figure 3.10.** *The barrel layers of the Pixel Detector are concentric in radial distances of* $R_0 = 50.5\,\text{mm}$*,* $R_1 = 88.5\,\text{mm}$ *and* $R_2 = 122.5\,\text{mm}$*. The IBL is glued on the beam pipe in an average distance of* $R_{\text{IBL}} = 33.25\,\text{mm}$ *[27].*

During LS1, the IBL was installed as additional layer of pixel sensors. By replacing the original beam pipe with a new and smaller version, the additional insertion had been made possible. The IBL contains fourteen staves in a turbine structure around the interaction point of ATLAS. The center of the IBL sensors have a distance of $R_{\text{IBL}} = 33.25\,\text{mm}$ to the interaction point as indicated in Figure 3.10. The pixels of the IBL have a size of $50{\times}250\,\mu\text{m}^2$ which provides a distinct improvement in the longitudinal direction compared to $50{\times}400\,\mu\text{m}^2$ of the Pixel Detector pixels [28].

## 3.7. The new ATLAS Inner Tracker (ITk)

Operating the ATLAS detector at the HL-LHC will require a new tracking system. The current ID will be replaced entirely during LS3 by the new ATLAS ITk, an all-silicon based tracking system to ensure a similar tracking performance in the challenging high-occupancy environment of the HL-LHC, capable of coping with the approximately ten–fold integrated radiation dose compared to Phase 1 [12].

Like the current ID, the ITk will consist of different sub-detectors, having five layers of silicon pixel sensors around the center and four layers of silicon strip sensors further out, extending up to the inner bore of the solenoid. The ITk will be 6 m long and take up all the space of the current ID – IBL, Pixel, SCT, TRT – inside the solenoid field of 2 T, bending the trajectory of charged particles. The layout of the ATLAS ITk Pixel Detector is shown in Figure 3.11. The sensors of the barrel region are shown in red, the outer modules being inclined to allow for two or more hits in the innermost layer. In addition, the high-eta range is covered by several end–caps shown in dark red.

### 3.7.1. Requirements

The development of the ATLAS ITk is necessary to not only replace the current ID but also to build a tracking system capable of coping with HL-LHC requirements. Over the operation time of the HL-LHC, an additional $2500\,\text{fb}^{-1}$ is aimed to be delivered to the ATLAS detector.

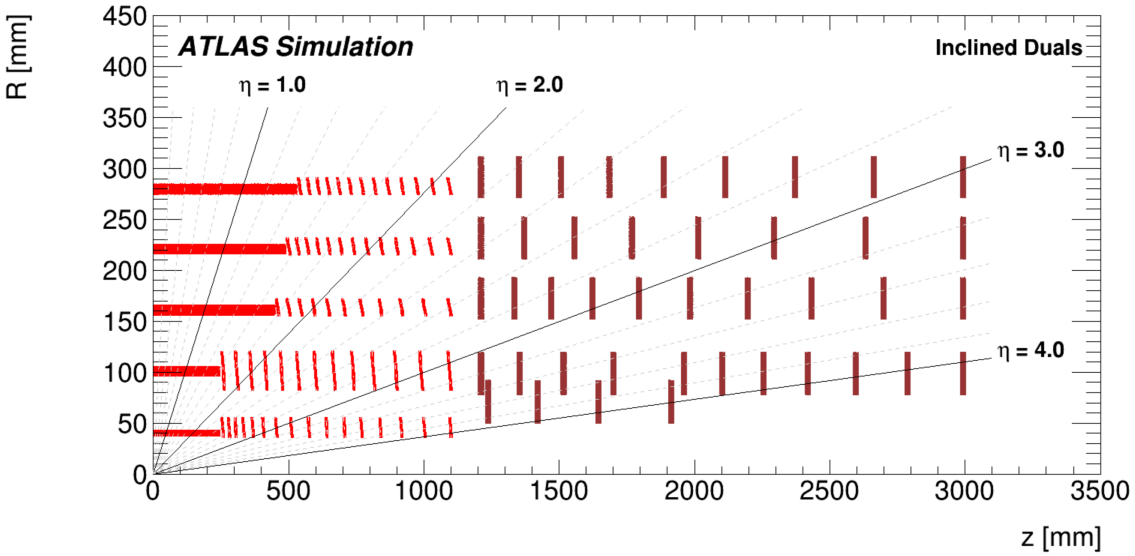


**Figure 3.11.** *Possible layout of the ATLAS ITk, covering a pseudorapidity range up to $|\eta|$ =4. The silicon Pixel Detector is shown in brown, the silicon strip detector is shown in blue [29].*

The increased instantaneous luminosity leads to an increase of pile-up (number of proton–proton interactions per bunch crossing) to around $\mu$=200. A high pile-up environment over years of operation is a severe challenge concerning the radiation hardness of the inner tracking system. On the other hand, the material budget of the sensor layers is to be kept as low as possible to reduce multiple scattering of the particles.

### Pixel size

The size of the pixels has direct impact on the resolution of the detector. A reduction results in a higher granularity and a better position determination of the particle trajectory. As mentioned, the pixel dimensions of the IBL are $50\times250\,\mu m^2$. For the ITk Pixel Detector, dimensions of $50\times50\,\mu m^2$ or $25\times100\,\mu m^2$ are considered [29]. Apart from the improvement in resolution, this helps avoiding the merging of clusters and reducing the occupancy regarding the increase of pile-up events.

### Timing

The LHC operates at a 25 ns bunch crossing interval, relating to 40 million beam–beam interactions per second. Since particle hits have to be assigned to a specific bunch crossing, the interval of 25 ns is a broad upper limit for the timing resolution the detector has to achieve.

Regarding the performance of a single pixel cell, this requires the analogue collection of charges, the processing and a reset of the cell to happen within this time budget so that the pixel is ready for the next bunch crossing. In case of a longer dead time of the pixel cell, the hit-detection efficiency might decrease, depending on the hit rate of the particular layer.

### Radiation hardness

The transition from LHC to HL-LHC operation includes a severe increase of radiation. Being placed directly around the beam pipe and the interaction point, the requirements are highest in the ATLAS ITk. A simulation of the expected 1 MeV neutron equivalent fluence, normalised to 3000 $fb^{-1}$ is shown in Figure 3.12.

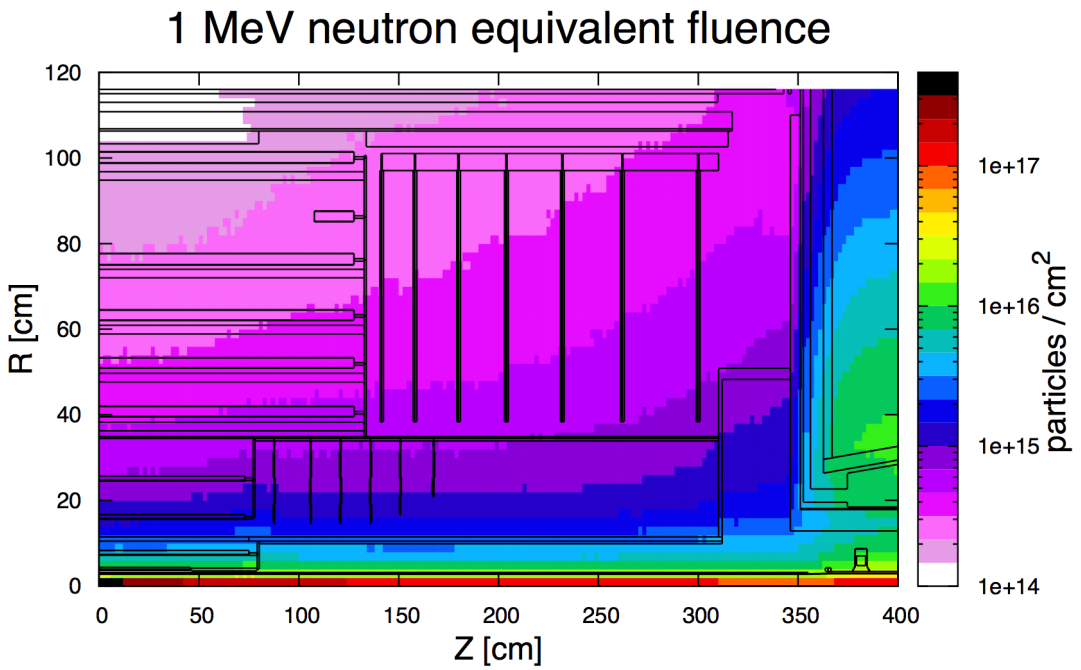


**Figure 3.12.** *Expected 1 MeV neutron equivalent fluence in the ATLAS ITk, generated using PYTHIA8 and normalised to 3000 $fb^{-1}$. For the outer pixel barrels, the maximum fluence is 1.7×$10^{15}$ $n/cm^2$ [30].*

Due to the inverse-square law, the radiation requirements differ between sensors on the inner layers ( R < 6 cm ) and on the outer layers ( R > 26 cm ). Sensors in the center of the innermost pixel layer need to tolerate a NIEL damage of 1.4x$10^{16}$ $n/cm^2$ and a TID of 7.7 MGy as IEL damage. Sensors in the outer pixel layers need to tolerate 1.7x$10^{15}$ $n/cm^2$ and 0.9 MGy, respectively [30].

## 3.8. Detector technologies

Although the principle of particle detection – creating electron–hole pairs in a semiconductor volume and detecting the induced current – stays the same, increasing requirements in applications demand ongoing technological effort and result in different detector concepts [16]. A schematic emphasising such concepts is presented in Figure 3.13.

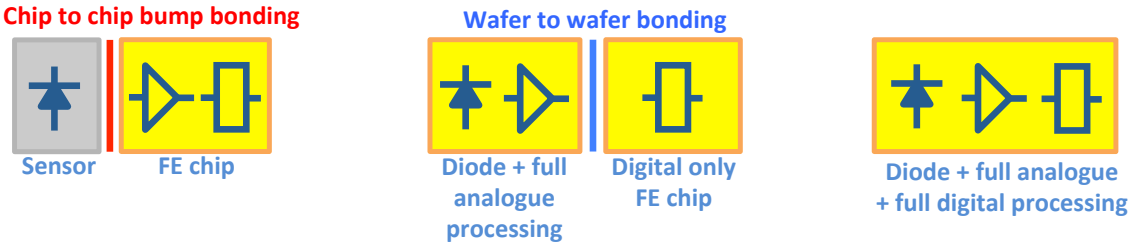


**(a)** *Passive sensor* **(b)** *Active sensor* **(c)** *Monolithic*

**Figure 3.13.** *The currently used detector concept consists of a passive sensor and a connected FE chip (a). Some R&D projects are ongoing to include analogue processing into the sensor (b). In a monolithic sensor all processing is included in the sensor and a separate readout chip becomes obsolete (c). (Pictures based on [31])*

### 3.8.1. Hybrid detectors

The pixel-sensor architecture used in the current ATLAS Pixel detector is based on hybrid pixel sensors as indicated in Figure 3.13a. A cross–section of a single hybrid pixel is given in Figure 3.14a. The depleted bulk is located in the passive sensor on top while the readout circuitry is located in the separate readout chip below. Signals are transmitted via solder bumps between the chips. Both chips are pixelated with equal pixel sizes and form a pixel matrix as shown in Figure 3.14b. The bias voltage – also called **H**igh **V**oltage (HV) – is connected externally to the passive sensor and therefore does not interfere with the electronics in the other chip.

Hybrid pixel sensors have shown outstanding performances in operation and the capabilities to cope with high particle rates while also being radiation hard. Given experience and known performance, they are the baseline choice for the new ATLAS ITk. The separation of tasks into two different entities allows for individual optimisation of sensor (regarding radiation hardness of the bulk) and readout chip (regarding processing rate).

Hybrid pixel sensors have their disadvantages. Consisting of two separate components, the sensors represent a relatively large material budget in the innermost part of the detector. In addition to the production of both components, a custom process is needed to connect them to one assembly.

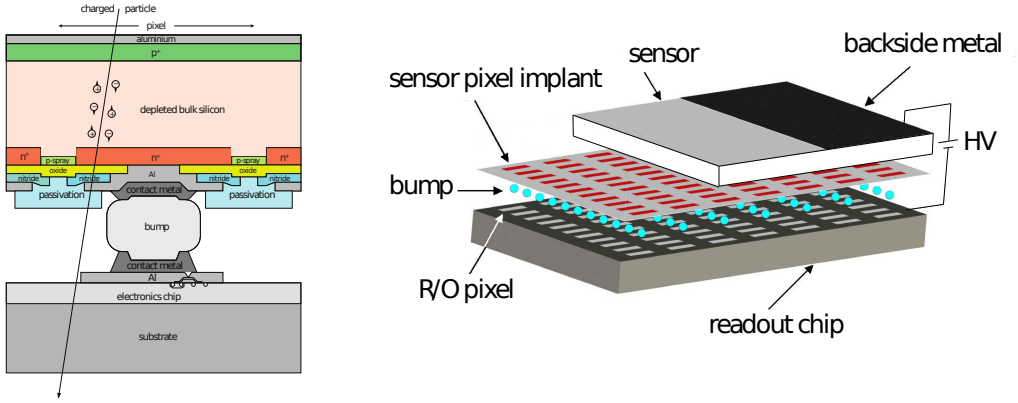


**(a)** *Hybrid pixel* **(b)** *Hybrid pixel matrix*

**Figure 3.14.** *For each individual pixel cell (a) of a hybrid pixel sensor, the charge collection volume is located in the passive sensor bulk (here on top). All readout circuitry is located in a second chip (here at the bottom) connected via solder bumps. Having equally sized pixels, sensor chip and readout chip form a hybrid pixel matrix (b). Per pixel, one bump-bond is needed [22].*

Since each pixel has to be connected individually with the corresponding circuit of the readout electronics, small solder balls – so-called bump-bonds – are placed according to the pixel pitch [22].

The total area size of the future ATLAS ITk and the resulting costs for an all-hybrid detector of the current design led to an R&D program for the investigation of alternative technologies based on commercial processes and their potential as radiation-hard pixel sensors. A general idea is the use of commercial CMOS technology. In one concept indicated in Figure 3.13b, a so-called active sensor also contains the full analogue processing. By including a first amplification stage into the active sensor, the requirements on the interconnection to the digital readout chip decrease. The output signal – after hit processing in the active sensor – can be large enough to be transmitted via capacitive coupling over a thin layer of glue, making solder bump-bonds obsolete.
In this case, not individual chips but entire wafers are bonded together. This procedure reduces costs but introduces higher requirements in placing precision compared to bump-bonding. Other potential issues are the uniformity of the glue-layer thickness which directly influences the coupling of both chips and the performance of the final detector [31].

### 3.8.2. Monolithic Active Pixel Sensors (MAPS)

Following the idea of implementing functionality into the sensor eventually leads to a **M**onolithic **A**ctive **P**ixel **S**ensor (MAPS) concept as indicated in Figure 3.13c. In MAPS, a silicon substrate serves as charge collecting volume while all circuitry – analogue as well as digital – is implanted at the top side of the chip using commercial CMOS production processes.

Developed for and driven by commercial applications, modern CMOS imaging processes offer many properties advantageous for HEP particle detectors: The relatively thin collection volume in a monolithic chip results in a small material budget and low multiple scattering. At the same time, the high density of CMOS circuitry enables very small pixel sizes resulting in a high position resolution.

A MAPS cross-section is given in Figure 3.15. On top of a low ohmic p-type substrate a grown epitaxial layer contains the CMOS circuitry while at the same time serving as charge-collection volume. The CMOS circuitry limits the biasing voltage of the bulk, so that especially a low ohmic epi-layer is not depleted except in the near surroundings of the collection electrodes. The dominant collection process is charge transport by diffusion, resulting in slow signals and limited radiation hardness. PMOS-hosting n-wells need to be shielded by deeper layers as shown. Otherwise they act as competing collecting nodes resulting in charge loss [22].

MAPS are not a completely new concept but already a technology used in HEP. Experiments with significantly lower requirements than the ATLAS ITk implemented the technology, for example, STAR [32] and the upgrade of the ALICE tracking system [33, 34]. The R&D project presented in this thesis for the ATLAS ITk evolved of the ALICE R&D process. Details are given in the next chapter.

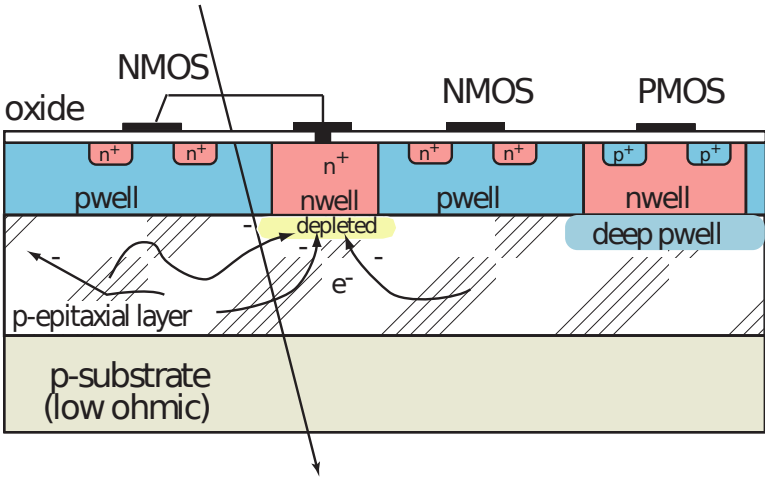


**Figure 3.15.** *Monolithic Active Pixel Sensor: A grown epitaxial layer contains the CMOS circuitry while serving as charge-collection volume [22].*

### 3.8.3. Depleted Monolithic Active Pixel Sensors (DMAPS)

As mentioned earlier, the key to tackle radiation hardness and detection time is to fully deplete the charge collection volume. Inside a depleted volume, charges are transported by drift and due to the high velocity less effected by radiation-induced trapping. R&D projects trying to enhance MAPS for high-radiation environments led to the design of DMAPS and their further developments [35].

As mentioned, the depletion capability depends on biasing limitations caused by the included CMOS circuitry. The relation between depletion depth $d$, substrate resistivity $\rho$ and bias voltage $V$ is

$$d \sim \sqrt{\rho V} \tag{3.7}$$

which implies that a significant depletion depth for charge collection can be achieved by increasing the resistivity of the substrate and by increasing the bias voltage. The foundries offer high resistivity substrates in the kΩcm range, enlarging the depletion depth. Since full CMOS functionality is desired, NMOS and PMOS structures need to be protected from the applied bias voltage. This is achieved by multiple nested wells as seen in Figure 3.16.

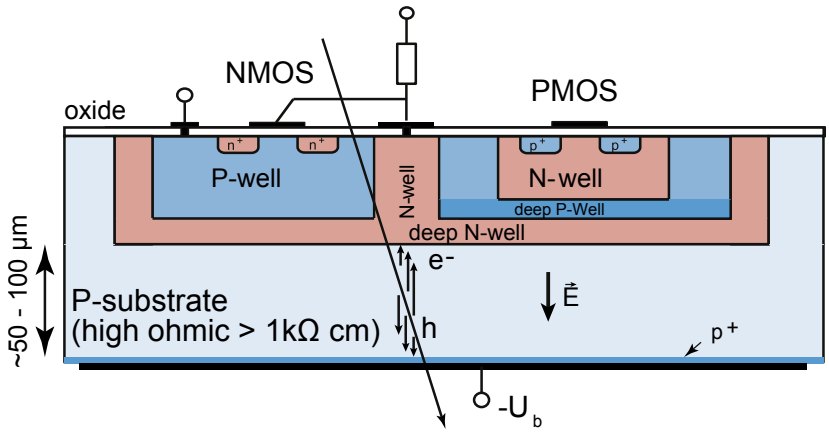


**Figure 3.16.** *In a Depleted Monolithic Active Pixel Sensor with large fill factor, the CMOS structures are completely embedded inside multiple wells to allow higher bias voltages. A "large fill factor" refers to the collection node – in this case the deep n-well – covering a large part of the pixel area. [15].*

The bias voltage is applied between the deep n-well and the backside, depleting the volume underneath the well structure. The CMOS circuitry is protected inside the deep n-well that serves as collection node. The separation of the depleted substrate from the MOS-containing wells allows the use of full CMOS logic. As for MAPS, a monolithic detector containing both analogue and digital processing in the active area can be designed but the stronger depletion enables charge transport by drift, enhancing radiation hardness [15, 22].

### 3.8.3.1. Fill factor and pixel capacitance

The DMAPS design shown above in Figure 3.16 has a "large fill factor" since the deep n-well that serves as collection node covers a significant part of the pixel area. The opposite principle is a "low fill factor" design as shown in Figure 3.17. Here, charges are not collected by a deep n-well enclosing all CMOS electronics but by a very small n-well outside of the electronics area.

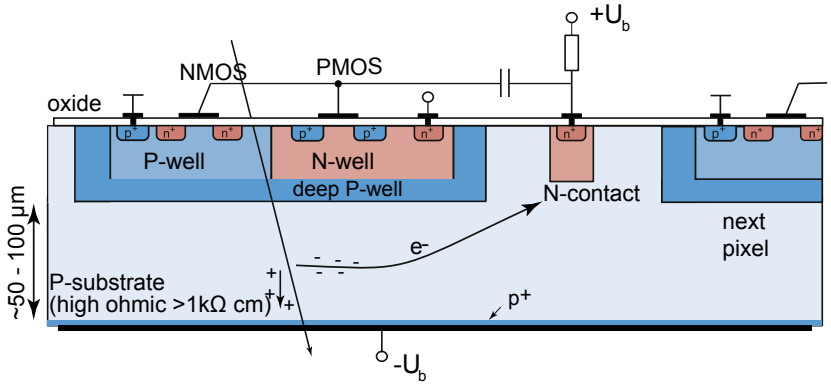


**Figure 3.17.** *In a Depleted Monolithic Active Pixel Sensor with small fill factor, a very small collection node is implemented to reduce the pixel capacitance [15].*

Both designs – large and small fill factor – aim at optimising different properties of the sensor.

- A large fill factor design enables good charge collection properties due to shorter distances of charge transport. Since the depletion field is especially strong around the collection node, the probability of trapping is reduced and radiation hardness is increased.
- A small fill factor design aims at reducing the pixel capacitance. While a large fill factor design can lead to a total pixel capacitance of ≈100 fF, a small fill factor design can reach values of ≈5–20 fF.

The total amplifier input capacitance of the pixel is determined by several capacitance contributions inside the pixel. The main contributions for both large fill factor and small fill factor designs are shown in Figure 3.18. A horizontal component is the capacitance between the collection node and neighbouring structures, in the case of a large fill factor the pixel-to-pixel capacitance $C_{pp}$ between deep n-wells, in the case of a small fill factor the capacitance $C_{np}$ between n-well and deep p-well. One contribution in both designs is the pixel-to-backside capacitance $C_b$ between collection node and substrate. Due to the smaller size of the collection electrode, the small fill factor design reaches significantly lower values of $C_b$.
In the large fill factor design, additional significant contributions originate from interwell capacitances both to the well sides and vertically between wells, marked by $C_{SW}$ and $C_{WW}$, respectively [22]. Since the collection node in the small fill factor design does not contain multiple wells, this contribution is not present.

### 3.8.3.2. Performance implication of the pixel capacitance

Keeping the pixel capacitance as low as possible is desirable to reduce the analogue power consumption of the pixel which is often determined by requirements on S/N. Perceiving the pixel cell as a capacitor, the signal can be expressed as a voltage of $V_{signal} = \frac{Q}{C}$ with $Q$ being the collected charge and $C$ being the "equivalent pixel input capacitance" [36].

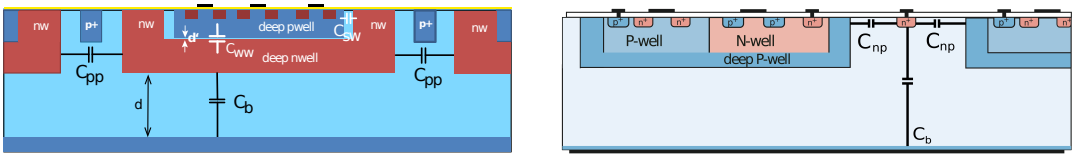


**(a)** *Large fill factor [22]* **(b)** *Small fill factor (based on [15])*

**Figure 3.18.** *In both the large fill factor design (a) and the small fill factor design (b) the total amplifier input capacitance is composed by different contributions. In the small fill factor design, interwell capacitances do not contribute.*

Next, the noise is expressed as equivalent voltage $v_{eq}$ using a simplified model. The noise of the MOS transistor is represented by a voltage source, parallel to the transistor or in series with the gate contact. The noise is frequency dependent and the frequency spectrum is given by Eqs. (3.8a) and (3.8b) [37]:

$$dv_{eq}^2 = \left( \frac{K_F}{WLC_{ox}^2 f^\alpha} + \frac{2kTn}{g_m} \right) df \qquad \text{for weak inversion} \tag{3.8a}$$

$$dv_{eq}^2 = \left( \frac{K_F}{WLC_{ox}^2 f^\alpha} + \frac{4kT\gamma}{g_m} \right) df \qquad \text{for strong inversion} \tag{3.8b}$$

The choice of equation depends on the working point of the transistor, i.e. if the transistor is in the weak or strong inversion state. Weak inversion refers to a state where the voltage $V_{GS}$ between gate and source is lower than the threshold voltage of the transistor. Although below the threshold, a leakage current is present and depends exponentially on $V_{GS}$. Strong inversion refers to a state where $V_{GS}$ is higher than the threshold voltage but the transistor has not saturated yet. In this mode, the current through the transistor depends linearly on $V_{GS}$.
In both equations the first term is often referred to as "$1/f$ noise", although the exponent $\alpha$ does not always coincide with exactly one. Furthermore, $K_F$ is a constant, $W$ and $L$ are the geometric transistor width and length, $C_{ox}$ is the capacitance of the gate oxide per unit area and $f$ stands for the frequency.
The second term in both equations expresses the thermal noise, $k$ being the Boltzmann constant, $T$ the absolute temperature, $n$ the weak inversion slope and $\gamma$ a "factor often around 2/3" [36]. The transconductance $g_m = \frac{\Delta I_{out}}{\Delta V_{in}}$ describes the relation between input voltage and output current. Its value is higher in the weak inversion state which is therefore preferred for low power pixel systems [36].

Particles with high energy deposit charges on such small time scale that slow phenomena like leakage current can be filtered out. This leads to thermal noise being the dominant contribution in the signal-to-noise ratio. In both cases – weak and strong inversion – S/N depends on the transconductance and the ratio $\frac{Q}{C}$:

$$\frac{S}{N} \sim \frac{Q}{C}\sqrt{g_m} \tag{3.9}$$

As mentioned before, the transconductance determines the current $I$ of the transistor and therefore of the readout circuitry. Using the relations for weak inversion ( $g_m \sim I$) and strong inversion ( $g_m \sim \sqrt{I}$) and assuming $I$ to dominate the power consumption $P$ of the front end, the following expressions are obtained:

$$\frac{S}{N} \sim \frac{Q}{C}\sqrt{g_m} \sim \frac{Q}{C}\sqrt[m]{I} \sim \frac{Q}{C}\sqrt[m]{P} \qquad \text{with } 2 \leq m \leq 4 \tag{3.10a}$$

$$\Rightarrow P \sim \left\{\frac{S/N}{Q/C}\right\}^m \qquad \text{with } 2 \leq m \leq 4 \tag{3.10b}$$

Equation (3.10b) shows that a reduction of the ratio $\frac{Q}{C}$ leads to a strong reduction of the power consumption for certain S/N in the analogue performance [36].
In HEP experiments, the power consumption of the detector is an important quantity. A large power consumption requires a powerful cooling system which can only be realised with a significant amount of material in the detector services, leading to a higher probability of particle scattering.

#### 3.8.3.3. DMAPS optimisation

Compared to hybrid concepts, monolithic sensors are advantageous in terms of cost and material. Especially DMAPS are promising candidates for monolithic sensors in high-radiation environments and a strong R&D effort is performed to probe the capabilities and push the limits in terms of fast charge collection and high charge-collection efficiency after irradiation.
Concerning the design optimisation, the key point to endure NIEL damage is to ensure sufficient depletion without damaging the readout electronics. This principle holds true for all presented detector types but gets most delicate for monolithic sensors due to the proximity of CMOS circuitry to the collection volume.
Comparing large and small fill factor designs, an optimal point is desired that ensures sufficient depletion after irradiation at the smallest amplifier input capacitance possible to optimise the sensor performance and reduce power consumption. This task becomes more and more challenging for hostile high-radiation environments.

# 4. TowerJazz Investigator

As described in the previous chapter, DMAPS are an interesting new technology for the ATLAS ITk. Regarding the challenging radiation environment, DMAPS technology is not yet expected to cope with the requirements of the future inner layers but might be considered for the outer layers. Here, the usage of a commercial CMOS imaging process can significantly reduce production costs.
In the context of this thesis, sensor designs produced in a 180 µm technology of the foundry TowerJazz[1] were tested concerning their potential for the ATLAS ITk.

In this chapter, the ALICE ITS Upgrade and the TowerJazz technology are presented as well as an analogue test chip – the TowerJazz Investigator – and its implemented features. At the end of this chapter, an innovative process modification is presented which had been developed together with the foundry to fully deplete the charge-collecting volume and ensure efficient functionality after irradiation.

## 4.1. ALICE ITS Upgrade

Similar to the ATLAS upgrade program, the ALICE detector will be upgraded to ensure and improve its performance. A new ALICE ITS with high resolution and lower material budget compared to the previous one will be installed around a new beampipe with a smaller diameter. The R&D program of the ALICE ITS is finished and its production is currently ongoing. The installation of the ITS is planned for the second long shutdown of the LHC in the years 2018-2019, in time to cope with a luminosity increase in Pb–Pb collisions as planned by the LHC.
The ALICE ITS will consist of seven barrel layers – three layers in an Inner Barrel and four layers in an Outer Barrel – with the center of the innermost layer at a radial position of 23.40 mm and the center of the outermost layer at a radial position of 393.35 mm [38].

[1] Tower Semiconductor Ltd, Israel

## 4.2. TowerJazz 180 nm technology

CMOS pixel sensors produced in the TowerJazz 180 nm technology offer among other features a high-resistivity epitaxial layer and the option of six metal layers. Process features of the sensors measured in the context of this thesis are given in Table 4.1:

**Table 4.1.** *Main features of the TowerJazz imaging process of the sensors presented in this thesis [39].*

| Feature | Property |
|---|---|
| MOS channel length | 180 nm |
| Metals | 6 layers, Aluminum |
| Supply rail | 1.8 V (up to −6 V on substrate) |
| MOS transistor types | full CMOS |
| Wafer type | epi p-type (>1 kΩcm), 25 µm thickness on p-type substrate |
| Backside implant | none |

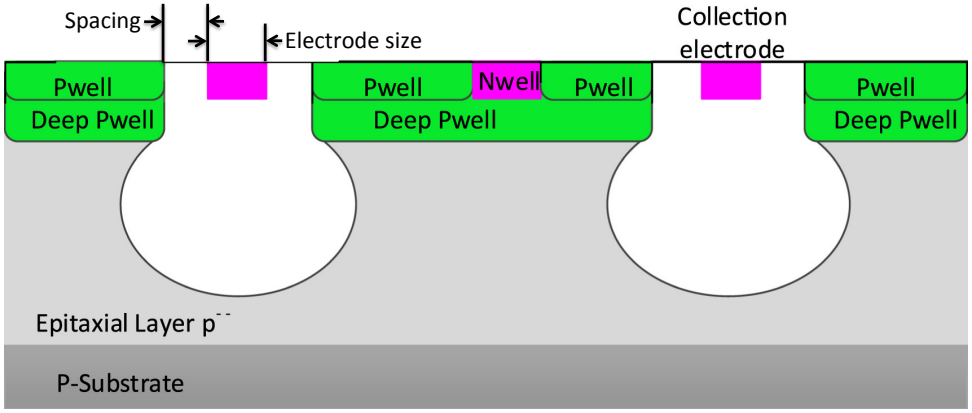


**Figure 4.1.** *Cross section of a TowerJazz sensor with low fill factor design. The shape of the depletion region is indicated in white [40].*

A key point for the ALICE collaboration was the availability of a deep p-well as shown in Figure 4.1, enabling a low fill factor design with full CMOS functionality of both PMOS and NMOS transistors in the pixel circuitry [41].

## 4.3. Investigator chip and pixel design

The **T**ower**J**azz **Inv**estigator (TJInv) is a test chip which was designed during the R&D process of the ALICE ITS. Its purpose is the investigation of geometric pixel-cell parameters and their effect on the analogue performance. The total area of the TJInv is $5.722 \times 5\,\mathrm{mm}^2$ and the chip consists of $2 \times 134$ different structures, also referred to as mini-matrices, as visible in Figure 4.2. Each mini-matrix contains 100 pixels in a $10 \times 10$ grid. The inner $8 \times 8$ sub-matrix of pixels is connected to wire-bond pads and their signals can be read out. The pixels in the remaining outer ring are powered and biased as the 64 central pixels but not read out. They serve as distance between the mini-matrices in order to reduce potential edge-effects [42].
All pixels of the TJInv have a square area, ranging from 20 µm to 50 µm pixel pitch. A scheme of the 134 mini-matrices in the sensor is given in Figure 4.3. The investigated structures are also referred to as for example, 'M129' for mini-matrix 129 as shown in the schematic. The entire set of matrices exists a second time on the chip, mirrored to the bottom half. In the bottom half, a circuit to induce charge was implemented into certain pixels. Due to connection problems, this feature was not working. It is re-implemented in a future version of the chip.

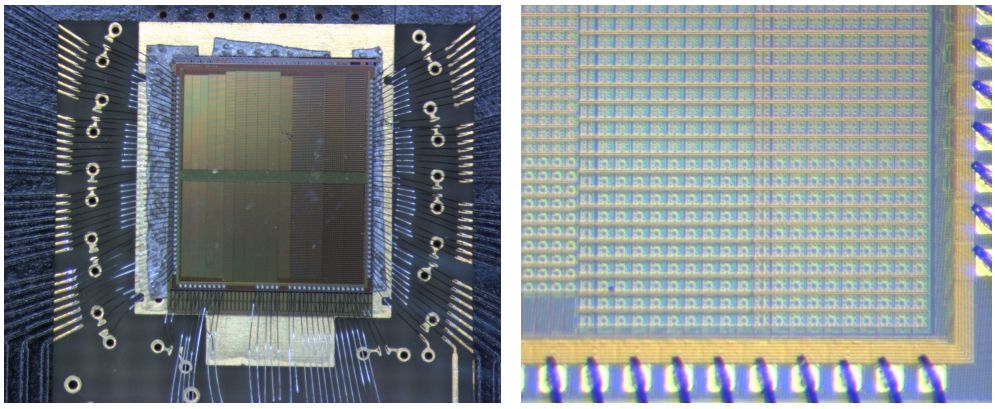

**(a)** *Investigator on carrier board* **(b)** *Pixels of mini-matrices*

**Figure 4.2.** *Glued and wire bonded Investigator (a) containing different mini-matrices (b).*

**Geometric properties of the pixel cell:** All pixels within one mini-matrix are identical. I addition to the pixel size, also the size of the collection electrode and its distance to the surrounding electronics – the spacing – can vary between mini-matrices. The opening is a function of electrode size and spacing. These parameters are shown in Figure 4.4a. Not all possible combinations are implemented, for example, large pixels are not combined with small openings.

Another geometric parameter is shown in Figure 4.4b. The deep p-well which shields the n-well is implemented in a minimal size, a medium size and a maximal size. Since the deep p-well is biased with the same potential as the substrate below, its size influences the electric field within a biased pixel.

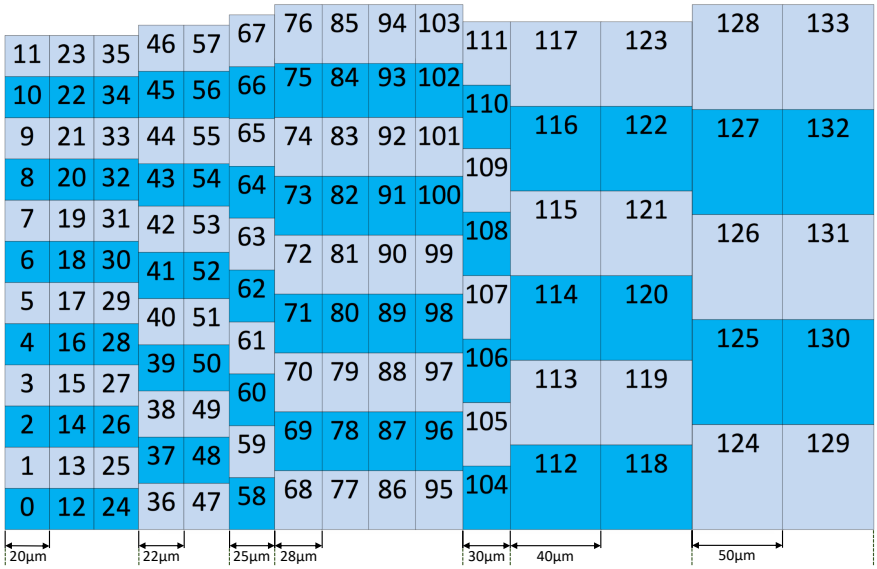


**Figure 4.3.** *The 134 mini-matrices of the TJInv. The pixel sizes range from 20×20 µm² to 50×50 µm² [42].*

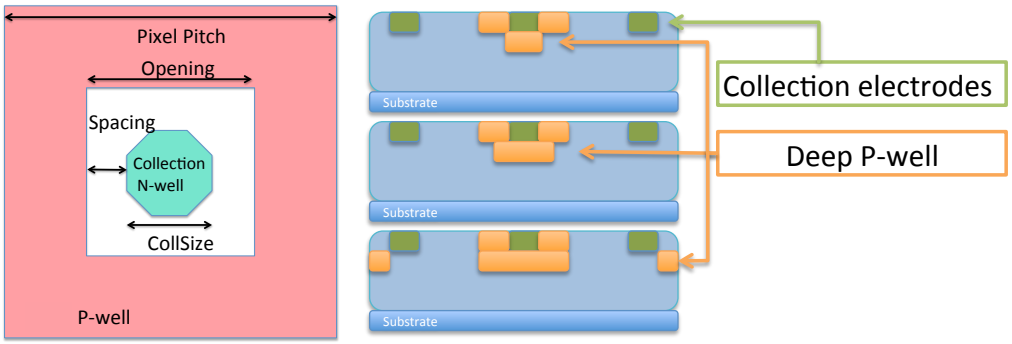


**(a)** *Geometric parameters (based on [39])*

**(b)** *Horizontal dimensions of the deep p-well [43, 44]*

**Figure 4.4.** *In the 134 mini-matrices of the Investigator, different combinations of geometric parameters are realised in the pixel cells. Pixel size, electrode size and spacing (a) are varied as well as the horizontal dimension of the deep p-well (b).*

**Pixel readout circuits:** The TJInv is designed for analogue readout of the pixels inside a selected mini-matrix. Deposited charges of a hit as well as leakage current induce a signal at the collection electrode. With time, accumulated charges cause a saturation of the pixel cell and new charges are not detected. To avoid saturation, a reset mechanism is implemented in each pixel cell. Some structures in the TJInv contain a double-diode reset. Here, the collection electrode is connected via two diodes to a positive reset voltage, leading to a constant discharging of the cell. Pixels containing this reset implementation were not measured in the context of this thesis since it leads to a slow reset during which the state of the cell is not well defined.

Other pixel structures contain an active reset based on a standard 3T cell. Here, the collection electrode is connected to the positive reset voltage over a transistor which is opened by an external control signal to remove the accumulated charges and reset the cell.

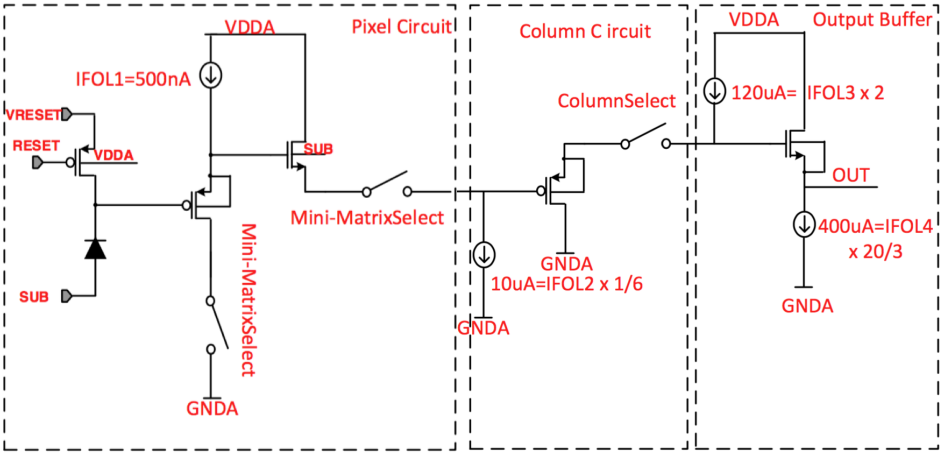


**Figure 4.5.** *Internal circuit and amplifier stages of a pixel: The left-hand block shows the 'Pixel Circuit' containing the p-n junction indicated as diode. The pixels of the selected matrix are then connected to the 'Column Circuit' and the 'Output Buffer'. In terms of the internal source follower circuit, the cathode of the diode – the collection electrode – serves as input node, the buffer output as output node [42].*

A schematic of the cell including the readout circuit is given in Figure 4.5. The collection electrode – the cathode of the p-n junction – serves as input node of the internal source follower. The constant currents in the source follower stages – IFOL1 to IFOL4 – are provided externally and determine the working point of the circuit. The current of the collected charges in the pixel cell is integrated as analogue information. The signals of the pixels of the selected mini-matrix are routed to a connected readout setup. In case of leakage current, the signal rises constantly until hitting the saturation of the source follower. In case of a particle hit, the current of the deposited charges induces a fast step function. In regular intervals, the reset transistor on the left-hand side of the schematic is opened and the pixel cell is reset [42]. The expected signal is discussed further in the next chapter in the context of operating the sensor and analysing the obtained signals.

## 4.4. Modified process for enhanced depletion

The described sensor design is a low fill factor design, aiming at a small capacitance. As mentioned previously, the downside of this approach is a limit in terms of depletion. Charges within a depleted volume are collected by drift whereas charges outside of the depletion area are collected by diffusion.

Based on these considerations, a process modification has been developed together with the foundry. A comparison between both processes – referred to as "Standard Process" and "Modified Process" – is shown in Figure 4.6. For both the Standard Process on the left-hand side and the Modified Process on the right-hand side, the depletion zone grows in the directions indicated by the yellow arrows. The reserve biasing voltage is applied to the substrate underneath the epitaxial layer as well as to the deep p-wells shielding the n-well electronics. In case of the Standard Process, achieving full lateral depletion including the area under the deep p-wells is difficult both before and after irradiation. For pixel geometries with a small opening and therefore a large coverage with electronics this problem is especially severe [45].

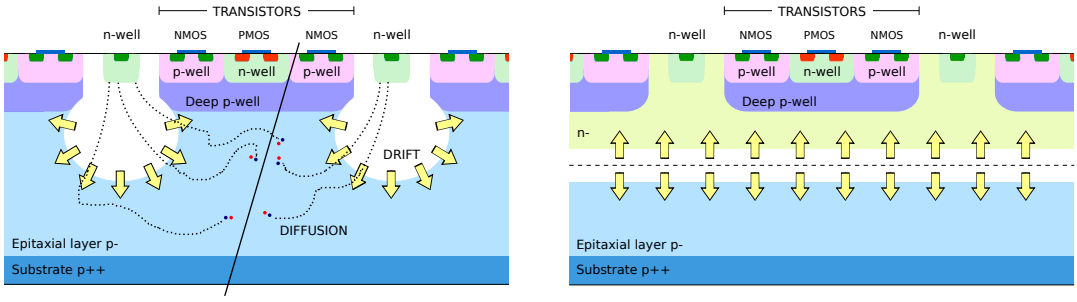


**(a)** *Standard process* **(b)** *Modified process*

**Figure 4.6.** *Comparison of the TowerJazz standard (a) and modified (b) process: While the depletion zone in the Standard Process is formed in a bulb-like shape, an additional low-dose n-type implant leads to a horizontal junction from which the depletion zone grows [46, 47].*

For the Modified Process, an additional low-dose n-type implant as shown in Figure 4.6b creates a planar junction over the entire pixel width. The depletion starts at the planar junction and covers the entire pixel area horizontally. With increased reverse bias voltage, the depletion then extends to the collection electrodes. Additional small junctions not marked in the figure are created between n-type implant and p-wells and deep p-wells.

The additional implant introduces additional capacitance components, increasing the total pixel cell capacitance. The design of the Modified Process is a compromise between low and high fill factor. The doping concentration of the additional n-type layer is a crucial parameter of the sensor's performance. On one hand, it should be sufficiently low to already enable full depletion when biased in the order of a few volts. This way, the capacitance of the pixel cell is still in the order of a few fF, keeping the advantages of a low-capacitance design. On the other hand, it should be high enough to prevent a punch-through between the substrate and the deep p-well. Simulations showed that the planar junction already depletes the entire pixel area at $HV = 0\,\mathrm{V}$ [45].

The process modification adds an additional implant but does not alter the remaining design and the TJInv could therefore be produced in both processes. and directly compared to test the enhanced depletion before and after irradiation and its impact on signal quality and sensor performance.

# 5. ATLAS TowerJazz Investigator test setup and data analysis procedure

The TJInv has been designed as an analogue test chip to investigate the impact of geometric parameters on the analogue features of the pixel cell. Having the timing requirements of the ATLAS ITk in mind, a new test setup with a high timing resolution has been designed. The focus was on analogue single-pixel measurements of different exposures – source scans and testbeams – and their interpretations.
By this, it was meant to complement a test setup previously built and used by the ALICE collaboration, reading out 64 pixels of the selected matrix simultaneously [48]. With a sampling rate of 15 ns between recorded data points, this setup did not provide the timing resolution which was aimed for in the context of this thesis. In this chapter, the new ATLAS TowerJazz Investigator test setup, its components and studies of its performance are presented.

## 5.1. ATLAS TowerJazz Investigator test setup

For the ATLAS TowerJazz Investigator test setup, the DRS4 oscilloscope was used which was designed and produced by the **P**aul **S**cherrer **I**nstitute (PSI) [49].

Its evaluation board is very compact and can be used to construct small setups for laboratory measurements and testbeam campaigns both at CERN and at external facilities.
The DRS4 offers a maximum sampling rate of 5 GS/s and records 1024 time-voltage data points per waveform for a maximum of four channels. The selected sampling rate in the setup of 1.982 GS/s leads to around 0.5 ns between recorded data points. This way the setup offers a thirty times higher timing resolution than the multichannel-setup by the ALICE group but also records a total interval of 517 ns, which is big enough to test for slow charge collection by diffusion.

**Supply and control:** All the **P**rinted **C**ircuit **B**oards (PCBs) of the ATLAS TowerJazz Investigator test setup are connected in series as shown in Figure 5.1. From left to right, there are the **M**ulti-**IO** board (MIO), the **G**eneral **P**urpose **A**nalog **C**ard (GPAC), the TowerJazz Adapter Card and the Investigator Carrier board.

The MIO is equipped with a **F**ield **P**rogrammable **G**ate **A**rray (FPGA). The FPGA firmware is written in the Hardware Description Language Verilog. The setup is operated with the pyBAR framework[2].

[2] `https://github.com/SiLab-Bonn/pyBAR`

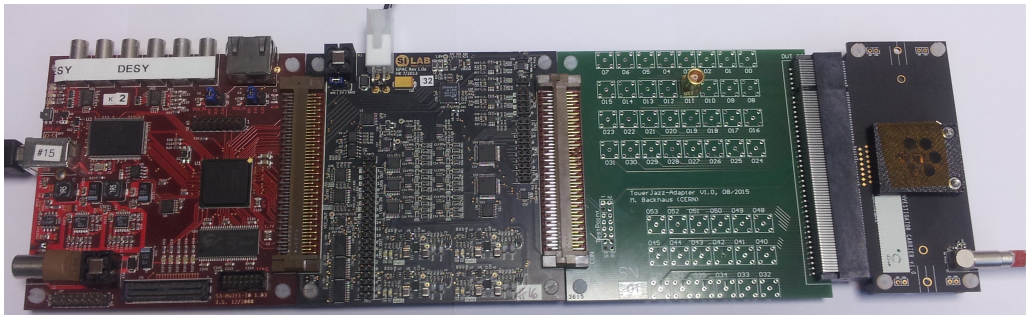


**Figure 5.1.** *The connected PCBs used in the ATLAS TowerJazz Investigator test setup from left to right: Multi-IO board, General Purpose Analog Card, TowerJazz Adapter Card (shown here V1.0) and Investigator carrier board.*

All signals and supplies – except for the bias voltage of the pixel cell – are generated by components on the GPAC. A list can be found in the appendix on page 131. The TowerJazz Adapter Card was specifically designed to connect the GPAC and Investigator carrier boards, which were designed and used by the ALICE group. This way, sensors could be tested in both setups to commission the new setup and compare results. The first three cards are connected via a 100 pin KEL-connector. The possibility of an extension via flat-ribbon cables is given. This way, carrier board and Adapter Card can be placed in small cooled containers as a climate chamber in the laboratory or a small cooling box in testbeam environments while the active components of MIO and GPAC are placed outside. The Investigator carrier board itself is connected to the Adapter Card via a 164 pin PCIe connector. The reverse bias voltage is connected directly to the carrier board of the TJInv. First measurements indicated the punch-through slightly beyond $HV = -7\,\mathrm{V}$. As a safety measure, the maximal value for operation was decided to be $HV = -6\,\mathrm{V}$.

**Readout:** During operation one matrix of the chip is selected via nine addressing bits. The outputs of the 64 pixels in this matrix are routed to 64 different pins of the PCIe connector on the carrier board. Out of those 64 signals, 25 are routed to LEMO connectors on the TowerJazz Adapter board V2.0 as seen in Figure 5.2. The 25 signals are arranged in a 5x5 grid and their position configuration coincides with the position configuration of the corresponding pixels.

The signal of a pixel is not connected directly to the channels of the DRS4 but through an external single-channel amplifier developed by cividec Instrumentation GmbH [50]. The cividec broadband amplifiers of the C1HV series are AC coupled low-noise current amplifiers and provide a gain of 20 dB and a bandwidth of 1 MHz - 2 GHz[3].
The amplifiers used in our setup were specifically altered by cividec for this setup. As mentioned, a particle hit leads to a step function in the analogue output signal of the pixel. A fast amplifier without modification shapes the signal in such a way that the signal has an exponential decay with small timing constant back to the baseline.

[3]Handbook C1HV available via `https://cividec.at/index.php?module=public.product&idProduct=32`

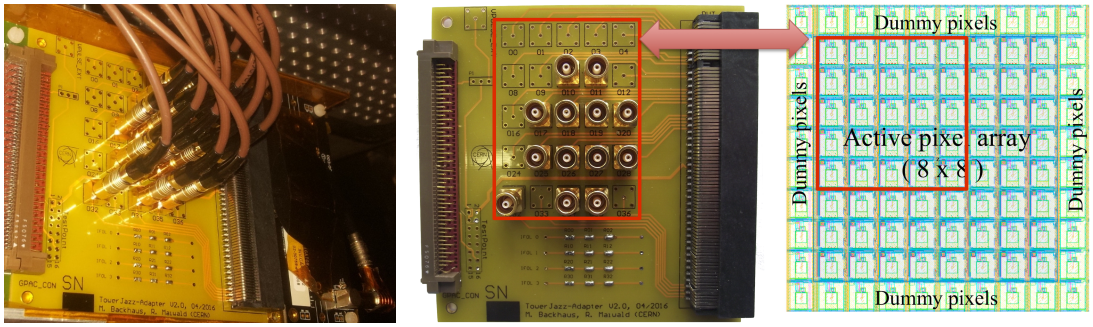


**(a)** *Multi-channel setup* **(b)** *Position configuration*

**Figure 5.2.** *TowerJazz Adapter V2.0 as used in a multi-channel setup (a). The signals of individual pixels are available via LEMO connectors on the board. The relative positions of the connectors correspond to the relative positions of the pixels (b).*

This becomes a disadvantage during the analysis of the waveform. The time constant of the internal circuit was increased to around 200 µs. This way, the effect on the signal shaping was reduced. Recording 1024 datapoint with a sampling rate of 1.982 GS/s covers an interval of around 517 ns. The exponential behaviour of the new time constant is only in the order of 0.3 % and thus negligible.
The output of each amplifier is connected to one input channel of the DRS4. Both devices are terminated by 50 Ω and AC coupled.

One amplifier is needed per measured channel. For most of the measurements presented in this thesis, only one channel (laboratory measurements) or four channels (testbeam measurements) could be read out. At the end of the project, five amplifiers were available for a short period of time to perform a small cluster measurement.

## 5.2. Data analysis procedure

Only pixels with active transistor reset were investigated. The behaviour of such a pixel is shown in Figure 5.3a, recorded by another oscilloscope to record a bigger interval. Every 25 µs the reset transistor in the pixel is opened for 200 ns. The pixel response is visible in the waveform plotted in red as very deep spikes. In order to only trigger on hits which appear as steps proportional to the collected charge as seen between the reset intervals, the spikes have to be vetoed. The black curve shows a reset-veto signal of 2.8 µs generated in the FPGA of the MIO. It contains the duration of the reset itself as well as additional time for the pixel to recover back to baseline-level.
For recording of the waveform the DRS4 software provided by PSI has been used. For every trigger, the complete waveforms of all connected pixel signals and the reset-veto are recorded.

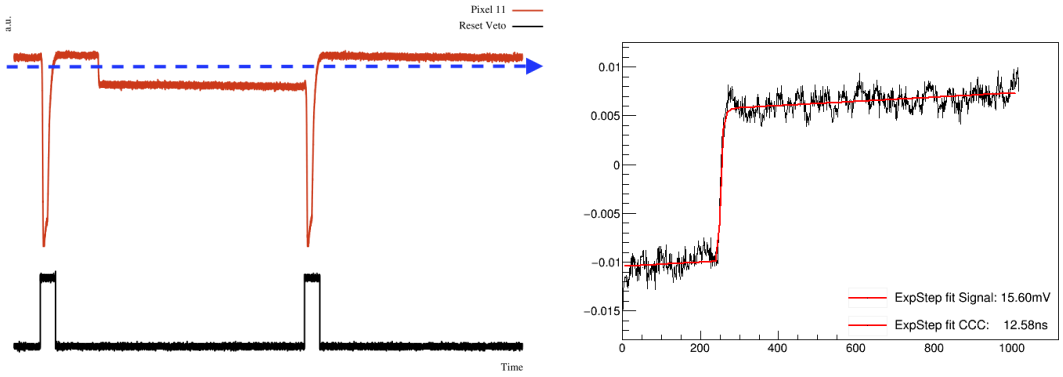


**(a)** *Pixel response (uninverted, red) and reset veto (black)*

**(b)** *Waveform (inverted) with fit*

**Figure 5.3.** *(a) Triggering is done directly on the pixel output (red) below the leakage level as indicated by the blue arrow. A reset veto (black) defines a time window around the reset to prevent triggering on the reset response. This data was recorded uninverted with a lab oscilloscope. (b) Offline, an exponential fit is performed as described in equations (5.1a) and (5.1b) [51].*

The recorded waveforms were – unless specifically stated otherwise – analysed with the software framework *tbConverter* [52]. The analysis contains the application of step-height requirements as rough cuts to separate hits from noise, and in case of a hit, a low-pass filter and of fit to the waveform. The low-pass filter is implemented as moving average. The framework and the fitting function have already been successfully used for performance studies of other technologies [53]. An example waveform recorded by a DRS4 with applied fit is shown in Figure 5.3b.

**Fit function** The fit function is given in the Equations (5.1a) and (5.1b) [53, 51].

$$t \leq t_0 \qquad f = a + m \cdot (t - t_0) \tag{5.1a}$$

$$t > t_0 \qquad f = a + m \cdot (t - t_0) - b \cdot (e^{-\frac{t-t_0}{c}} - 1) \tag{5.1b}$$

The algorithm implemented in *tbConverter* detects a step and estimates a starting value for the time $t_0$ of the particle hit. For $t \leq t_0$ a linear function (5.1a) is used to fit the leakage current. Then for $t > t_0$ the hit is described by adding an exponential function continuously in $t_0$ (5.1b). Hereby, $t_0$ is itself a fit parameter. Taking the six obtained fit parameters $\{a, m, t_0, b, c\}$, the step parameter $b$ is interpreted as signal amplitude. Fitting the waveform enables the extraction of the signal rise time $t_r$, defined as the time between 10 % and 90 % of the signal amplitude and calculated as $t_r = 2.2 \cdot c$.

In order to calculate the noise of the baseline, the data points recorded before the rising edge of the fit were used. The RMS of those data points – corrected for the slope induced by the leakage current – serves as estimation for the noise level.

## 5.3. Robustness of fit function against noise

The effects of both Gaussian noise and harmonic noise on the used fit function have been studied with simulated waveforms. An ideal noise-free waveform with $b = 100\,\text{mV}$ and $c = 10\,\text{ns}$ (resembling a signal rise time of 22 ns) was generated. Its data points were then altered with Gaussian and harmonic noise. Data sets of 10k events were created using the standard deviation of the Gaussian smearing as well as the amplitude and frequency of the harmonic noise as input parameters. The actual Gaussian noise per data point and the harmonic phase per waveform were drawn as random numbers. The data sets of simulated waveforms were analysed identically to recorded waveforms.

The working principle is shown in Figure 5.4a with the ideal waveform in black, the waveform with added noise in blue, the filtered waveform in green and the final fit in red. In this example, the Gaussian noise was set to $\sigma_g = 10\,\%$ of the signal $b = 100\,\text{mV}$, simulating a signal-to-noise ratio of S/N=10.

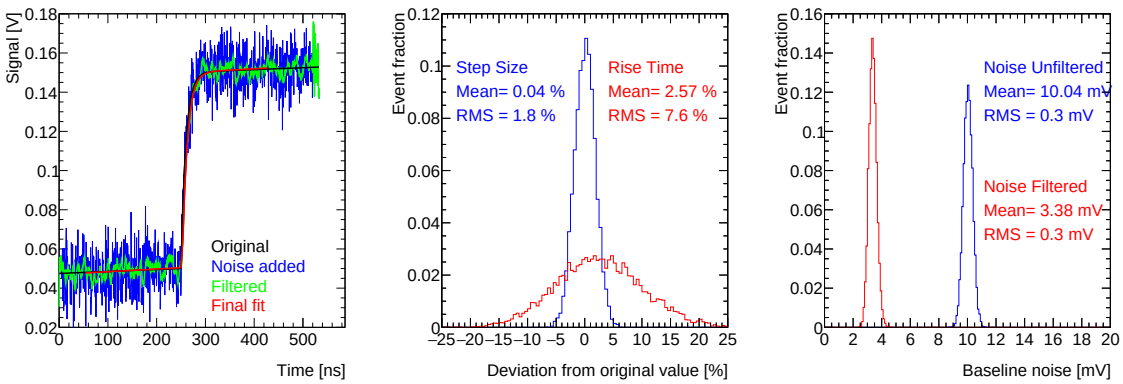


**(a)** *Waveform with added Gaussian noise, $\sigma_g = 10\%$*

**(b)** *Deviations from original values*

**(c)** *Noise levels before and after filtering*

**Figure 5.4.** *Investigating the effect of noise using simulated waveforms: Alteration of a waveform (a), deviations from the original parameters after fitting (b) and obtained baseline noise (c) before and after moving-average filter.*

Figure 5.4b shows the distributions of relative deviations between original and obtained parameter for signal and signal rise time. The baseline noise before and after the filter is given in Figure 5.4c.

The interval size of the moving average has a direct impact on the resulting S/N and the resolution of the obtained fit parameters. The waveforms altered with Gaussian noise are analysed using a moving average of different size. A high interval size resembles a low-pass filter with lower cutoff.
This leads to a stronger suppression of noise but also smoothens out the signal shape. At an interval size of 1024 – the total number of recorded data points – the waveform becomes a constant value.

Figure 5.5. shows means of simulated S/N distributions. As expected, waveforms with higher relative noise – also resembling smaller hits – benefit from a higher interval size. For the results presented in this thesis, a moving average size of 10 was chosen to obtain high S/N for both small and big hits.

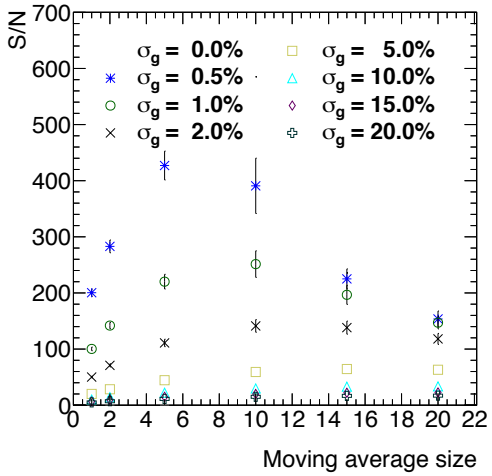


**Figure 5.5.** *Simulated S/N depending on filter average interval size: Waveforms with simulated Gaussian noise were analysed using a moving average of different size. The Gaussian noise is given as standard deviation relative to the ideal signal size. The error bars show the RMS values of the distributions.*

**Gaussian noise** The noise simulation procedure is performed for different values of Gaussian noise $\sigma_g$. Mean and RMS of the obtained distributions are indicators for noise induced bias and resolution limits. Their dependence on the noise is shown in Figure 5.6. The plots show the effect of Gaussian noise on signal size $b$ and signal rise time $t_r$ in terms of relative deviations with respect to the values of the ideal, that is, noise-free, waveform.
The means of the signal size deviations in Figure 5.6 stay below 0.1 % even for $\sigma_g = 20\,\%$, which corresponds to hits with S/N = 5. Gaussian noise does therefore not lead to a significant bias of the estimated signal size.
Figure 5.6b shows the corresponding RMS values of the deviations as a function of $\sigma_g$. They increase with increasing noise up to around 5 % for $\sigma_g = 20\,\%$ and contribute to the energy resolution of the setup. Hits with smaller signal size – a higher relative $\sigma_g$ – are more affected.
Looking at the results for the signal rise time, Figure 5.6c shows a quite constant bias of around +3 % even for the case of no simulated noise. This overestimation is a result of the used low-pass filter and fit procedure.

Figure 5.6d shows the corresponding RMS values of the deviations as a function of $\sigma_g$. Here, a strong impact of the Gaussian noise can be observed. The RMS of the timing distribution rises linearly and almost coincides with the RMS of the noise before applying the low-pass filter. Similar to the energy resolution, the timing resolution is affected by Gaussian noise. Hits with small signal size are more affected by this smearing than hits with high signal size.

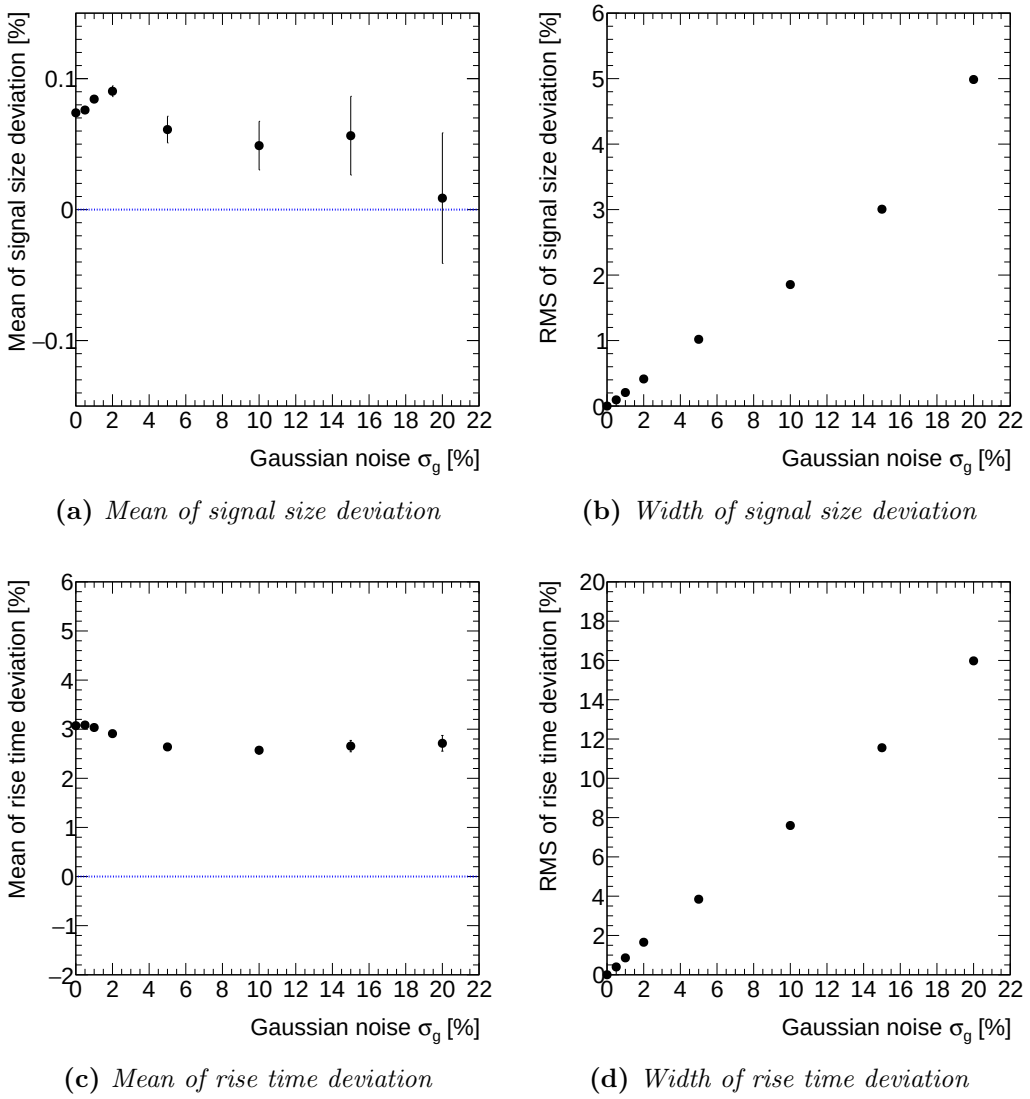


**(a)** *Mean of signal size deviation*

**(b)** *Width of signal size deviation*

**(c)** *Mean of rise time deviation*

**(d)** *Width of rise time deviation*

**Figure 5.6.** *Mean (a,c) and RMS (b,d) of the relative deviations between ideal parameters and fit results for signal size and signal rise time after adding Gaussian noise. The Gaussian noise is given as standard deviation relative to the ideal signal.*

**Harmonic noise** Another potential kind of noise is harmonic noise created by environmental sources. Examples are electromagnetic radiation of surrounding devices, mobile phones and power converters, or components of the setup. The best measures to reduce harmonic noise are the smoothing of supply voltages using capacitors and an effective shielding of setup and cables.
During the measurements, harmonic noise of significant size was only observed during the CERN SPS testbeam. The other measurements were performed in environments with more reduced noise, for example, the laboratory climate chamber, which served as additional shielding.

Examples of the effect of applied harmonic noise are presented in Figure 5.7. Depending on the phase of the noise, it can lead to underestimation of the signal as shown in Figure 5.7a or to overestimation as shown in Figure 5.7b. Data sets containing waveforms affected by both Gaussian noise and harmonic noise were also simulated.

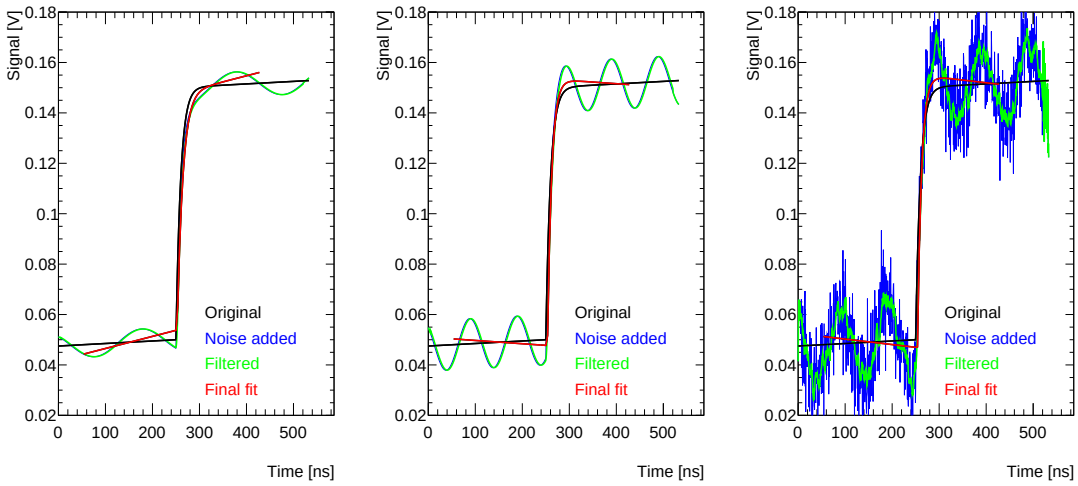


**(a)** $\sigma_g = 0\%$, $h = 5\%$, $f$=5 MHz

**(b)** $\sigma_g = 0\%$, $h = 10\%$, $f$=10 MHz

**(c)** $\sigma_g = 10\%$, $h = 15\%$, $f$=10 MHz

**Figure 5.7.** *Effects of harmonic noise on Waveforms: Depending on the phase of the harmonic noise, it can lead to an underestimation (a) or an overestimation (b) of the signal size. Waveforms containing both Gaussian and harmonic noise were also simulated (c).*

The deviations for different frequencies as well as combinations of harmonic and Gaussian noise can be found in the appendix starting on page 132. High-frequency noise has less effect on the fit parameter deviations since it is suppressed by the applied low-pass filter and it is also easier in the case of high-frequency noise.

In the case of a very low frequency, biases towards higher signals of almost +20 % and high signal rise times of almost +40 % are observed. The widths of the distributions are quite stable against high frequent noise but reach almost 60 % for signal size and 100 % for rise time. The effects of Gaussian noise observed before, without harmonic noise, are also present in combined simulations.

## 5.4. Noise of the external readout chain

In a linear readout chain every electronic component contributes to the total noise at the end of the chain. In order to test the performance of the setup and to identify its noise contributions, the chain is tested in steps by adding components starting from the very last one, the DRS4. This way, an observed increase in noise is caused by the most recently added part.

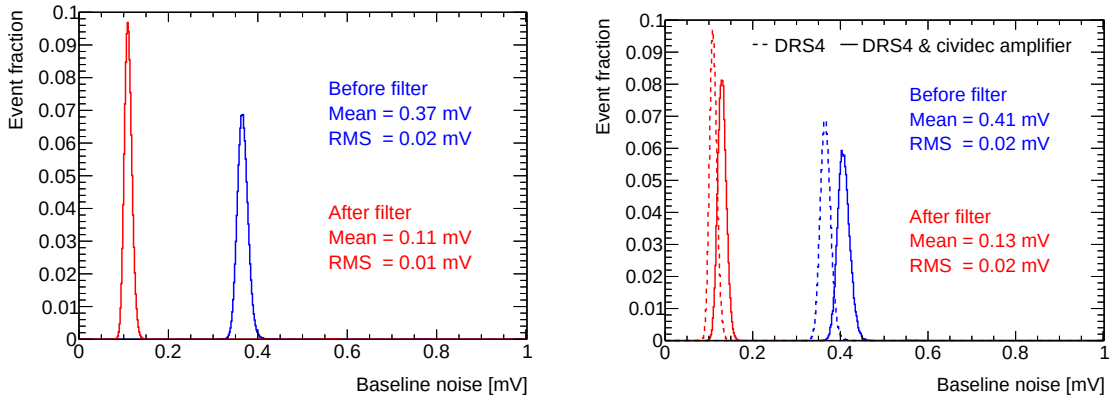


**(a)** *DRS4 baseline noise*

**(b)** *DRS4 and cividec amplifier baseline noise*

**Figure 5.8.** *Baseline input noise of the DRS4 without (a) and with connected cividec amplifier (b). The input was shortened with a 0 Ω termination and the noise – defined as RMS of the baseline – was estimated.*

**DRS4** The input noise of the DRS4 was measured while the channel input was shorted using a 0 Ω termination. 500k waveforms were recorded and the baseline RMSs calculated. The results are presented in Figure 5.8a. The values of the unfiltered DRS4 input noise shown in blue are distributed around 0.37mV with a width of 0.02mV. Regarding the simulations presented before, the impact of this noise level on a signal of size $x$ is comparable to $\sigma_g = \frac{0.37mV}{x}$. Regarding the S/N of the resulting spectra, the noise suppression between the distributions in blue and red is significant. This distribution peaks around 0.11 mV with a width of 0.01 mV. No harmonic component was observed during this measurement.

**External Amplifier – Noise level** In front of the DRS4 channels is the external cividec amplifier. Each component in the chain contributes its own noise component, therefore the amplifier was connected to the DRS4 while its input was shortened by a 0 Ω termination. Again, the baseline noise was recorded and analysed. Its distribution is shown in Figure 5.8b.

The distribution of unfiltered baseline noise peaks around 0.41 mV with a width of 0.02 mV. Assuming that the noise contributions of cividec amplifier and DRS4 add up quadratically, the noise contribution of the amplifier can be estimated to be:

$$\begin{aligned} \sigma^2_{\text{DRS4+amplifier}} &= \sigma^2_{\text{DRS4}} + \sigma^2_{\text{amplifier}} \\ \Rightarrow |\sigma_{\text{amplifier}}| &= \sqrt{\sigma^2_{\text{DRS4+amplifier}} - \sigma^2_{\text{DRS4}}} \\ &= \sqrt{(0.41\text{ mV})^2 - (0.37\text{ mV})^2} \\ &= 0.18\text{ mV} \end{aligned} \tag{5.2}$$

The noise contribution of the cividec amplifier is visible but small compared to the noise contribution of the DRS4. After applying the low-pass filter – shown in Figure 5.8b in red – the total noise level increases from 0.11 mV to 0.13 mV.

**External Amplifier – Amplification** Taking into account that the DRS4 is read out with a 14bit ADC over an input range of 1 V [42], the voltage resolution is 0.061 mV. This resolution impacts energy and timing resolution of the obtained spectra. In order to reduce its impact, the external cividec amplifier is used. Its effect is shown in Figure 5.9a, tested exemplary on a $^{55}$Fe spectrum measured with a sensor connected for an unirradiated 50 µm pixel of the standard process which will be discussed in more detail in the following chapter.

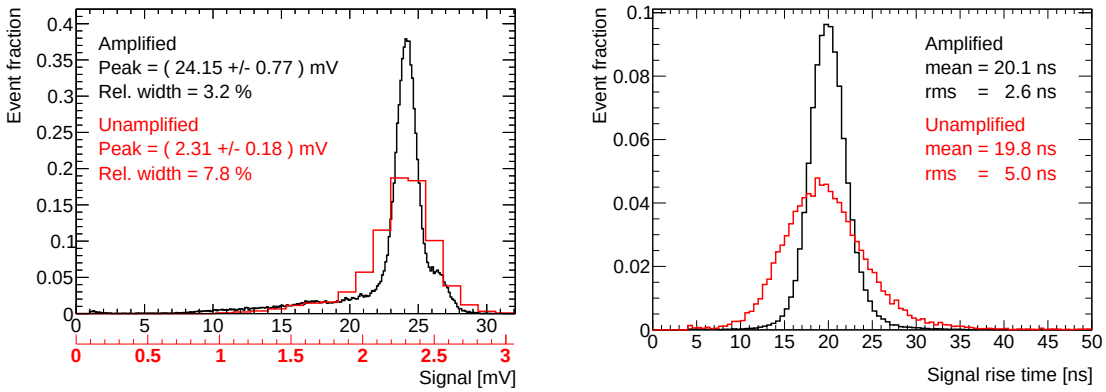


**(a)** *Effect on signal spectra* **(b)** *Effect on signal rise time distributions*

**Figure 5.9.** *Shape comparison of the obtained signal spectrum with (black) and without (red) external amplifier for an unirradiated 50 µm pixel (a). The spectra are scaled to have the peak positions overlap. The bin sizes match the DRS4 ADC resolution of 0.061 mV. The external amplifier also influences the distribution of the corresponding signal rise times (b).*

The signal spectra show an amplification for the peak position from 2.31 mV to 24.15 mV. The binning of both distributions is chosen to match the DRS4 voltage resolution of 0.061 mV. The energy resolution of the spectrum of unamplified signals shown in red is strongly limited by the DRS4 voltage resolution. For the spectrum of the amplified signals shown in black, the DRS4 resolution has a significantly lower impact on the obtained energy resolution. With amplifier, the relative width decreases from 7.8 % to 3.2 %. In the presented case, the improvement in resolution enables the visibility of the partly fused side peak of a second line in the amplified spectrum. Without the amplifier, both peaks have fused completely.

The corresponding distributions of the signal rise time are presented in Figure 5.9b. The timing resolution improves with a magnitude similar to the energy resolution by about 48 % from 5.0 ns to 2.6 ns.

**External amplifier – Signal-to-noise ratio** The improvements in energy and timing resolution are caused by the improvement in S/N. When no sensor is connected – as shown in Figure 5.8 – the baseline noise of the combination of DRS4 and external amplifier is around 10 % higher than the one of DRS4 alone. In order to estimate the effect of the external amplifier on S/N, the baseline noise distributions of the measurements with connected sensor shown in Figure 5.9 are analysed.

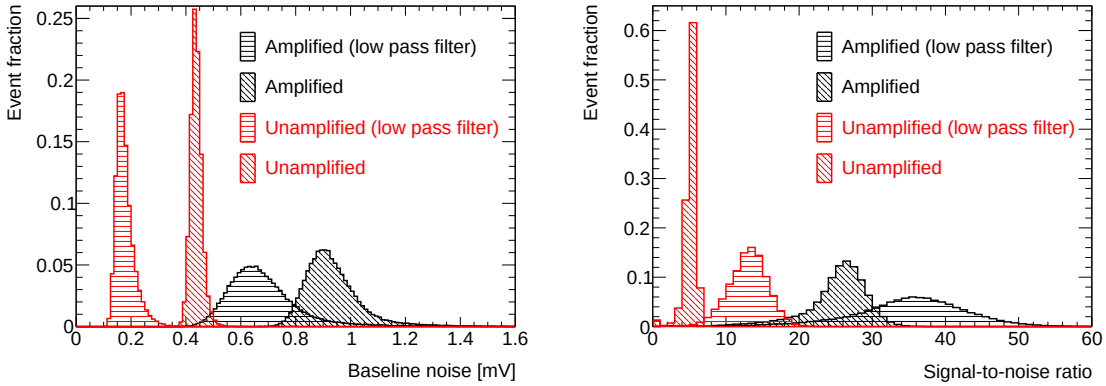


**(a)** *Noise distributions, standard process* **(b)** *Signal-to-noise ratios, standard process*

**Figure 5.10.** *Effect of the external amplifier on baseline noise (a) and signal-to-noise ratio (S/N) (b). The data sets are the ones of the $^{55}$Fe spectra shown in Figure 5.9.*

For both configurations – amplified in black and unamplified in red – the noise distributions shown in Figure 5.10a peak at higher values than when the sensor was replaced by a short as shown in Figure 5.8. Without external amplifier, the peak position is 0.44 mV instead of 0.37 mV. Assuming the noise contributions to add quadratically, the contribution of the sensor is estimated as $\sigma_{\text{sensor}} = 0.24\,\text{mV}$. However, with an external amplifier, the peak position is 0.94 mV. This leads to an estimation of $f * \sigma_{\text{sensor}} = 0.85\,\text{mV}$ with $f$ being the amplification factor. The value of $f = \frac{0.85\,\text{mV}}{0.24\,\text{mV}} = 3.5$ is significantly below the value of 10.5 obtained from the signal spectra peak positions. Despite it being a rough estimation, there might be a further noise contribution which is not amplified.

The distributions of the resulting S/N is presented in Figure 5.10b. Again, the entries of the distribution are calculated individually for each measured event. As expected from the improvement in energy and timing resolution, adding the external amplifier increases S/N. In case of applying the low-pass filter, the distribution peaks at around 35.0 instead of 12.8. The distribution gets very wide but 95 % of events have S/N>21.

## 5.5. Linearity of external readout chain

One important requirement of the setup is linearity. If the readout chain were to introduce nonlinearities, the obtained signal spectra were convolved. The linearity of the external readout chain was tested with an external pulse generator. Different signals with a total rise time of 30 ns (for the complete step) had been produced.

The lowest signal producible by the pulse generator is 10 mV. In order to validate the linearity of the low-signal range, the pulses were additionally divided down before the amplifier.

For each data point, 120k events were analysed using the standard analysis procedure. These points cover a signal range (in the DRS4 after amplification) from around 19 mV to 295 mV. The correlation between input pulse height and resulting signal size is presented in Figure 5.11. The data points show a strict linear behaviour over the investigated range. Non-linearities created by the external readout chain are not observed. The offset estimated by a linear fit is $(0.1 \pm 0.9)$ mV and at the level of the DRS4 baseline noise.

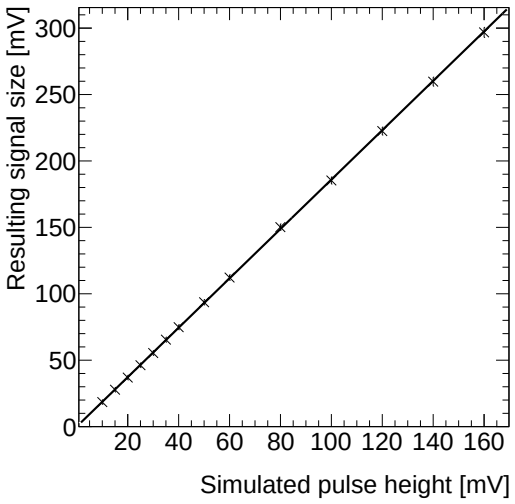


**Figure 5.11.** *The linearity test of the external readout chain was tested with generated step functions.*

## 5.6. Summary

In order to test the TJInv chip and its performance in terms of the requirements of the ATLAS ITk, the Time-precision setup has been designed and commissioned. Its main feature is obtaining a high timing resolution by using a high sampling rate. Simultaneous measurements of several neighbouring pixels are possible, limited by the number of available external amplifiers. Most results presented in this thesis were performed as single-pixel measurements. At the end of the project, more amplifiers were available for testbeam measurements. The effects of Gaussian and harmonic noise on the performance of the fit have been studied with a toy MC. In the presence of Gaussian noise, the estimated signal size stays unbiased, while the signal rise time gets overestimated by around 3 %, caused by the low-pass filter used in software. The presented results are not corrected for the this. The filter increases S/N significantly but is not able to reduce the effect of low-frequency harmonic noise. This noise has the biggest impact on the performance of the setup. Unless otherwise noted, no harmonic noise was observed during the measurements.

The noise contributions of all components in the external readout chain have been studied. The biggest contribution is the DRS4 input noise of 0.11 mV when using filtered. The external cividec amplifier only adds a minor contribution, increasing the noise to 0.13 mV. Compared to the estimated noise contribution of an unirradiated sensor of 0.24 mV, the devices in the external readout chain do not dominate to total noise level. In an environment with a high level of background noise, for example, testbeam measurements, noise induced into the connecting cables is expected.
The external amplifier increases S/N significantly due to the relatively high DRS4 input noise. In addition, the energy resolution of amplified signals is not dominated by the limited voltage resolution of the DRS4. This improves both energy resolution by around 59 % and resolution of signal rise time by around 48 %. The external readout chain shows an excellent linearity over the significant signal range. The offset of the correlation is at the level of the observed noise.

# 6. Signal characterisation of the Standard Process

The TJInv is a powerful tool to test and optimise the TowerJazz technology and the analogue features of its low-capacitance design. Its 134 substructures open up a multivariate space of design-parameter combinations. During the time of this thesis, different combinations were studied regarding the requirements of the ATLAS ITk. This chapter contains the results of performance studies on sensors produced in the Standard Process. First, measurements of the chosen working point conditions on exemplary matrices are presented. Second, the correlation between deposited energy and signal response is analysed for both the internal amplification circuit alone as well as for the pixel cell and readout. For the latter, monochromatic X-rays of different energies were used to characterise the signal spectra. Third, the shape of the signal spectrum is discussed and compared with simulations based on simple assumptions. Fourth, results of single-pixel studies with radioactive sources – $^{55}$Fe and $^{90}$Sr – before irradiation are shown. Fifth, these measurements were repeated for neutron irradiated sensors and the obtained results are compared to investigate performance degradation. The last section of this chapter presents a CERN SPS testbeam campaign testing hit-detection efficiency after irradiation.

## 6.1. Validation of the chosen working point

As a first study, source scans with $^{55}$Fe were used to test the impact of different settings for the reset voltage $V_{\mathrm{RESET}}$ and the biasing voltage $HV$. A clear Gaussian peak with a width given by the energy resolution is expected. The results of a scan to validate the chosen point for $V_{\mathrm{RESET}}$ is shown in Figure 6.1 for a backbias voltage of $HV = -3\,\mathrm{V}$ on the top and $HV = -6\,\mathrm{V}$ on the bottom. These results are obtained for the 30 µm pixel structure M106 of an unirradiated chip.

The parameters of interest are pixel gain (position of the $^{55}$Fe peak), energy resolution of the peak, rise time, and timing resolution. Charge sharing with neighbouring pixels results in a hit continuum below the $^{55}$Fe peak which will be discussed later in this chapter. For the study of the working point, only the peak position is used. The normalised signal distributions show higher positions of the $^{55}$Fe peak in the case of lower values of $V_{\mathrm{RESET}}$ for both $HV = -3\,\mathrm{V}$ and $HV = -6\,\mathrm{V}$. A value for $V_{\mathrm{RESET}}$ of 1.2 V is clearly not feasible. The measurements for 0.8 V and 1.0 V differ only slightly. For each peak, mean and standard deviation are given. $V_{\mathrm{RESET}}$ also effects the energy resolution. The timing distribution gets narrower for higher values of $V_{\mathrm{RESET}}$ for both $HV = -3\,\mathrm{V}$ and $HV = -6\,\mathrm{V}$ while the mean of the distribution increases.

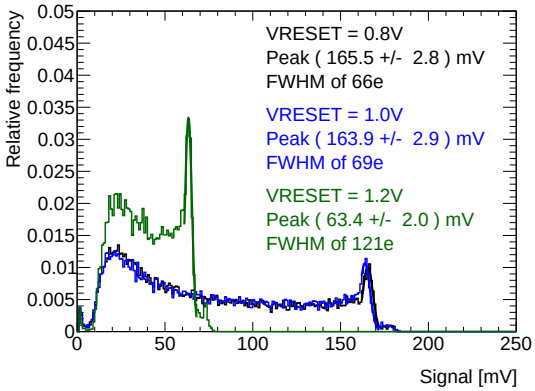


**(a)** *$^{55}$Fe spectra for different $V_{\mathrm{RESET}}$ values and $HV = -3V$*

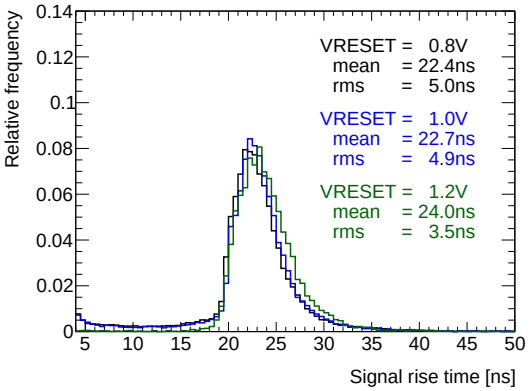


**(b)** *Timing distributions for different $V_{\mathrm{RESET}}$ values and $HV = -3V$*

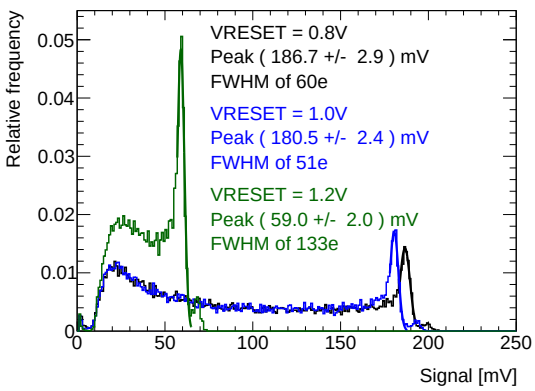


**(c)** *$^{55}$Fe spectra for different $V_{\mathrm{RESET}}$ values and $HV = -6V$*

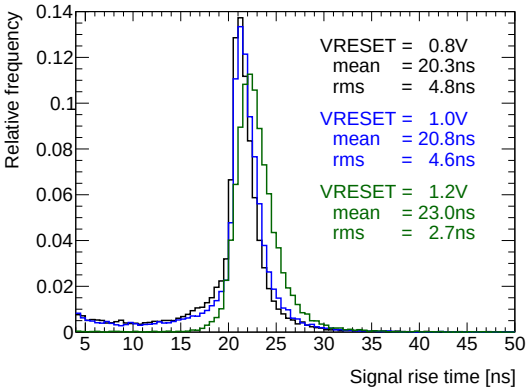


**(d)** *Timing distributions for different $V_{\mathrm{RESET}}$ values and $HV = -6V$*

**Figure 6.1.** *$^{55}$Fe spectra and timing distributions for different values of $V_{\mathrm{RESET}}$. The peak positions in the signal spectra change with $V_{\mathrm{RESET}}$ for both $HV = -3\,\mathrm{V}$ (a) and $HV = -6\,\mathrm{V}$ (c). The timing distributions (b,d) are less affected.*

The manual of the TJInv mentions of a value of $V_{\mathrm{RESET}} = 1\,\mathrm{V}$ [42]. This value proves to be a reasonable value regarding the parameters of interest. For all results presented in this thesis $V_{\mathrm{RESET}}$ was set to 1.0 V unless mentioned otherwise.

Another important value during the operation of semiconductor sensors is the biasing voltage $HV$. As described before, it is used to create an electric field and a depletion region inside the collection volume. For the TJInv chip, the maximum bias voltage used was $HV = -6\,\mathrm{V}$. The effect of different $HV$ settings on the $^{55}$Fe signal spectrum is shown in Figure 6.2a. As before, these results were obtained for an unirradiated chip of the Standard Process with a 25 µm epitaxial layer thickness. The spectra of $^{55}$Fe show that a larger bias leads to higher signal sizes for the $k_\alpha$ peak. This is expected since similar to a capacitor, the capacitance is inverse proportional to the applied voltage for a given charge. The energy resolution improves with stronger biasing.

The distributions of the signal rise time are shown in Figure 6.2b. The increase of the depletion volume also affects the timing distributions. The distributions get narrower towards $HV = -6\,\mathrm{V}$. A small side-peak around 20 ns is visible in the distributions of $HV = -1.5\,\mathrm{V}$ and fuses with the main peak for higher values but the peak position seems not to shift below this value.

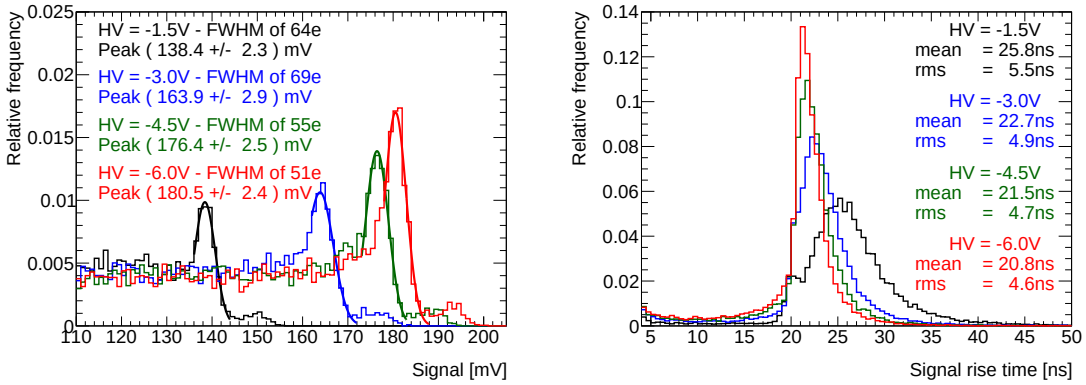


**(a)** *Peaks of $^{55}$Fe spectra for different HV (normalised over the entire spectrum)*

**(b)** *Corresponding timing distributions*

**Figure 6.2.** *The value of HV has a direct impact on the $^{55}$Fe spectra (a). A stronger biasing increases the gain as shown by the increase of the $^{55}$Fe peak position in mV. An effect is also visible in the timing distribution (b). A stronger biasing results in stronger electric field lines in the charge-collection volume and reduces the capacitance. The distributions appear narrower and peak at lower signal rise times.*

An increase of high voltage leads to an increase of the electric field which lowers the capacitance of the pixel. The low-capacitance design is sensitive to this reduction leading to an increase of the gain. The reduction in capacitance also results in a reduction of the signal rising time. Both effects seem to increase asymptotically but no saturation is reached up to $HV = -6\,\mathrm{V}$.

## 6.2. Correlation of deposited energy and signal size

During the commissioning of the Time-precision setup the linearity of the external amplifier and readout chain was shown. No corrections for the recorded signal spectra are needed. The aim of the investigations is the understanding of charge collection and signal creation in the pixel cell. For this, the next step is to test the association of recorded signal spectra with the energy spectra of the deposited charges. In case of a linear correlation between deposited energy and created signal, a simple calibration using known energy depositions with monochromatic photons can be used. The spectrum is then rescaled without affecting the shape.

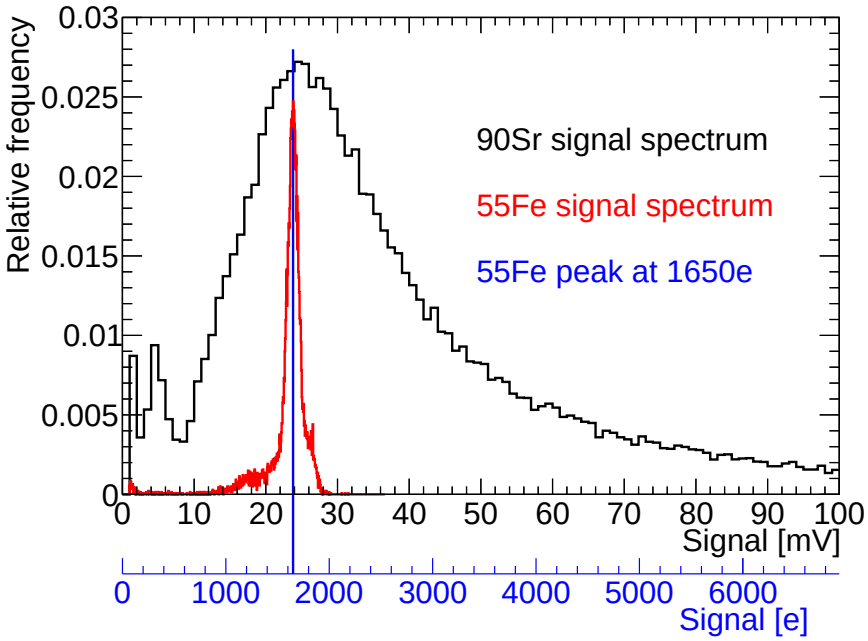


**Figure 6.3.** *Single-pixel spectra obtained using $^{55}$Fe in red and (b) $^{90}$Sr in black. Assuming a linear correlation between deposited energy and obtained signal, the energy spectra (blue scale) can be calculated using the $k_\alpha$ peak position of the $^{55}$Fe signal spectrum as indicated [46].*

This procedure is highlighted in Figure 6.3. An example signal spectrum of $^{55}$Fe, recorded with the 50 µm pixel structure M129 of an unirradiated Standard Process sample is shown in red. In the radioactive source, $^{55}$Fe decays via electron capture to $^{55}$Mn with a half-life of 2.73 years. The vacant position on the k-shell is then filled by an electron from a higher shell. In this process, X-rays with an energy of $k_{\alpha,\mathrm{Mn}}$= 5.90 keV and $k_{\beta,\mathrm{Mn}}$= 6.49 keV are emitted with a probability of 24.4 % and 2.86 % respectively [17]. A clear $k_\alpha$ peak is visible as marked by a blue vertical line. The peak position value corresponds to 5.9 keV of the monochromatic photons being completely deposited in the pixel. Using the energy of 3.6 eV needed to create an electron–hole pair [54], the peak position is associated with a deposited charge of 1650 e. Under the assumption of a linear correlation between energy and signal, the calculated correlation factor is then used to convert the scale of the signal spectrum – shown as x-axis in black – into the scale of the energy spectrum – shown as blue x-axis – to obtain the energy spectrum of the measurement.
Another measurement performed with the MIP-like $\beta$-source $^{90}$Sr on the same pixel of the same device under the same conditions is shown in Figure 6.3 as signal spectrum in black. Since these measurements have the same gain properties, the correlation factor determined with $^{55}$Fe is also valid to convert the $^{90}$Sr signal spectrum into an energy spectrum assuming linearity.
The energy spectrum contains the information about charge deposition and charge collection for a traversing MIP. Charges deposited inside of the depletion zone move by drift, charges deposited outside of the depletion zone move by diffusion. Charge collection by diffusion is characteristically slower.

Taking this into account and only analysing fast hits in the energy spectrum, the position of the MPV is a measure for the vertical size of the depletion zone. Here, we assume 63 $e^-h$ pairs/µm [55] for the thin sensors of 25 µm thickness. For full lateral depletion, we therefore expect an MPV value of $63 \frac{e}{\mu m} \cdot \sim 25\,\mu m = 1575\,e$. For the spectrum shown in Figure 6.3, the estimated MPV position is 1759 e and in good agreement with full vertical depletion. The small deviation to a higher collected charge might be caused by charge carriers of the transition region between the epitaxial volume and the substrate, which is expected to contribute 10 % additional charge [39].

The example showed the conversion between recorded signal spectrum and energy spectrum in case of a linear correlation. Two different methods are used to probe the linearity of the sensor: One method is the analysis of the transfer function of the internal source follower circuit [40]. The other method is the analysis of signal distributions for monochromatic photons of different energies.

### 6.2.1. Transfer function of the internal source follower

The correlation between the voltage level at the input node of the circuit (collection electrode) and its output node (output of the chip) is called the transfer function. The circuitry is shown in Figure 4.5 on page 35. The TJInv offers the possibility of probing the potential at the input node for pixels with active reset, that is, pixels whose circuit includes a reset transistor. By keeping the reset transistor constantly open, the voltage level set as reset voltage $V_{\mathrm{RESET}}$ is set at the input node. During the measurement, the bias voltage is set to ground ($HV = 0\,\mathrm{V}$ ). The potential of the input node is then altered and the DC level of the output node is measured.

An example for a transfer function of a Standard Process chip obtained with the multichannel setup of the ALICE group is shown in Figure 6.4a. The results for different structures on an unirradiated sensor are presented in Figure 6.4b. The measurements were scripted and automated in steps of 0.05 V. All functions show a linear range below the chosen working point and another linear range above before reaching a saturation, caused by the PMOS transistors of the source follower circuit. The working point of 1.0 V resembles the state of the cell after reset. While collecting negative charge – either by leakage current or a particle hit – the potential at the input node reduces. For operation, a working point at the upper end of a long linear range is anticipated. This way, a linear transfer behaviour is established before saturation.

The measured transfer function shows no explanation for the reduction of signal size in the case of $V_{\mathrm{RESET}} = 1.2\,\mathrm{V}$ as observed in the spectrum in Figure 6.1. Since it is not caused by the (DC) transfer function, other possible reasons are an increased leakage over the closed reset transistor during normal operation mode.

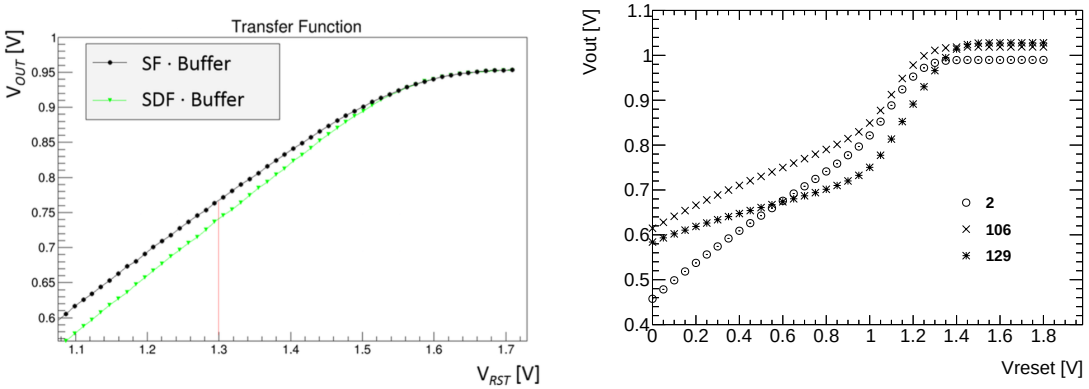


**(a)** *Transfer function of Standard Process chip [40]*

**(b)** *Transfer function for different structures*

**Figure 6.4.** *Transfer functions of Standard Process as measured in the multi-channel setup (a) and as measured in the Time-precision setup (b). All functions show an area of linear correlation before a saturation of the amplifier stages start.*

### 6.2.2. Linearity test using monochromatic fluorescence lines

The observed transfer functions show a linear correlation over a certain range. Beyond this range, the signal saturates. The external readout chain shows a strict linear behaviour as shown in the previous chapter. Therefore, any nonlinearities between deposited energy and recorded signal only depend on the working point position inside the transfer function.
Given a certain energy depositon, for example, by the fluorescence lines of $^{55}$Fe, the position of the working point on the transfer function depends on the internal gain of the pixel. This gain is among other things a function of the capacitance of the pixel and the applied bias voltage. In order to determine the correlation between deposited energy and resulting signal for given pixels, additional energy lines are measured in X-ray fluorescence setups. A picture of the X-ray fluorescence setup at the University of Glasgow and the working principle are shown in Figure 6.5.

An X-ray tube is directed towards a thin target and emits the “incident beam” indicated in yellow. When the X-ray photon hits the target, an electron of the k-shell might be excited to leave the atom, creating a vacant space. This space then can be filled by an electron coming from a higher shell, emitting the energy difference as a “secondary X-ray” photon indicated in green.
The setup is placed in a cooling box with supply of dry air. The box will be closed and a target is placed on top indicated in red. A replica of the Time-precision setup as described in the previous chapter was used to test TJInv sensors at Glasgow. The only difference was the usage of a laboratory oscilloscope instead of a DRS4. A second setup has been designed, constructed and commissioned at CERN by the local ATLAS CMOS group. The CERN setup was successfully used to measure unirradiated samples and is currently under development to add sufficient cooling for the analysis of irradiated samples.

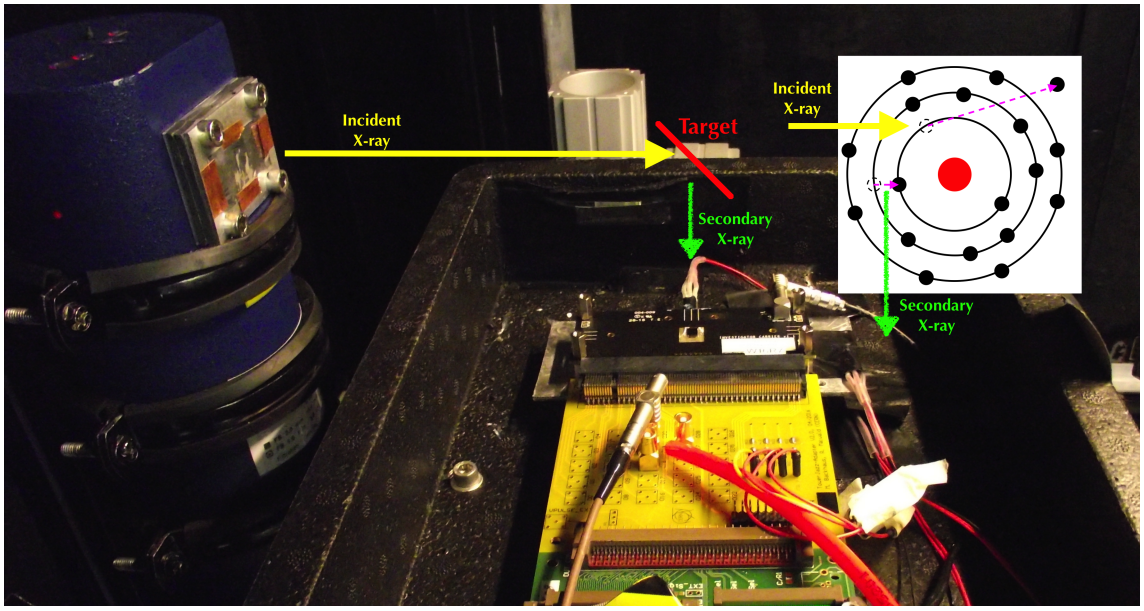


**Figure 6.5.** *Glasgow fluorescence setup and working principle.*

The fluorescence photons of each spectral line are monochromatic and can therefore be used for energy calibration. With different target materials, photons of different energies can be produced. The covered energy range is presented in Figure 6.6.
Different pixel structures of an unirradiated Standard Process sensor were tested in the Glasgow X-ray fluorescence setup. Measurements with five different targets – Fe, Cu, Se, Nb, Sn – were recorded.

The waveforms recorded by the laboratory oscilloscope were converted and then analysed using the standard framework and procedure to determine the signal size of the $k_\alpha$ peaks. In order to be compatible to measurements previously performed by the Glasgow group, the chip was only biased to $HV = -5\,\mathrm{V}$ in these measurements. The results are shown in Figure 6.7.

The data was fitted using an exponential function to consider saturation. Equation (6.1) gives the used formula, $s$ being the final level at saturation, $\tau$ being the constant of the exponential behaviour and $m$ being an offset

$$g(q) = s \cdot (1 - e^{-\frac{q}{\tau}}) + m \tag{6.1}$$

Fits with $m$ being a fit parameter are shown in Figure 6.7a, fits with $m = 0$ fixed are shown in Figure 6.7b.
Concerning the results, two types of structures are visible: On one hand, some pixels (M114, M126 and M129) produce relatively low signals for the $k_\alpha$ peaks. These in the context of the thesis called **L**ow **G**ain (LG) pixel structures show a fairly linear behaviour over the entire investigated range. For LG structures, the linear approach for converting signal spectra into energy spectra described above shows to be reasonable. The example in Figure 6.3 was a pixel of M129.

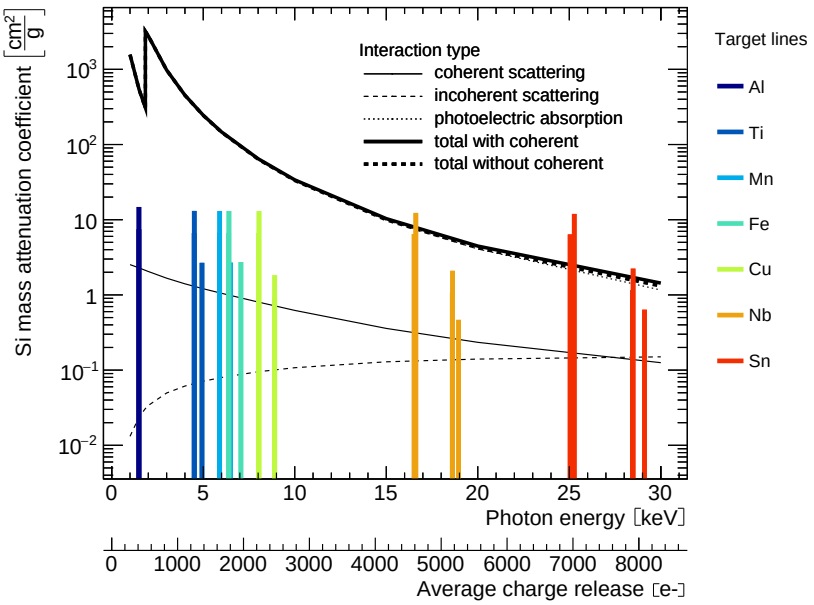


**Figure 6.6.** *Energies of different X-ray fluorescence targets. The dominant process in the shown energy range is photoelectric absorption. Using different target materials, a range from around 1.5 keV up to 25 keV was covered. One target material can emit several lines in the energy range [46].*

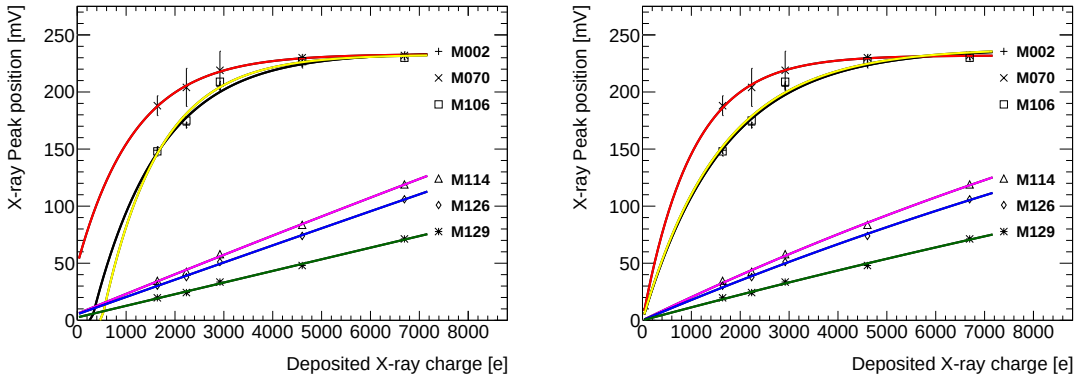


**(a)** *X-ray results - Fit with offset*

**(b)** *X-ray results - Fit without offset*

**Figure 6.7.** *X-ray fluorescence on unirradiated Standard Process. The signal size of the $k_\alpha$ peaks of different pixels for five used targets – Fe, Cu, Se, Nb, Sn – are shown. An exponential fit function with (a) and without (b) offset is added.*

On the other hand, some pixels (M002, M070 and M106) produce relatively high signals for the investigated $k_\alpha$ peaks. For these **H**igh **G**ain (HG) pixel structures, the peak positions reach a saturation approximately at 240 mV. The saturation behaviour resembles the shape of the already observed transfer function. When using the linear conversion from signal to energy spectra, the range beyond iron and copper will be compressed. The differences of LG and HG structures are probably caused by different pixel capacities but were not studied in more detail.

To correct for this behaviour, calibration measurements with multiple lines are needed for each different pixel and sample under controlled conditions like bias voltage and temperature.
As said before, the expected MPV position for MIPs is around 1575 e for sensors of 25 µm thickness. This energy is slightly above $k_{\alpha,Fe}$ and below $k_{\alpha,Cu}$. In case of charge loss or charge sharing, the MPV position will reduce further away from the saturation region. During the measurements in the lab, the $^{55}$Fe source is used to estimate the gain of the pixel structure, this position is therefore known. Regarding the results of the LG structures and the fit results with $m = 0$, using the linear conversion as first-order approximation around $k_{\alpha,Fe}$ is sufficient to qualitatively compare the MPV. In the context of this thesis, also the energy spectra for HG structures were obtained this way. For further validation of this approximation, the X-ray measurements must be repeated with targets providing $k_\alpha$ peaks at lower energies like aluminum or tin.

## 6.3. Performance of the Standard Process before irradiation

As mentioned before, the sensors of the upcoming ALICE ITS upgrade will be produced in the TowerJazz Standard process. During the R&D phase, sensors of this process, including the TJInv, were intensively tested to prove capabilities and to optimise parameters. The tests had been performed on unirradiated samples as well as irradiated samples up to $1.7\times10^{13}$ n/cm$^2$. The results were published [48, 33].

Some results were reproduced with the Time-precision setup in order to validate the setup but also to acquire data for the unirradiated Standard Process to later compare with irradiated samples and samples of the modified process.

The results obtained in the Glasgow fluorescence setup showed significant differences in gain between pixel structures present in the TJInv chip. Using the $^{55}$Fe target, more pixel structures were tested to search for correlations to the geometric parameters – pixel size (pitch), electrode size and spacing – of the respective pixel design. The results are presented in Figure 6.8. In each data set, the remaining parameters are kept constant.

First measurements indicated that pixels with larger pitch are more likely to be in the LG category and pixels with smaller pitch to be in the HG category. In order to test this further, pixels of different size had been used as shown in Figure 6.8b. Unfortunately, no pixels of 40 µm or 50 µm size with a spacing of 3 µm are available in the chip. No clear correlation between pixel size and gain is visible since the 30 µm structure M106 provides a high gain.
The comparison of pixels with 28 µm pixel size and 3 µm spacing but different electrode size is given in Figure 6.8c. Here, a smaller electrode size corresponds to a significantly higher gain, caused by a smaller capacitance between the electrode and the epitaxial layer.

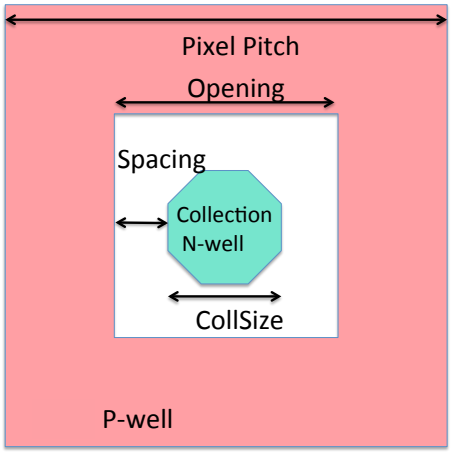


**(a)** *Geometric parameters of the pixel cell (based on [39])*

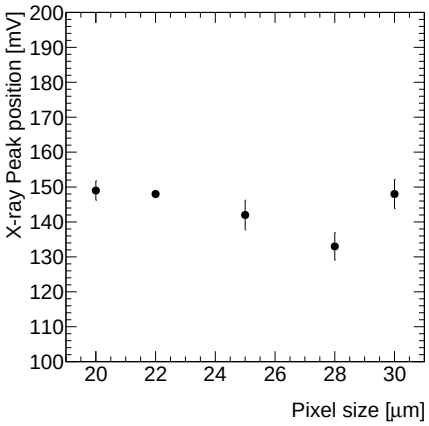


**(b)** *Effect of pixel size (pitch), electrode size 3µm, spacing 3µm*

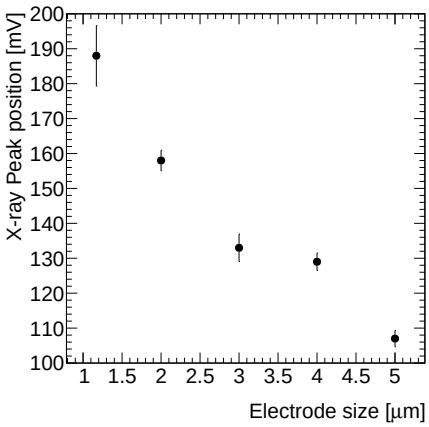


**(c)** *Effect of electrode size, pixel size 28µm, spacing 3µm*

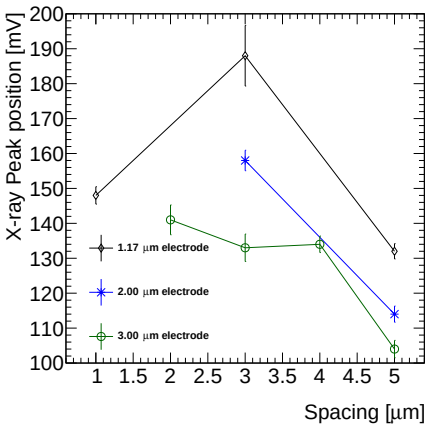


**(d)** *Effect of spacing size, pixel size 28µm, electrode size as stated*

**Figure 6.8.** *Effect of geometric parameters (a) on the signal size of the $k_{\alpha,Fe}$ peak. Pixel structures with different pixel sizes (b), electrode sizes (c) and spacing (d) had been measured.*

Among the 28 µm pixels, also structures with different spacing were measured. Data series for different electrode sizes are given in Figure 6.8d. The spacing has an impact on the gain of the pixel but there is no visible correlation between spacing and a maximum gain independent of the electrode size. Instead, the capacitance – and as result the gain – is a function of all geometric parameters.
The TJInv was used by the ALICE collaboration to analyse this parameter space in order to find optimal combinations for their upcoming upgrade and the same behaviours were observed: The signal size reduces with increasing size of the collection electrode. Using the multi-channel readout, a decrease of the average cluster size with increasing electrode size was observed due to stronger electrical fields in the volume. The impact of the spacing on the signal size showed no consistent trend but a local maximum. The average cluster size decreases with increasing spacing [56].

### 6.3.1. Charge sharing and its effect on the single-pixel spectrum

The geometric design of the pixel cell impacts on the signal gain as observed in the X-ray fluorescence measurements. Apart from the position of the $k_{\alpha,Fe}$ peak, also the shape of the signal spectrum depends on the parameters. The spectra of 28 µm pixels with different electrode sizes are shown in Figure 6.9.

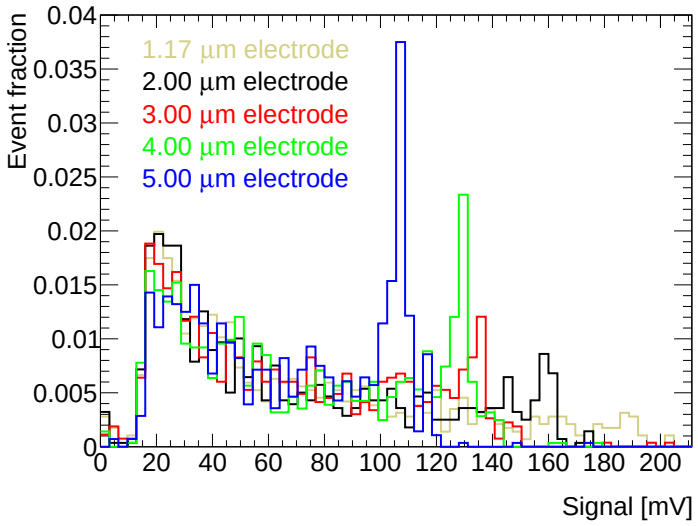


**Figure 6.9.** *Signal spectrum shape for different electrode sizes with area normalisation.*

With increasing electrode size, the ratio of events in the $k_{\alpha,Fe}$ peak increases. On one hand, this could be the result of a decreasing gain but an equal lower cutoff of the spectra. On the other hand, it could indicate an influence on charge sharing since the continuum of hits with lower energies is expected to contain signals shared between neighbouring pixels. At the time of these measurements, the readout was limited to single-pixel measurements by the number of available amplifiers.

Concerning the single-pixel spectra presented here, validating the effect of geometric parameters like electrode size on the electric field, charge collection and charge sharing in fine detail requires simulations of electric fields, penetration depths and crystal properties. For the interpretation of the observed spectra shapes with monochromatic peaks and a continuum of shared hits, a more simply plausibility test of the observed spectra can be based on a few assumptions:

- Penetration depth and vertical charge deposition is neglected. Instead, a 2d approximation is used.
- Charges are generated as a normalised charge cloud with 2d Gaussian density and Integral $I_c = 1$.
- The widths in both directions are identical: $\sigma_x = \sigma_y = \sigma_{cloud}$.
- The center position of a charge cloud is random and uniformly distributed.

- The charge collected by one electrode is the integral of the charge cloud over the pixel of size $d_{pixel}$, so the collected charge only depends on the pixel size.
- No charge loss is considered.
- The spectrum has a cutoff at a low value $x_{cut}$ (simulating a trigger threshold).
- Each signal is affected by Gaussian smearing $\sigma_{smear}$ (simulating energy resolution).

The application of these assumptions is shown in Figure 6.10. For each dataset, a combination of the parameters ($d_{pixel}$,$\sigma_{cloud}$, $x_{cut}$, $\sigma_{smear}$) is chosen. Out of scaling-invariance, all parameter sets with the same ratio $\frac{\sigma_{cloud}}{d_{pixel}}$ lead to the same result. This reduces the combinations to ($\frac{\sigma_{cloud}}{d_{pixel}}$, $x_{cut}$, $\sigma_{smear}$). The center of the charge cloud is chosen randomly over an area bigger than the pixel size, limited by the selected cutoff $x_{cut}$.

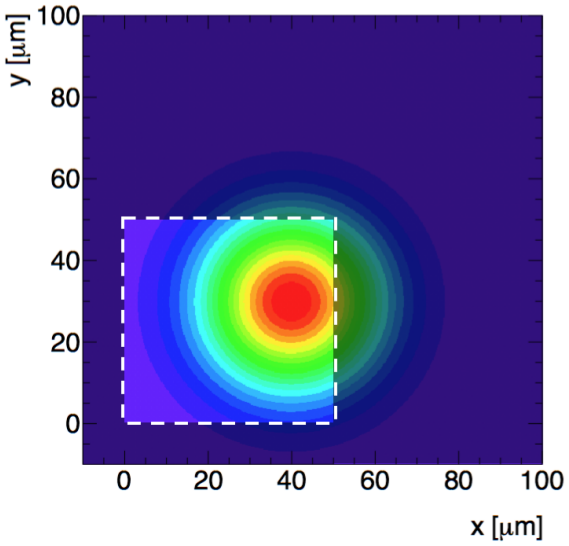


**Figure 6.10.** *Simulation of charge sharing. A central hit position is chosen randomly and a normalised 2d Gaussian with given width is calculated. The integral over the pixel area (indicated as light area) is taken as signal in the pixel if this signal exceeds a given threshold.*

The integral $I_{pixel}$ of the charge cloud over the pixel area is calculated and neglected for $I_{pixel} < x_{cut}$. As last step the calculated signal gets Gaussian smeared by adding a Gaussian random number of mean $\mu = 0$ and $\sigma_{smear}$, similar to the simulated noise in the previously presented fit validation procedure.

**$^{55}$Fe:** In the case of a photon, such as emitted by $^{55}$Fe, the produced charge cloud has a monochromatic energy. Additional lines are neglected and the energy of the line is normalised to one. Histograms of different datasets with equal $\sigma_{smear}$ are given in Figure 6.11a. For small values of $\frac{\sigma_{cloud}}{d_{pixel}}$, the peak is clearly visible around a signal value of $x = 1$.

Increasing the relative charge cloud size $\frac{\sigma_{cloud}}{d_{pixel}}$ leads to the expected increase of shared hits and decrease of peak height in the normalised histogram. In terms of the laboratory measurements, this corresponds to choosing smaller pixel sizes.

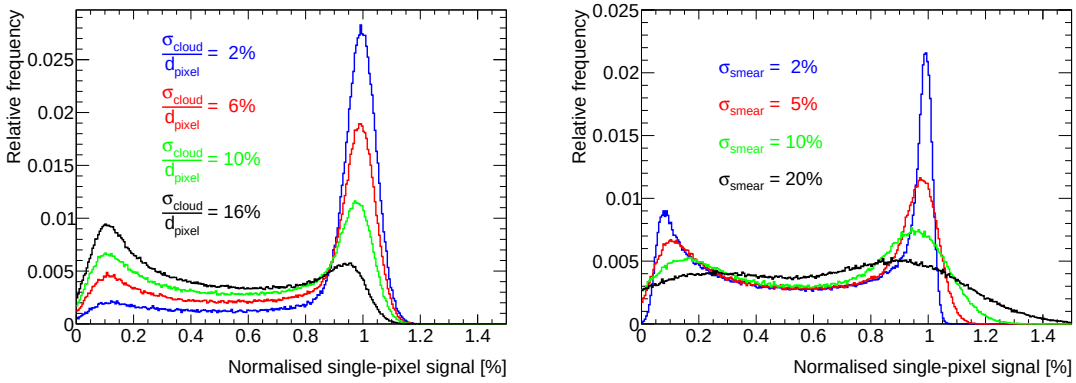


**(a)** *Simulated charge sharing in dependance of relative charge cloud size, $\sigma_{smear} = 5$ %*

**(b)** *Simulated charge sharing in dependance of energy resolution, $\frac{\sigma_{cloud}}{d_{pixel}} = 10$ %*

**Figure 6.11.** *Charge sharing simulation of $^{55}$Fe spectra. The shape of the distribution is affected by the relative charge cloud size (a) and the energy resolution of the sensor (b). In the first case the energy resolution was kept constant at 5%, in the second case the charge cloud size was kept constant at 10%.*

The influence of different energy resolutions is shown in Figure 6.11b. The relative cloud size is kept constant at 10 %. In addition to the expected effect of reducing the relative peak height, the position of the maximum gets shifted to lower values when the energy resolution gets worse.

**$^{90}$Sr:** The presented simulation assumes a Gaussian shaped charge cloud around a central point. This assumption is a better approximation for photons than for MIP-like particles traversing the sensor. In the case of MIP-like particles, the deposited energy is not monochromatic but a statistical value. Also the assumption of a fixed cloud size might no hold valid anymore. Still, the simulation can be used for a qualitative estimation of observed $^{90}$Sr spectra since the other assumptions – signal as integral of a charge cloud, low-value cutoff and limited energy resolution – are independent of the original particles.
As explained in section 3.3, an ideal MIP spectrum follows a Landau distribution. For the simulation of effects, random numbers are drawn out of a Landau distribution. They are then altered by a factor randomly drawn out of the normalised $^{55}$Fe simulations show in Figure 6.11. The simulated distributions as well as the used original Landau distribution are shown in Figure 6.12.

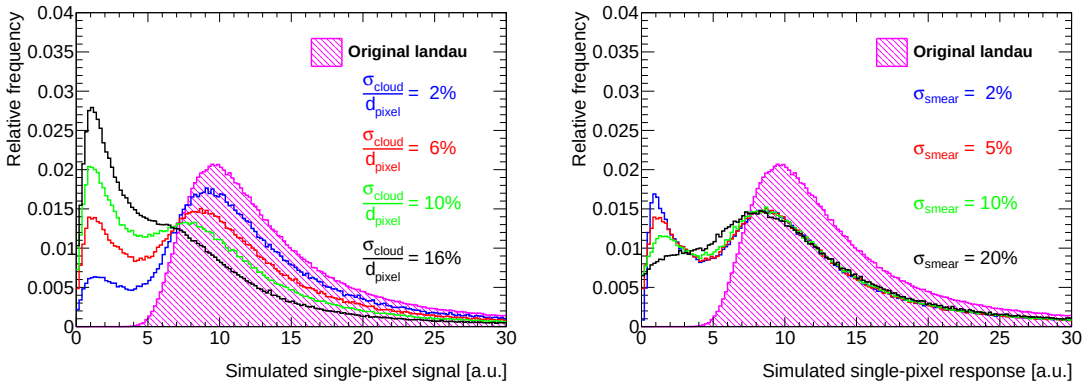


**(a)** *Simulated charge sharing in dependance of charge cloud size, $\sigma_{smear} = 5\%$*

**(b)** *Simulated charge sharing in dependance of energy resolution, $\frac{\sigma_{cloud}}{d_{pixel}}$=6%*

**Figure 6.12.** *Charge sharing simulation of $^{90}$Sr spectra. The shape of the distribution is affected by the simulated charge cloud size (a) and the simulated energy resolution of the sensor (b). In the first case the energy resolution was kept constant at 5%, in the second case the charge cloud size was kept constant at 6%. The used original Landau distribution is added.*

As observed before in the $^{55}$Fe spectra, a rising contribution of shared hits for higher relative cloud sizes can be observed in Figure 6.12a. With increasing charge sharing the position of the local maximum moves to smaller values. Whereas the peak of the $^{55}$Fe spectrum was still visible for $\frac{\sigma_{cloud}}{d_{pixel}} = 16\,\%$, the local maximum of the $^{90}$Sr spectrum almost completely fuses with the rising contribution of shared hits due to the initially broader Landau shape. Despite the visible distributions, the distributions seem to coincide at around 0.7 MPV.
Figure 6.12b shows the impact of energy resolution on the obtained spectra for a fixed cloud size of 6 %. Unlike the $^{55}$Fe spectra above, the peak position of the distribution is more robust, even up to $\sigma_{smear} = 20\,\%$.

The simulations presented here are made using simplified assumptions. Calculated charge sharing and energy resolution have different effects on the observed spectra. Whereas the spectra of $^{55}$Fe are more affected by the energy resolution, the gain information can still be extracted in case of high charge sharing. The peak position remains relatively stable. The opposite holds true for the $^{90}$Sr spectra. The information of the MPV is more robust against a decrease in energy resolution. Charge sharing on the other hand alters the shape of the distribution and the position of the local maximum. This has to be taken into account when interpreting $^{90}$Sr spectra of smaller pixel sizes in case of strong charge sharing.
With respect to the X-ray fluorescence measurements discussed in the previous section, it is to mention that the simulated spectra resemble energy spectra of the collected charge. In the case of HG structures a comparison to recorded signal spectra has to consider the compression of the tail due to the saturation region.

### Charge sharing for different pixel sizes

The basic simulations show the effect of different $\frac{\sigma_{cloud}}{d_{pixel}}$ ratios in the obtained signal spectra. Results of $^{55}$Fe source measurements for pixels from 20 µm size up to 50 µm size on an unirradiated chip are shown in Figure 6.13a. The normalised distributions for M112 and M124 are additionally descaled by a factor of four to enhance visibility.

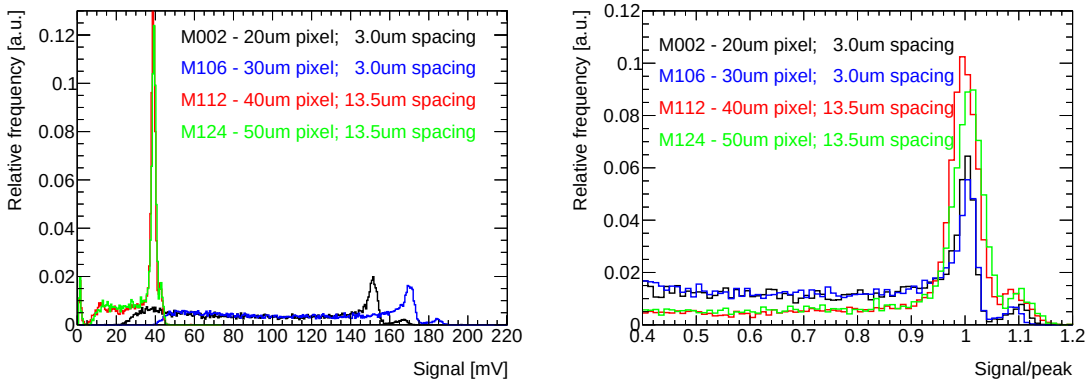


**(a)** *Signal spectra for different pixel sizes (normalised, then descaled by a factor of 4 for M112 and M124)*

**(b)** *Spectra normalised regarding the peak position*

**Figure 6.13.** *$^{55}$Fe results of the Standard Process before irradiation. The signal spectra for different pixel structures (a) show a different amount of shared hits. After normalisation with respect to the peak position (b), shape differences become more visible.*

The difference in gain is clearly visible in the $^{55}$Fe spectra as seen before in the fluorescence measurements. Concerning the shape of the normalised spectra, the ratio of hits in the main peak is significantly higher for the larger pixels (40 µm and 50 µm) than for the smaller pixels (20 µm and 30 µm) and the continuum of shared hits is reduced. Apart from the bigger pixel size, the structures M112 and M124 also have a bigger spacing (13.5 µm compared to 3 µm) than the structures M002 and M106. In Figure 6.13b, the spectra are scaled horizontally to a $k_\alpha$ peak position of 1 and normalised in the interval [0.4:1.2] to compensate for gain differences and threshold effects. In this diagram, the differences between different pixel sizes seem negligible whereas the spacing has an effect on the shape of the spectrum.
Beyond this, single pixel spectra are not sufficient to determine cluster characteristics like cluster size and cluster charge. For these measurements, multichannel setups reading out a grid of pixels simultaneously are needed.

## 6.3.2. Signal rise time

The MPV position in the converted $^{90}$Sr energy spectrum in Figure 6.3 indicates full vertical depletion. A high level of depletion is important to fulfil the requirements for fast and uniform signal detection.

The corresponding distribution of signal rise time for the 50 µm pixel structure of the Standard Process before irradiation is shown in Figure 6.14a. The distribution is Gaussian shaped with a peak position of (20±3) ns. The low peak position – small absolute collection time – equals a high mobility and is important to reduce the trapping probability and ensure radiation hardness. The narrow width of the distribution is important for the mapping of a particle hit to a specific bunch crossing in the detector.

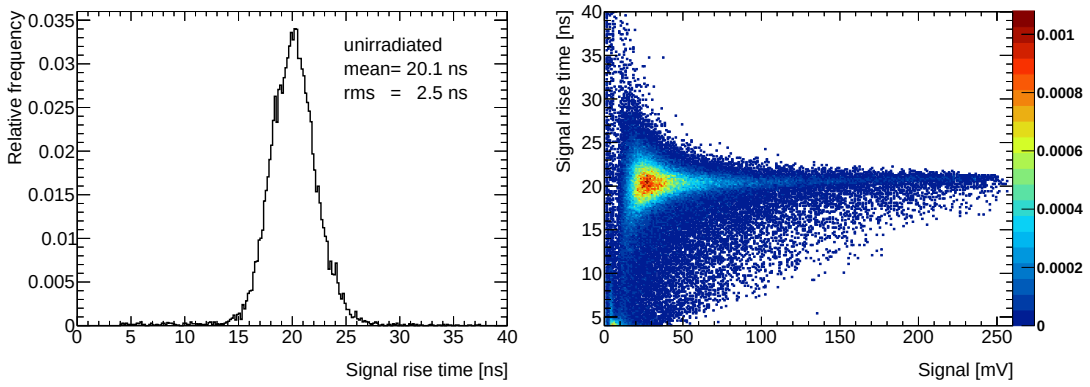


**(a)** *$^{55}$Fe signal spectrum* **(b)** *$^{90}$Sr signal spectrum*

**Figure 6.14.** *Signal rise time of $^{90}$Sr for a 50 µm pixel structure before irradiation (a) and correlation with the energy spectrum (b).*

Figure 6.14b shows the correlation of both the energy spectrum and time distribution in the 2d plane. In both the 1d and 2d diagrams, no signal contribution with high signal rise time is observed. Since charge collection by drift is significantly faster than charge collection by diffusion, this indicates charge collection only by drift for the applied $HV = -6\,\mathrm{V}$. The triangular shape of the 2d distributions agrees with the noise studies presented in chapter 5. The timing resolution of the fit is a linear function of S/N in case of Gaussian noise. Having a noise level independent of the signal results in the observed shape.

## 6.4. Sensor performance after irradiation

At the beginning of the ATLAS TowerJazz project, it was already established that the TJInv sensors produced in the Standard Process work before irradiation and after irradiation to $1.7\times10^{13}\,\mathrm{n/cm^2}$. This level of NIEL damage was the requirement for the ALICE ITS upgrade and the feasibility of the technology was proven [33]. For the ALICE ITS, full depletion and charge transport by drift are not required. Regarding the outer layers of the future ATLAS ITk on the other hand, higher requirements are in place as mentioned before. In order to test these requirement, sensors were neutron irradiated to higher fluences in the TRIGA reactor in Ljubljana, Slovenia.

### 6.4.1. Irradiation campaigns at the TRIGA reactor in Ljubljana

The TRIGA reactor at the Jožef Stefan Institute in Ljubljana, Slovenia, is a research reactor and was used to irradiate TJInv sensors. The irradiation was done in the F19 irradiation channel [57]. Sensors of the Standard Process were irradiated to different fluences, an overview is given in Table 6.1. The fluences are scaled to 1 MeV neq, the uncertainty on the obtained fluences is estimated to be 10 %.

**Table 6.1.** *Overview of fluences for sensors of the Standard Process: Only selected irradiation steps were analysed in the context of this thesis.*

| Fluence scaled to 1 MeV neq | Included |
|---|---|
| $1.7\times10^{13}\,\mathrm{n/cm^2}$ | – |
| $4.0\times10^{13}\,\mathrm{n/cm^2}$ | – |
| $1.0\times10^{14}\,\mathrm{n/cm^2}$ | X |
| $2.0\times10^{14}\,\mathrm{n/cm^2}$ | – |
| $4.0\times10^{14}\,\mathrm{n/cm^2}$ | – |
| $1.0\times10^{15}\,\mathrm{n/cm^2}$ | X |

For the irradiation, bare sensors were packed and inserted into the reactor. After letting he activation level cool down for several days, the sensors were shipped to CERN, glued onto carrier boards and connected with wire-bonds. After irradiation, sensors were stored and measured at cold temperatures and in dry-air environments.

### 6.4.2. Gain and charge collection after irradiation

Like the comparisons between pixel structures of different geometric properties, the effect of neutron irradiation is investigated by comparing the signal spectra of $^{55}$Fe and $^{90}$Sr. After irradiation, the leakage current at room temperature is significant and prohibits triggering on the signal itself. Therefore, the measurements were performed in a climate chamber at −30 °C to suppress leakage current in the irradiated samples. For comparison, also unirradiated sensors were measured at −30 °C.
The obtained signal spectra for the 50 µm pixel structure M129 before and after irradiation to $1.0\times10^{14}\,\mathrm{n/cm^2}$ and $1.0\times10^{15}\,\mathrm{n/cm^2}$ are shown in Figure 6.15.
The sensor irradiated to $1.0\times10^{14}\,\mathrm{n/cm^2}$ stayed functional and clear signals and spectra were obtained. The signal spectra of $^{55}$Fe show a gain reduction of around 10.0 % after $1.0\times10^{14}\,\mathrm{n/cm^2}$. The energy resolution worsens by a factor of 1.4 compared to the unirradiated sample. This leads to the $k_\alpha$ and $k_\beta$ peaks being fused completely. The sample irradiated to $1.0\times10^{15}\,\mathrm{n/cm^2}$ only shows a minor further reduction but the energy resolution worsens by a factor of 4.9 compared to the unirradiated sample and by 3.8 compared to the sample irradiated to $1.0\times10^{14}\,\mathrm{n/cm^2}$.

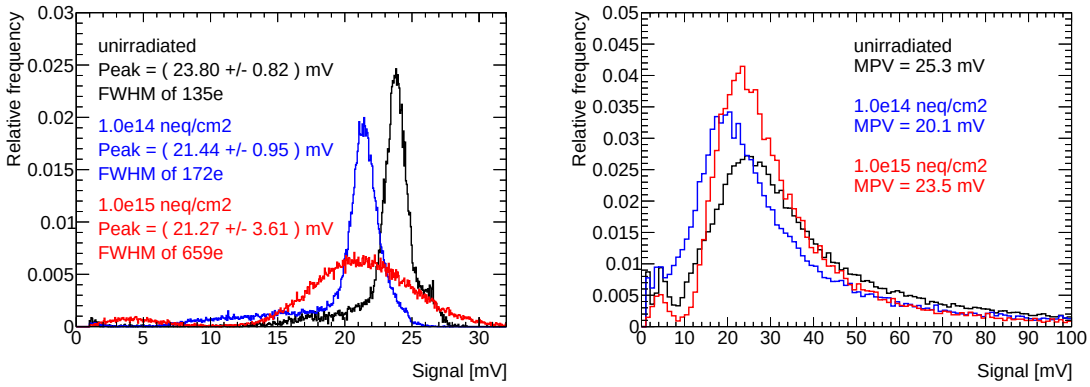


**(a)** $^{55}Fe$ *signal spectrum* **(b)** $^{90}Sr$ *signal spectrum*

**Figure 6.15.** *Signal spectra of $^{55}Fe$ (a) and $^{90}Sr$ (b) for a 50 µm pixel structure before irradiation in black, after irradiation to $1.0\times10^{14}$ n/cm$^2$ in blue and after $1.0\times10^{15}$ n/cm$^2$ in red. All measurements were performed at -30°C.*

Comparing the $^{90}$Sr signal spectra before and after irradiation to $1.0\times10^{14}$ n/cm$^2$, the MPV signal position decreases by almost 21 %. The distribution seems compressed as a result of the gain decrease. The MPV signal position for the sample irradiated to $1.0\times10^{15}$ n/cm$^2$ is in between the values of the other two samples.
position of the MPV signal position.
The signal spectra are now normalised with respect to the $^{55}$Fe peak position as discussed before. The linear transformation rescales the spectra into energy spectra to enable shape comparisons and an estimation of the MPV positions. The result of this transformation is given in Figure 6.16.

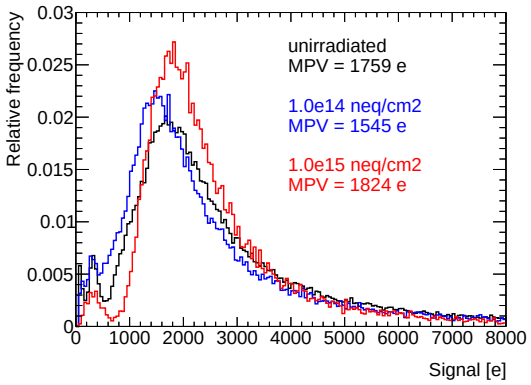


**Figure 6.16.** *Converted energy spectra of $^{90}Sr$ for a 50 µm pixel structure M129 before irradiation in black, after irradiation to $1.0\times10^{14}$ n/cm$^2$ in blue and after $1.0\times10^{15}$ n/cm$^2$ in red.*

After conversion into energy spectra, the differences between the unirradiated sample and the $1.0\times10^{14}$ n/cm$^2$ sample reduce as expected. The collected charge of 1545 e agrees very well with the expected MPV for a 25 µm depletion thickness of 1575 e [39]. This result is a strong indication that the sensor of the Standard Process can keep full vertical depletion of the epitaxial layer even after an irradiation of $1.0\times10^{14}$ n/cm$^2$.

For the highest irradiated sample, an MPV value of 1824 e is estimated. This value exceeds the value of the unirradiated sample by 3.7 %. Despite the high signals, this sample showed a very low hit rate, indicating a reduced lateral coverage of the depletion zone. Further measurements on the depletion zone and behaviour of the sample were performed with other techniques as described later.

### 6.4.3. Signal rise time after irradiation

The corresponding distributions of signal rise times for the $^{90}$Sr measurements presented before are given in Figure 6.17. After $1.0\times10^{14}$ n/cm$^2$, the signal rise time decreases from 20.1 ns to 17.3 ns. This decrease is within the timing resolutions of the distributions but still a visible shift. For both sensors, the signal rise time is Gaussian distributed with a narrow width below 3 ns.

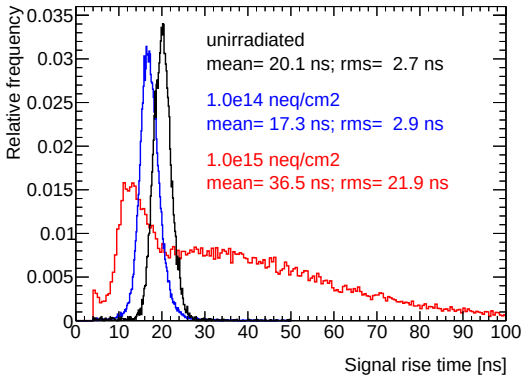


**Figure 6.17.** *Signal rise time of $^{90}$Sr for a 50 µm pixel structure before irradiation in black, after irradiation to $1.0\times10^{14}$ n/cm$^2$ in blue and after $1.0\times10^{15}$ n/cm$^2$ in red.*

The signal rise time of the sensor irradiated to $1.0\times10^{15}$ n/cm$^2$ appears to be the combination of a very fast component – peaking at around 12 ns – and a slower continuum that reaches a maximum around 35 ns and contains a long tail over 100 ns, failing the requirements for the ATLAS ITk. The fast component agrees with the previous observation of decreasing signal rise time and increasing width due to lower S/N. A similar separation was observed for unirradiated sensors when applying a low value for $HV$ as seen in Figure 6.2b on page 53. A possible explanation is the assumed sever degradation in lateral depletion: Particle hits near the collection electrodes experience a high electric field and create fast signals. Particle hits further away – if still close enough to be detected – experience significantly lower fields, creating slow signals.

Correlations between signal rise time and signal are shown in Figure 6.18. After irradiation to $1.0\times10^{14}$ n/cm$^2$, the correlation still has a visible triangular shape as expected. The observations of the 1d distributions – lower signals and lower signal rise times – seem not to relate to certain areas but the entire distribution. After irradiation to $1.0\times10^{15}$ n/cm$^2$, the correlation has a totally different shape.

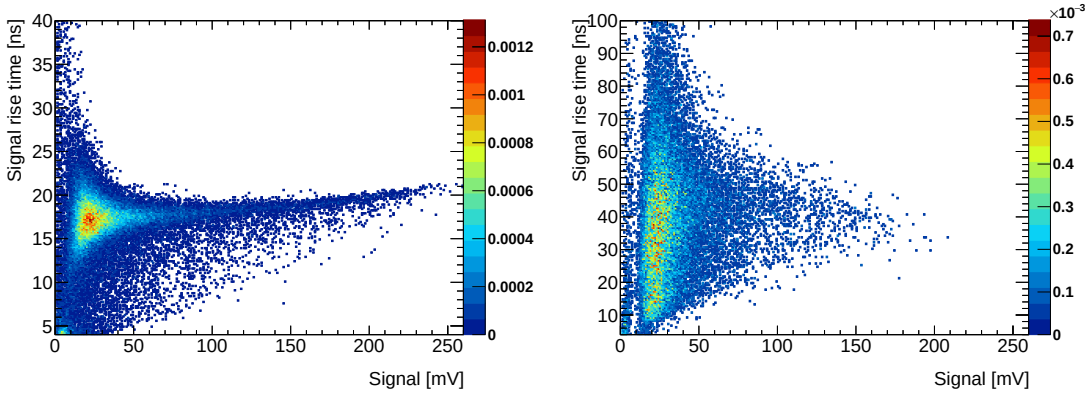


**(a)** $1.0{\times}10^{14}\,n/cm^2$ **(b)** $1.0{\times}10^{15}\,n/cm^2$

**Figure 6.18.** *Correlations between signal rise time and signal for a 50 µm pixel structure after $1.0{\times}10^{14}$ $n/cm^2$ (a) and after $1.0{\times}10^{15}$ $n/cm^2$ (b).*

The triangular effect of S/N is roughly visible but the majority of hits is spread out both in signal size and especially in signal rise time. The two contributions which appear to form the signal rise time distribution are not separate in the 2d area. Comparing the shape with the mentioned shape for low biasing, the results hint to the fact that the irradiated sensor is barely depleted even for $HV = -6\,\mathrm{V}$. Since the converted $^{90}$Sr energy spectra still indicates a certain level of vertical depletion, the horizontal depletion might be significantly affected. In order to study this further, a space-resolved measurement method is needed. Additionally, the count rates decreased and indicated a reduction in efficiency. But considering the higher leakage current and change in threshold settings, dedicated efficiency measurements with a reference telescope were performed.

## 6.5. Efficiency measurements – Standard Process

Laboratory measurements with radioactive sources give important results on signal shapes, signal rise times and charge collection. In order to characterise the performance and potential of a sensor, further information is needed which cannot be obtained in such setups. A sensor is required to keep a high charge-collection and hit-detection efficiency over its entire surface. These parameters are measured in testbeam environments using a particle beam passing through the sensor and a reference telescope to obtain the position information of the particle interaction. The TJInv has been tested in 2016 at the H8 beamline in the CERN SPS North Area.

**CERN SPS North Area - H8 beamline** The second-largest machine at CERN, the SPS serves as accelerating stage before the LHC. Receiving protons from the Proton Synchrotron (PS) with an energy of 25 GeV/c, their energy is further increased and they are then either filled into the LHC or transferred to other facilities, the CERN SPS North Area being one of them.

Here, four beam lines are available to test detector components with the primary proton beam or with secondary beams. These secondary beams are created when the primary beam hits a target. All CERN SPS testbeam measurements presented in this thesis had been performed with secondary pion beams of 180 GeV/c [39].

**AIDA SBM FE-I4 telescope** The AIDA SBM FE-I4 telescope was built by members of the local CERN group throughout 2014 [16]. A picture of the telescope is shown in Figure 6.19.

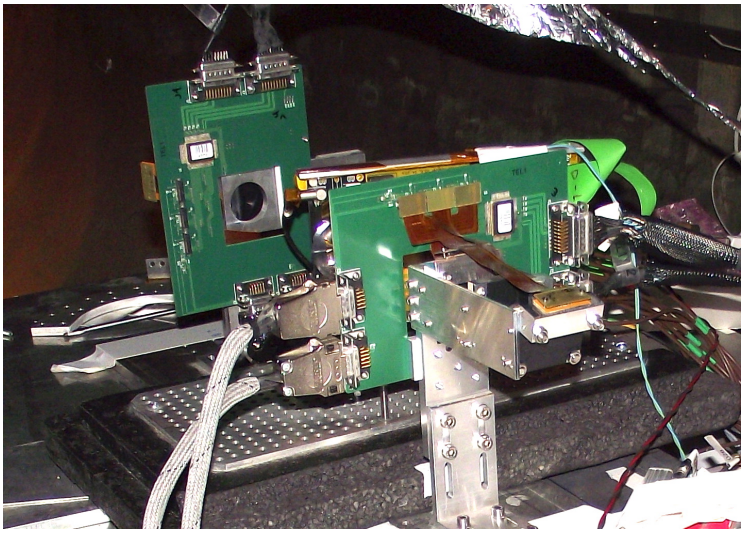

**Figure 6.19.** *AIDA SBM Fe-I4 telescope. The DUT is positioned between the two telescope arms. Each arm consists of three FE-I4 modules of which the inner one is rotated by 90° and the outer ones are tilted by 15°. The second arm is additionally rotated by 90° with respect to the first one.*

The telescope contains six single-chip FE-I4B modules mounted on two telescope arms. Each module contains pixels of 50 µm×250 µm pixel size in an active area of around 2 cm×2 cm. The asymmetry is compensated by rotating the middle module of both arms by 90 ° with respect to the outer ones and then rotating one arm by 90 ° with respect to the other one. The outer modules of each arm are then additionally tilted by 15 ° around the axis of its long pixel direction. Using charge sharing and hit-position interpolation, the resolution is enhanced further. This way, a resolution in the order of 8–9 µm in both the horizontal and vertical direction can be achieved [16, 39].
During the 2016 CERN SPS testbeam only five modules were working and arranged to have three upstream and two downstream modules, leaving the last position without working module. This resulted in a slight asymmetry in resolution of 11.6 µm in $x$ and 12.2 µm in $y$.
The **D**evice **U**nder **T**est (DUT) – in this case the TJInv – is positioned in the centre of the telescope between both arms. Beam particles pass through the modules of the first arm, then the DUT, and finally the modules of the second arm. By recording and analysing the hits in the telescope modules, the particle trajectory is reconstructed.

**DUT setup** By recording the signals of the telescope and the ones of the DUT at the same time, the information can be linked and a position-sensitive dataset of DUT events is obtained. The Time-precision setup has been modified to read out multiple channels simultaneously in the CERN SPS testbeam. Three DRS4 oscilloscopes were connected in series and read out together. The first DRS4 serves as master being configured in a standard way. The two other DRS4 serve as slaves and record hits together with the master. This way, up to twelve channels can be recorded at the same time. Out of these twelve channels, one channel was needed to receive the trigger veto signal. Out of the remaining eleven channels, only four channels were equipped with external cividec amplifiers. The four channels were chosen to form a 2×2 pixel area as shown in Figure 6.20. This way, the interconnection of four pixels is at the center of the sensitive area. Since this part of the pixel cell has the biggest distance to collection electrodes, charge collection and therefore hit-detection efficiency are most sensitive to failing depletion after irradiation at this location.

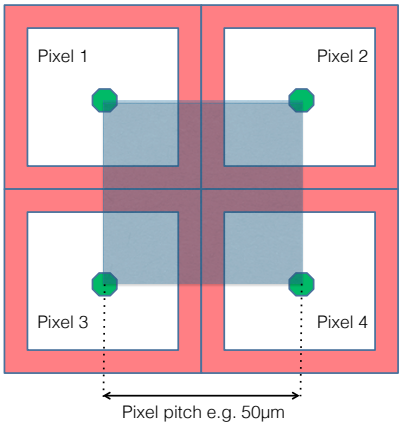


**Figure 6.20.** *2×2 pixel configuration to optimally use the four available cividec amplifiers: The interconnection of four pixels has the biggest distance to collection electrodes and is expected to be most sensitive to failing depletion after irradiation.*

**Trigger scheme** Both setups – AIDA telescope and TJInv readout – are run separately. Trigger signals between both setups enable the simultaneous readout of telescope hits and the corresponding hits in the DUT. The trigger scheme is explained in Figure 6.21. Each telescope arm is equipped with a "Hitbus chip". In this chip, the hit signals of all planes in this arm can be combined with simple gate logic. During operation, the first two modules of the telescope (the most upstream ones) serve as initial trigger planes. Each single-chip FE-I4B module has 80×336 pixels in an area of 2 cm×2 cm. Since our DUT area is only around 200 µm×200 µm in case of testing big pixels, a **R**egion **O**f **I**nterest (ROI) can be defined for each trigger plane. All pixels of the plane are read out but only pixels inside the ROI are used for triggering. A logic AND gate in the chip sends a trigger pulse only in the case of coinciding hits in the ROIs of the first two planes.

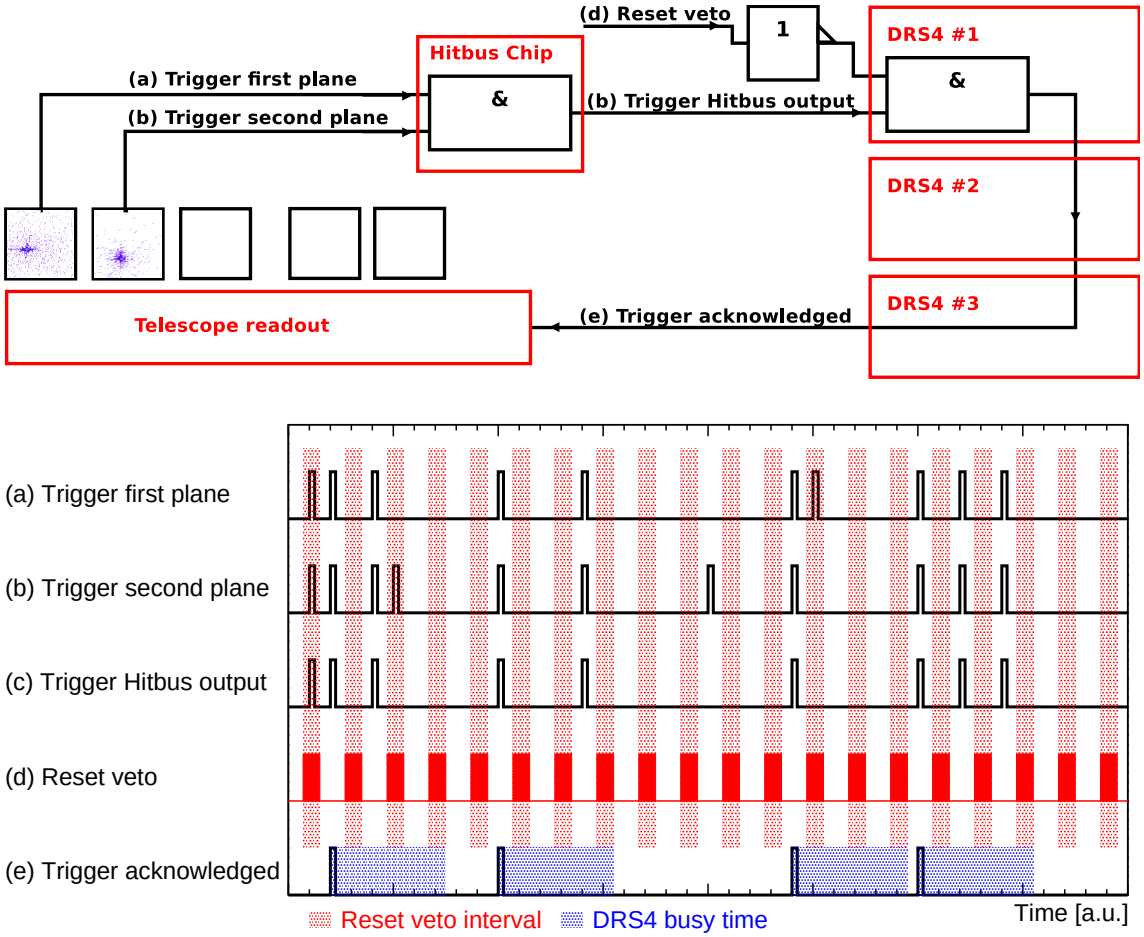


**Figure 6.21.** *Trigger scheme of the CERN SPS Testbeam, signals are sent in clockwise direction. Triggers in the ROIs of the first two planes (a,b) are processed by the Hitbus chip applying an AND gate (c). The DRS4 ignores triggers in the reset veto interval (d) and only sends triggers for events that are stored when it is not busy (d). This "trigger acknowledged" signal (e) is used by the telescope readout to store the information of all planes (five during the 2016 testbeam campaign).*

This pulse is then sent to the master DRS4. As before during source scans, hits coinciding with the reset interval are neglected since they cannot be analysed. The DRS4 has a limited rate for stored events per second. The manual speaks of about 500 Hz per number of boards. After each recorded event, the DRS4 is busy for some time and ignores incoming trigger pulses.
Only for successfully stored events the trigger output of the DRS4 transmits a pulse further. This trigger pulse is sent along the chain and all DRS4 channels are stored into one file. Since both trigger veto and DRS4 event rate limitation reduce the number of stored DUT hits with respect to the initial triggers sent by the Hitbus, this trigger pulse of the last DRS4 is used as a 'trigger acknowledged' signal. It is sent back to the telescope setup to trigger the storage of telescope events.

Closing this loop enables both files to contain the same amount of events by ignoring the telescope events without stored equivalent in the DRS4. The synchronisation of the events stored in both files is done offline using event timestamps.

As indicated in the trigger scheme, the limited event rate of the DRS4 chain is the main bottleneck in the setup. Different measures are in place to maximise the data rate of the setup: Not all hits on the entire first two planes are used for triggering. Instead, a very small ROI is defined. This way, particles that cannot hit the DUT are excluded in the first place. A further measure is to exclude hits during the reset of the pixel cell already online during data taking. The desired properties of the pion beam are high intensity and high focus to maximise particle density in the small are of the DUT.

**Cooling** Irradiated samples are measured at low temperatures to reduce the leakage current and prevent annealing. Figure 6.22 shows the closed cooling box positioned between both telescope arms.

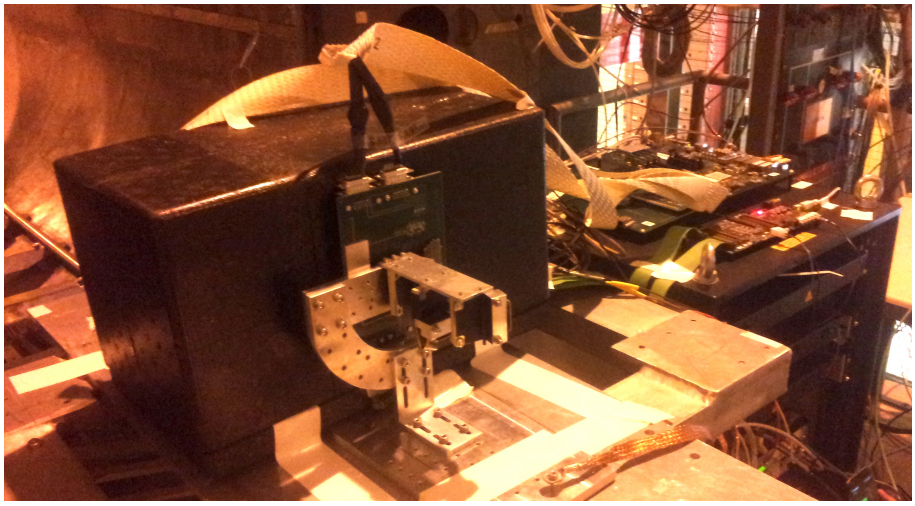

**Figure 6.22.** *The cooling box for sensor and TJInv adapter board is positioned between both telescope arms. The box has two separate compartments. On the right hand side, dry ice is used to cool down the inside of the box. On the left-hand side, the compartment containing the sensor and the TowerJazz adapter board is flushed with dry air to prevent condensation.*

The components of the setup that had been positioned inside the climate chamber are now fixed inside the cooling box. The box has a second compartment that is filled with dry ice. External supply of dry air prevents condensation on the sensor.

**Efficiency calculation and corrections** The efficiency of the DUT is the ratio of the number of events with reconstructed telescope tracks and a valid sensor hit to the number of all events with reconstructed telescope tracks as given in Eq. (6.2):

$$\eta_{uncorrected}(x,y) = \frac{n_{\text{Tracks with DUT hit}}(x,y)}{n_{\text{All tracks}}(x,y)} \tag{6.2}$$

Since the acceptance area of the DUT consists of only four pixels which are read out simultaneously, edge effects and the pointing resolution of the telescope of around 9 µm influence the efficiency measurements. A simulation has been performed to estimate the influence of this pointing resolution on a perfect sensor [39]. As shown in Figure 6.23a, the measured efficiency drops to 50 % in the middle of the edges of the acceptance area and down to 25 % in the corners where four pixels are connected.

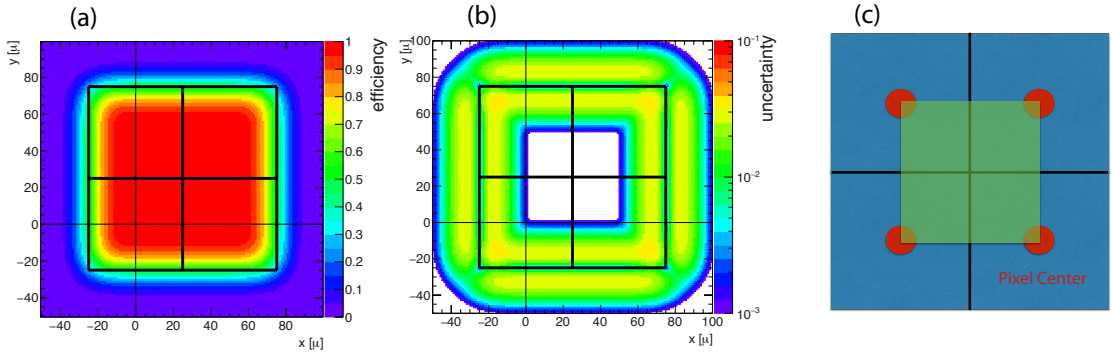


**Figure 6.23.** *Efficiency correction due to a finite telescope resolution (a) and estimated uncertainty of the correction (b). The pixel area under investigation (c) is least affected by the finite resolution [39].*

The drop in expected efficiency is caused by hits outside the area which get misreconstructed inside the area due to the telescope resolution. As seen in the map, this effect is most significant on the corners and edges whereas the correction in the center of the acceptance area is almost zero for pixels of 50 µm size. For smaller pixel size, the effect increases. As mentioned before, only five out of the six AIDA SBM telescope planes were functioning during the testbeam campaign. For the calculation of the correction map this difference between horizontal and vertical resolution is taken into account. Figure 6.23b shows an estimation of the correction uncertainty obtained by a ±1 µm variation to the telescope resolution. This uncertainty is treated as systematic uncertainty. The obtained corrected efficiency for a position $(x, y)$ is given in Eq. (6.3):

$$\eta_{corrected}(x,y) = \frac{n_{\text{Tracks with DUT hit}}(x,y)}{n_{\text{All tracks}}(x,y)} \cdot \frac{1}{\eta_{ideal}(x,y)} \tag{6.3}$$

### 6.5.1. Testbeam results of the Standard Process after irradiation

Unirradiated TowerJazz sensors produced in the Standard Process were not tested with the AIDA SBM FE-I4 telescope. Their efficiency was tested and presented by other groups investigating the technology [58]. The efficiency of the TowerJazz technology using a Standard Process design after (irradiation to $1.7\times10^{13}$ n/cm$^2$, the requirement for the ALICE ITS Upgrade) was further tested with the ALICE Alpide chip, which is currently in production for the ALICE upgrade [38].

As mentioned before, the requirements for the outer layers of the ATLAS ITk are set to $1.5\times10^{15}\,\mathrm{n/cm^2}$. In this radiation regime, the two levels presented earlier – $1.0\times10^{14}\,\mathrm{n/cm^2}$ and $1.0\times10^{15}\,\mathrm{n/cm^2}$ – were also tested in the CERN SPS testbeam.

**Standard process after $10^{14}$ n/cm$^2$** The obtained results for structure M129 after $1.0\times10^{14}\,\mathrm{n/cm^2}$ is shown in Figure 6.24. The four recorded pixels are marked with black squares. The uncorrected efficiency map over the entire four-pixel area is given in Figure 6.24a. Within statistical fluctuations, the distribution agrees very well with the expected efficiency.

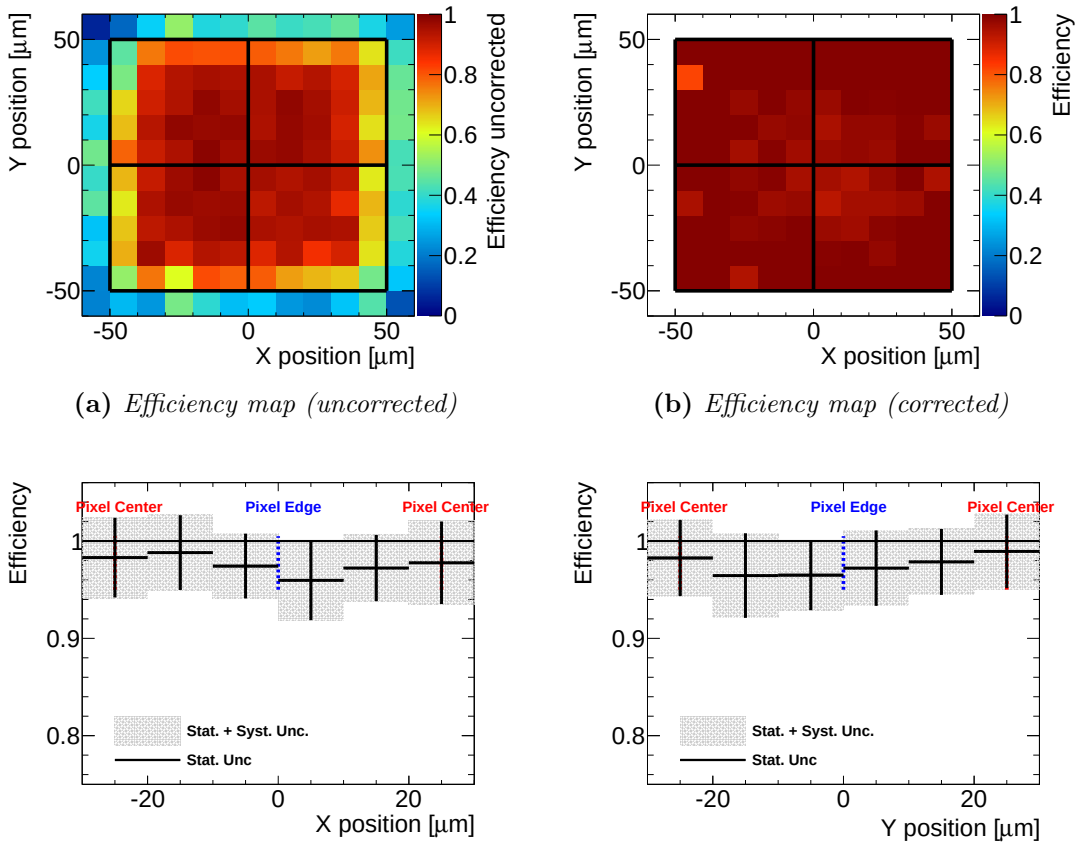


**(a)** *Efficiency map (uncorrected)*

**(b)** *Efficiency map (corrected)*

**(c)** *Efficiency projections in x (corrected)*

**(d)** *Efficiency projections in y (corrected)*

**Figure 6.24.** *Efficiency map over the entire four-pixel area before (a) and after applying the resolution correction (b) as well as efficiency projections of the central area in x-direction (c) and y-direction (d) for Standard Process 50 µm pixel after $1.0\times10^{14}$ n/cm$^2$.*

The corrected efficiency map is shown in Figure 6.24b. The efficiency is relatively constant over the entire pixel area. As mentioned before, the area of interest is the intersection of all four recorded pixels. Projections of the efficiency in this area are shown in Figure 6.24c and Figure 6.24d. Since the 2016 CERN SPS testbeam campaign mainly focused on sensors of the modified process (results in the next chapter), this measurement was done at the end of the campaign in little remaining time and does not contain high-statistic runs.

Regarding the center area, only 4500 tracks were reconstructed by the telescope, leading to high statistical uncertainties. The sensor shows an efficiency of 97.6 % ± 1.5 % (stat.) ± 0.6 % (syst.) with a slight drops around the middle of the four-pixel area. Still, the sensor is capable of collecting charge over its horizontal area within the uncertainties even after this level of irradiation.

Efficiency drops around pixel edges are a first indication for weaker horizontal depletion in this area. Another possible reason is charge sharing in combination with a low S/N: During this testbeam campaign, the setup suffered from higher noise than previously in the laboratory environment. Therefore, this noise is no intrinsic noise of the chip but the effect of external sources. As a result of this noise, higher threshold settings were used during the campaign. The investigated structure M129 is an LG structure. At the pixel edges and corners, charge sharing between the pixels leads in addition to smaller signals in each individual pixel.
Such an effect on the TJInv can only be tested by reducing the effect of external noise sources. Based on the observations during this testbeam campaign, modifications of the telescope setup were performed for future campaigns, including shielded cables and more integrated components.
Since the transport of analogue signals over cables is one of the main weaknesses, a future test chip that includes a digital front-end is expected to suffer less from external noise then the TJInv.

**Standard process after $10^{15}$ n/cm$^2$** The Standard Process sensor irradiated to $1.0\times10^{15}$ n/cm$^2$ was also measured in the SPS testbeam. Based on the laboratory source measurements shown before, a high efficiency was not expected and only a small amount of time invested, limiting the collected statistics. The center area contains only 2986 reconstructed tracks. The obtained results for a matrix of 50 µm pixel size after $1.0\times10^{15}$ n/cm$^2$ is shown in Figure 6.25.

Both the uncorrected and corrected efficiency maps show a structure in the four-pixel area. The efficiency is highest in the middle of each pixel at the location of the collection electrode, but even there the measured efficiencies are below 80 %. The projections in the $x$ and $y$ directions in Figure 6.25c and Figure 6.25d, respectively, show drops in efficiency below 50 %. Due to the radiation damage in the epitaxial volume, the depletion zone shrinks down around the collection electrodes. Here, partial charge collection is still possible. The average obtained efficiency over the central area is measured to be 56.6 % ± 1.9 % (stat.) ± 0.6 % (syst.). The severe degradation in efficiency is not limited to the pixel edges but also visible at the position of the collection electrodes. Unlike the sample irradiated to $1.0\times10^{14}$ n/cm$^2$, the effect is not only the result of charge sharing and a lower S/N.
The systematic uncertainty caused by the applied correction is small for the tested 50 µm structures. For a more precise measurement, a higher statistic is necessary.

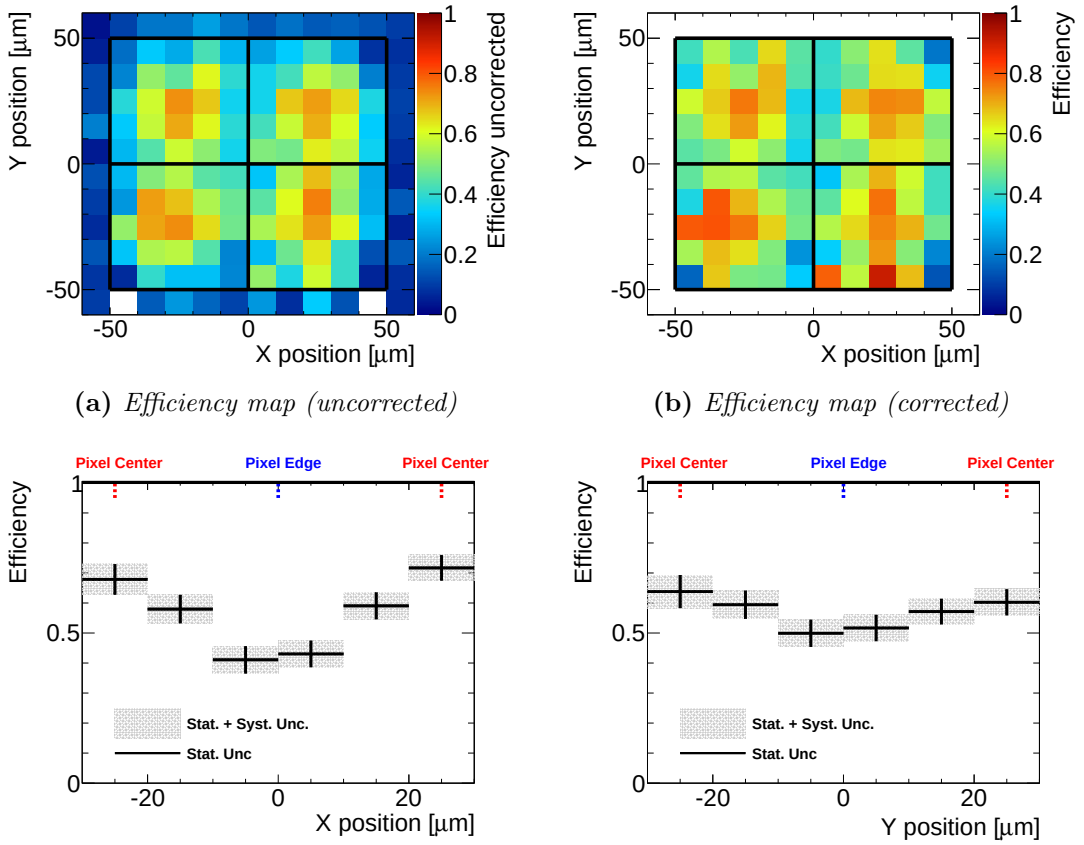


**(a)** *Efficiency map (uncorrected)*

**(b)** *Efficiency map (corrected)*

**(c)** *Efficiency projections in x (corrected)*

**(d)** *Efficiency projections in y (corrected)*

**Figure 6.25.** *Efficiency map over the entire four-pixel area before (a) and after applying the resolution correction (b) as well as efficiency projections of the central area in x-direction (c) and y-direction (d) for Standard Process 50 µm pixel after 1.0×10^15 n/cm^2.*

## 6.6. Summary

The Time-precision setup has been successfully used to measure the performance of TJInv sensors produced in the Standard Process before and after irradiation up to $1.0\times10^{15}$ n/cm$^2$. The working point of the setup was chosen based on scans of different values for $V_{\mathrm{RESET}}$ and the investigation of the transfer function of the internal source follower. The gain of a pixel as determined by the $k_\alpha$ peak position of the $^{55}$Fe source depends as expected on the capacitance of the pixel cell. This was confirmed in scans of the biasing $HV$ and in comparing pixel structures with different geometric properties. Regarding these properties, the structures were classified in LG and HG pixel structures. For LG structures, X-ray fluorescence measurements confirmed a linear conversion between signal spectra and energy spectra over a wide energy range to be reasonable. For HG structures, a saturation effect of the transistors in the internal source follower becomes visible. Since the expected value of the MPV in the $^{90}$Sr energy spectrum is close to the energy of the $^{55}$Fe peak, a linear conversion is considered sufficient to investigate a change in the amount of collected charge.

The shape of signal spectra and the identification of a continuum of shared hits below the monochromatic peak was simulated and motivated based on basic assumptions. Geometric properties show a greater impact than pixel size on the shape of the spectrum.

Source measurements confirmed depletion and fast signal rise time before and even after an irradiation to $1.0\times10^{14}\,\mathrm{n/cm^2}$. For a sensor irradiated up to $1.0\times10^{15}\,\mathrm{n/cm^2}$, severe degradation was visible. The position resolution of a CERN SPS testbeam campaign confirmed the failing horizontal depletion of this sensor at the pixel edges. The lower irradiated sensor already showed an overall drop in efficiency and a drop at the edges whereas the higher irradiated sample is heavily damaged in terms of fast charge collection and hit detection efficiency.

Based on the measurements presented here, TowerJazz sensors produced in the Standard Process are not capable of fulfilling the requirements of the future ATLAS ITk.

# 7. Performance of the Modified Process

Sensors of the TJInv produced in the Standard Process proved to work successfully before irradiation. The testbeam measurements presented in the last chapter showed first signs of degradation after $10^{14}\,\mathrm{n/cm^2}$. After $10^{15}\,\mathrm{n/cm^2}$, the hit-detection efficiency of the sensor as well as its signal rise time behaviour was measured to be not sufficient. Sensors of this process can not be considered for the ATLAS ITk.
As mentioned in Chapter 4, a process modification was designed to enhance the depletion after irradiation by adding an additional n-type implant. In this Chapter, measurements with sensors of the Modified Process are presented and the results are compared to the ones obtained for the Standard Process. First, the performance in the X-ray fluorescence setup and in source measurements before irradiation are compared. Second, the performance improvements after irradiation are presented, both in laboratory measurements and in the CERN SPS testbeam. Third, the amount of collected charge and potential charge loss are investigated further with a dedicated five-pixel cluster measurement. Here, structures with different horizontal dimensions of the deep p-well are measured to probe its impact and search for improvement options.
Concerning the low-dose n-type implant, all these measurements were performed for sensors with an identical doping concentration. As mentioned before, a second set of sensors with a lower concentration in the n-type implant was produced. The performance of both doping concentrations are compared in the next chapter.

## 7.1. Correlation of deposited energy and signal size

The sensors of the Modified Process were tested under the same conditions as the previously presented results of the Standard Process. The obtained transfer functions before irradiation for the Modified Process are given in Figure 7.1a the ones for the Standard Process in 7.1b. In both cases, the general shape agrees with the expectation of linear regions and saturation regions. The transfer functions of the Modified Process seem to be shifted to lower values of $V_{\mathrm{RESET}}$. Aside chip-to-chip variations, the readout is identical to the Standard Process and the shift is caused by the process modification. For structure M129 – classified as LG structure in the Standard Process – the working point is in a linear region. For the two HG structures, the point is slightly at the beginning of the saturation region.

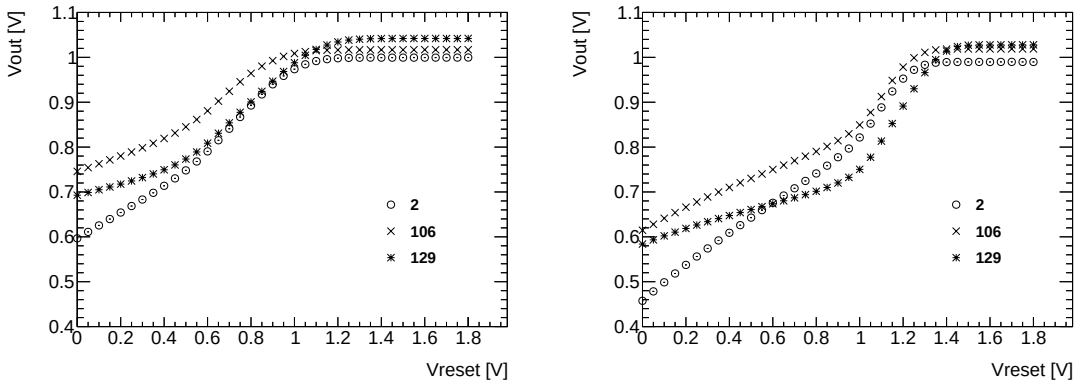


**(a)** *Transfer function - Modified Process* **(b)** *Transfer function - Standard Process*

**Figure 7.1.** *Transfer functions of the Modified Process (a) compared to the Standard Process (b) before irradiation.*

### 7.1.1. Linearity test using monochromatic fluorescence lines

A sensor produced in the Modified Process was also included in the X-ray fluorescence measurement campaign in Glasgow described in section 6.2.2. During the measurements with the Fe target, the wrong structures were selected and these data points could not be used. Only the four targets at higher energies – Cu, Se, Nb, Sn – are analysed. The obtained correlation of energy and signal is given in Figure 7.2.

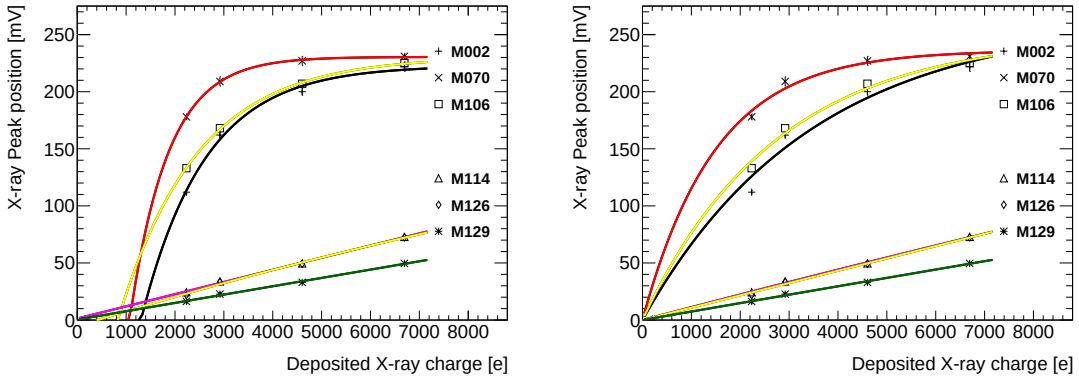


**(a)** *X-ray results - Fit with offset* **(b)** *X-ray results - Fit without offset*

**Figure 7.2.** *X-ray fluorescence measurements on unirradiated sensors of the Modified Process. The signal size of the $k_\alpha$ peaks of different pixels for four targets – Cu, Se, Nb, Sn – are shown. An exponential fit function with (a) and without (b) offset is added.*

The measured matrices fall into the same categories of LG and HG pixel structures as for the Standard Process. Since differences in gain between pixel structures seem to be determined by the geometric design parameters of the cell, this was expected. For the LG structures, the correlation can again be described using a linear approximation without offset as visible in Figure 7.2b.

Comparing to the Standard Process given on page 58, the slope representing the gain is significantly lower.
For the HG structures, the general shape of rise and saturation is the same as for the Standard Process. The saturation level seems to be a bit lower than observed before but measurements at even higher energies are needed to determine this.
As seen in the transfer function, both the linear rise and the begin of the saturation seem to be shifted to higher energies compared to the Standard Process, indicating a reduced gain. The chosen working point of $V_{\mathrm{RESET}} = 1\,\mathrm{V}$ is not at the end of the linear region but in the saturation region. In that case, small amounts of energies do not cause signals linearly but with a smaller gain. Since the measurements are calibrated with $^{55}$Fe, an energy very close to the expected MPV in case of full depletion, using the linear approximation for the HG structures is still sufficient for the determination of the MIP MPV. For the measurement of small charges, for example, the determination of cluster charges over several pixels, the linear approximation leads to an underestimation of the deposited energy. For charge-precision measurements, a shift of the working point to a linear region might be advantageous to avoid this effect.

## 7.2. Performance of the Modified Process before irradiation

The results of the X-ray fluorescence measurements showed a gain reduction compared to the Standard Process. This gain reduction is based on an increase of the pixel capacitance due to the additional interwell capacitances between the n-implant and the neighbouring structures. Signal spectra for the 50 µm pixel structure M129 at a bias voltage of −6 V are presented in Figure 7.3.

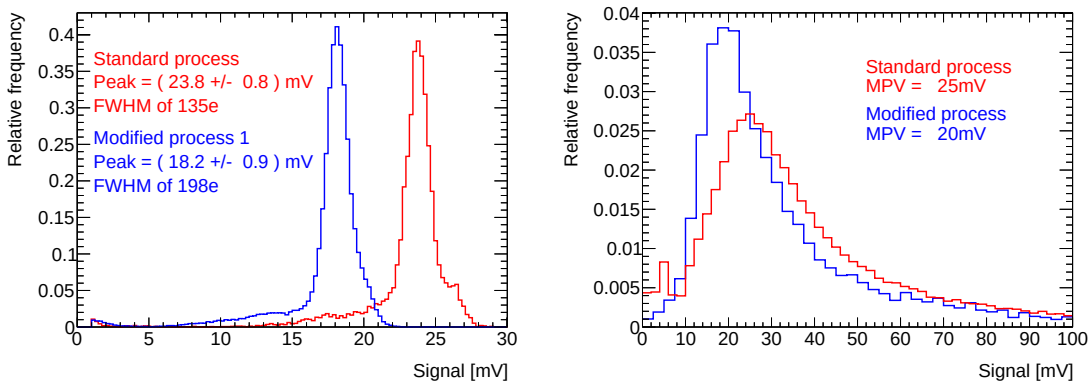


**(a)** *$^{55}$Fe signal spectra* **(b)** *$^{90}$Sr signal spectra*

**Figure 7.3.** *Signal spectra of $^{55}$Fe (a) and $^{90}$Sr (b) for the 50 µm pixel structure M129. A gain difference between the Standard Process in red and the Modified Process in blue is visible in both spectra.*

The position of the $^{55}$Fe peak reduces by around 24 % from 23.8 mV to 18.2 mV. Since the same charge $Q_{Fe}$ is deposited, the gain reduction indicates an estimated increase in capacitance of around $\left(\frac{C_m}{C_s} - 1\right) = \left(\frac{V_s}{V_m} - 1\right) = \left(\frac{26\,\text{mV}}{18\,\text{mV}} - 1\right) \approx 31\%$.

A similar reduction is visible in the $^{90}$Sr spectra in Figure 7.3b. Matrix M129 being a LG structure, the converted energy spectra in Figure 7.4a are without distortion over the observed energy range. The obtained MPVs of 1759 e for the Standard Process and 1732 e for the Modified Process agree. The observed reduction in signal is not caused by loss of charge but by the reduction in gain. As mentioned in the last chapter, an MPV of 1575 e is expected for a depletion thickness of 25 µm and the additional charges might be a contribution from the transition volume between epitaxial layer and substrate [39]. The results indicate a full vertical depletion also for the Modified Process.

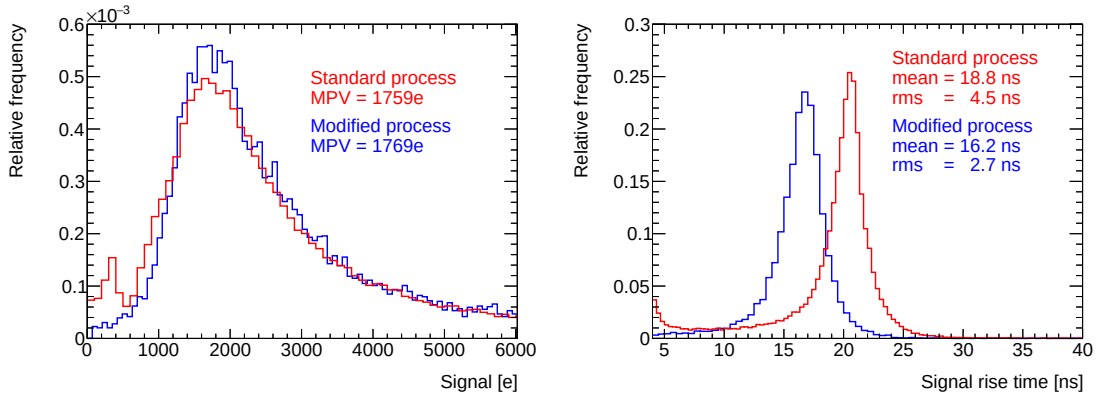


**(a)** *$^{90}$Sr energy spectra* **(b)** *Signal rise time distribution*

**Figure 7.4.** *Converted $^{90}$Sr energy spectrum (a) and signal rise time distribution (b) for unirradiated sensors of both processes.*

The distributions of the signal-rise time are given in Figure 7.4b. The mean value reduces from 18.8 ns for the Standard Process to 16.2 ns for the Modified Process. The rms of the distribution reduces from 4.5 ns to 2.7 ns caused by a longer tail for the Standard Process. The widths of the distributions are comparable. The reduction in time indicates a stronger depletion and stronger field in the pixel volume due to the creation of a horizontal pn-junction.

### Cluster measurements on 28 µm pixel structures

A gain reduction in a similar magnitude was also observed in the ALICE multichannel setup for a pixel size of 28 µm in structure M075 [45]. The obtained seed-pixel spectrum is given in Figure 7.5a below, the seed pixel being defined as the pixel in a cluster with the highest signal.

The seed signal spectrum is by definition expected to show a smaller contribution of small hits than the single-pixel spectra shown before. The spectra of cluster signals – sum of signals over all hit pixels – are given in Figure 7.5b.

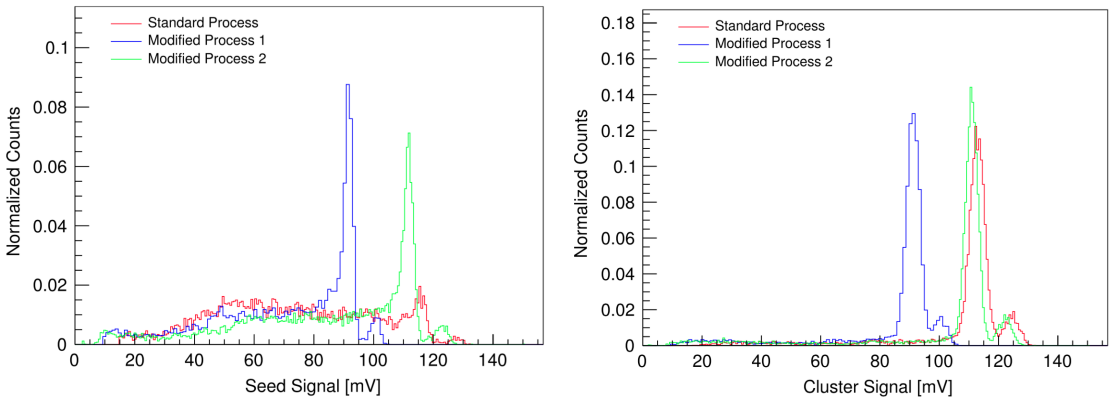


**(a)** *Seed signal spectra - multichannel setup*

**(b)** *Cluster signal spectra - multichannel setup*

**Figure 7.5.** *Seed signal spectra (a) and cluster signal spectra (b) of 28 µm pixels of unirradiated sensors recorded with the multichannel setup [45].*

'Modified Process 1' refers to a sensor with a "by several tens of percent" [45] higher doping concentration in the n-type implant than for 'Modified Process 2'. The measurements presented in this chapter were performed with sensors of 'Modified Process 1'. A comparison with 'Modified Process 2' is given in the following chapter. A significant signal size reduction of around 20 % between the Standard Process in red and 'Modified Process 1' in blue is visible in both the seed and cluster signal spectra. The shapes of the seed signal spectra show a significant reduction of the shared hit contribution in case of the Modified Process. As expected, this effect is more visible than for the spectra of 50 µm pixels shown before.
The cluster signal spectra of both processes show distinct $k_\alpha$ and $k_\beta$ peaks, confirming successful charge collection. The peak widths are higher than for the seed signal spectra due to the summation of the pixel noises.

Figure 7.6a shows the corresponding cluster size distributions. For the sensors of the Modified Process, charge sharing is significantly reduced and the number of pixels per cluster is lower than for the Standard Process.
Regarding the signal rise time distributions given in Figure 7.6b, the width of the distribution reduces as seen before. The mean of the distribution is lower for the Modified Process than for the Standard Process. The difference is not general but specifically for small shared hits. This shape difference is visible in the correlation between single-pixel signals and signal rise time for both processes in Figure 7.6c and 7.6d. The non-shared events in the peaks have a similar signal rise time of around 23 ns for both processes. The shared hits are caused by photons near pixel boundaries. For the Standard Process, these areas are more likely to be weakly depleted or undepleted. The additional charge transport by diffusion increases the signal rise time compared to the Modified Process and its charge transport by drift in depleted areas [45].

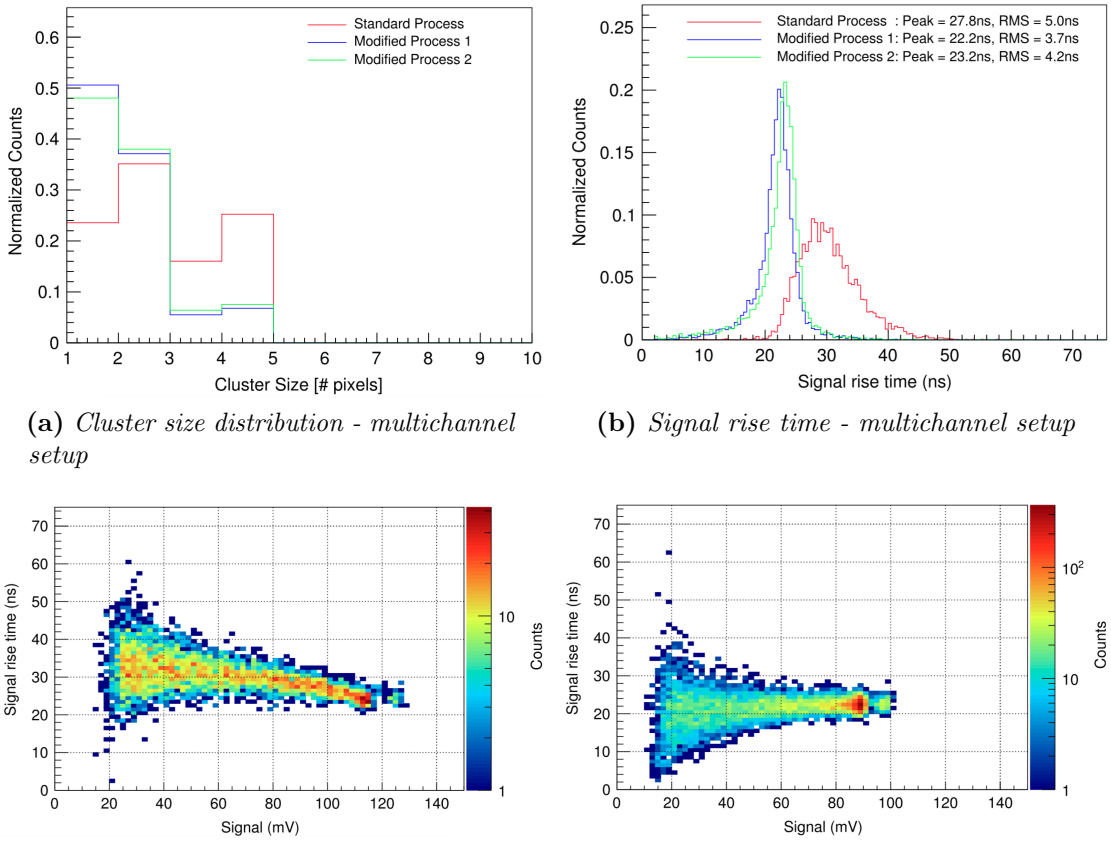


**(a)** *Cluster size distribution - multichannel setup*

**(b)** *Signal rise time - multichannel setup*

**(c)** *Signal vs. Rise time - Standard Process*

**(d)** *Signal vs. Rise time - Modified Process*

**Figure 7.6.** *Cluster size (a) and signal rise time (b) of 28 µm pixels of unirradiated sensors recorded with the multichannel setup. The correlation of single-pixel signal and signal rise time show a shape difference between the Standard Process (c) and the Modified Process (d) [45].*

### Measurements on 30 µm pixel structures

During the time of this thesis, the next test chip was designed based on and in line with the results obtained in the various measurements. The pixel structure M106 – 30 µm pixel size, 3 µm electrode size, 3 µm spacing, maximum deep p-well – got into the focus of measurements for having a pixel size close to the designated pixel size and having a very high pixel gain.

Figure 7.7 shows the signal spectra of $^{55}$Fe and the converted energy spectra of $^{90}$Sr for sensors produced in both processes. As before, a reduction in gain is visible. The energy resolution seems to be unaffected since the peak width reduces in a similar magnitude. The 30 µm pixel structure is affected significantly by charge sharing. For both processes, the shape is distorted, comparable to the simulations presented in the previous chapter. Comparing the shapes confirms lower charge sharing for the Modified Process, leading to a more distinct peak. The obtained MPVs are 1418 e for the Standard Process and 1519 e for the Modified Process. A complete collection of the expected MPV charge of 1575 e is assumed.

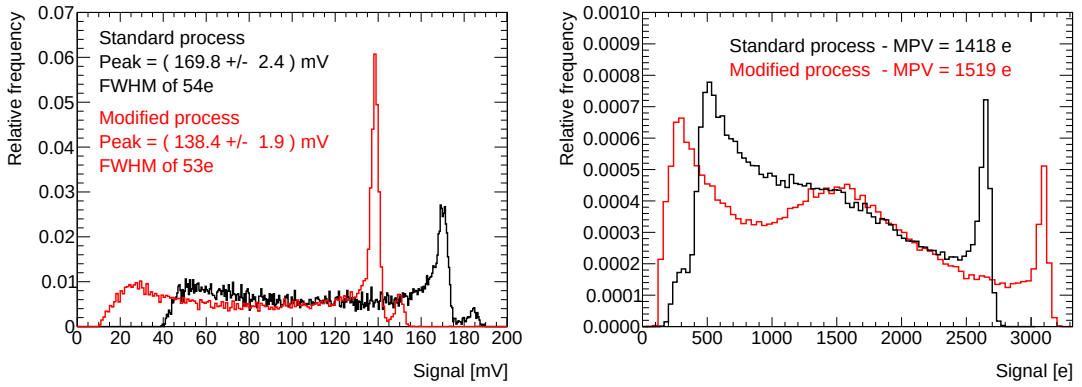


**(a)** *$^{55}$Fe signal spectra* **(b)** *Converted $^{90}$Sr energy spectra*

**Figure 7.7.** *Signal spectra of $^{55}$Fe (a) and converted energy spectra of $^{90}$Sr (b) on 30 µm pixels of unirradiated sensors produced in both processes.*

The distribution of signal rise time is shown in Figure 7.8. Similar to the 28 µm pixels, the mean of the distribution is lower and the width of the peak is smaller for the Modified Process, indicating a more uniform depletion and fast charge collection.

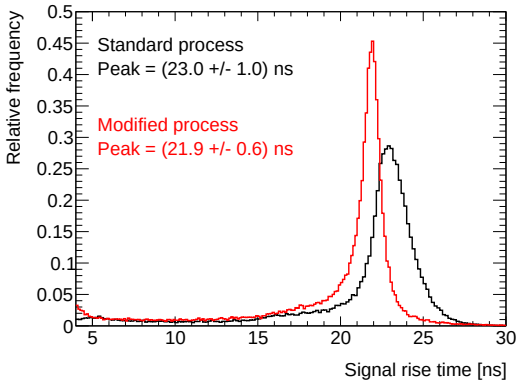


**Figure 7.8.** *Signal rise time of $^{90}$Sr hits on 30 µm pixels of unirradiated sensors produced in both processes.*

### 7.2.1. Signal spectra depending on pixel position

Obtaining full lateral depletion of the pixel cell even after irradiation is the major aim of the process modification. Source scans provide no position information other than the fact that a signal of a certain value was recorded in the pixel. Measurements at the CERN SPS testbeam on the other hand provide reconstructed position information of a passing particle – pions in the presented case – and can be used to detect areas of low depletion. Due to the nature of the interaction, the deposited charge is not monochromatic.

A third measurement technique combining the advantages of position resolution and monochromatic energy deposition uses a highly focused photon beam. Usually, a strong laser pulse is used. In case of the TJInv, a laser can not penetrate the metallised surface and a different photon energy is needed.

For this purpose, testbeam campaigns were planned and performed at the DIAMOND synchrotron facility [4] in Oxfordshire, United Kingdom, in the years 2016 and 2017. The DIAMOND facility provided a monochromatic X-ray beam with an energy of 15 keV which is around three times the energy of $^{55}$Fe and below the X-ray lines of Nb, corresponding to a deposited charge of around 4140 e.
The provided beam was highly focused and had a sigma-width of around $1.3 \times 2.7\,\mu m^2$. The Time-precision setup was installed on a movable $x--y$ table. Using the $x--y$ table, the surface of the pixels could be scanned with high position resolution [39]. One measurement of structure M129 on a sample of the Modified Process is shown in Figure 7.9. For different bias voltages, the number of stored events in 30 s was counted depending on the position of the X-ray beam while scanning over the pixel center. The pixel width of 50 µm is clearly visible for all three bias voltages, (0 V, −3 V and −6 V) indicating full horizontal depletion even when substrate and deep p-wells are connected to ground. In this case, the collection electrode is still on the potential of $V_{\mathrm{RESET}} = 1\,\mathrm{V}$ and the horizontal junction of the Modified Process is biased as expected by simulations [45].

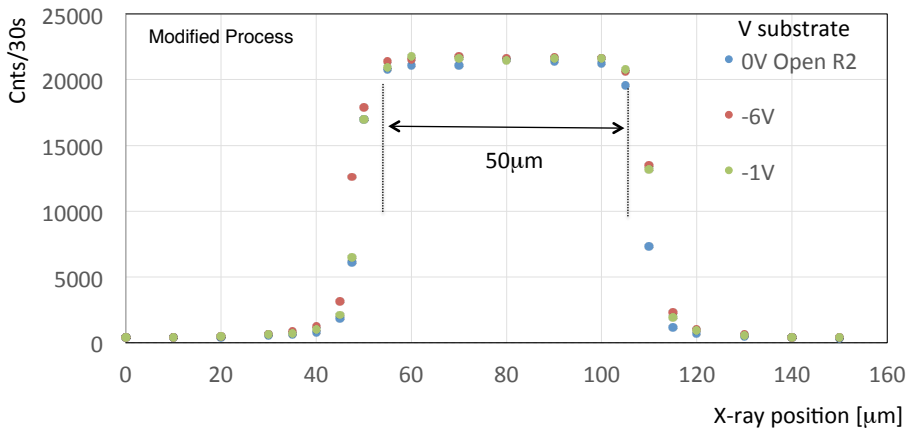


**Figure 7.9.** *A 1d scan over the pixel center of an unirradiated structure M129 is performed for different biasing voltages and the number of stored events per 30 s are counted [39].*

The position information during the scan is used to analyse the obtained signal spectra for different positions. A comparison between a signal spectrum at the edge of the pixel and at its center is shown in Figure 7.10. As expected, the signal spectrum at the pixel center in Figure 7.10a is dominated by one peak corresponding to the energy of 15 keV being completely deposited in this pixel. Only a very small continuum of hits with smaller signal is visible.

[4] DIAMOND Light Source, U.K., http://www.diamond.ac.uk/Home.html

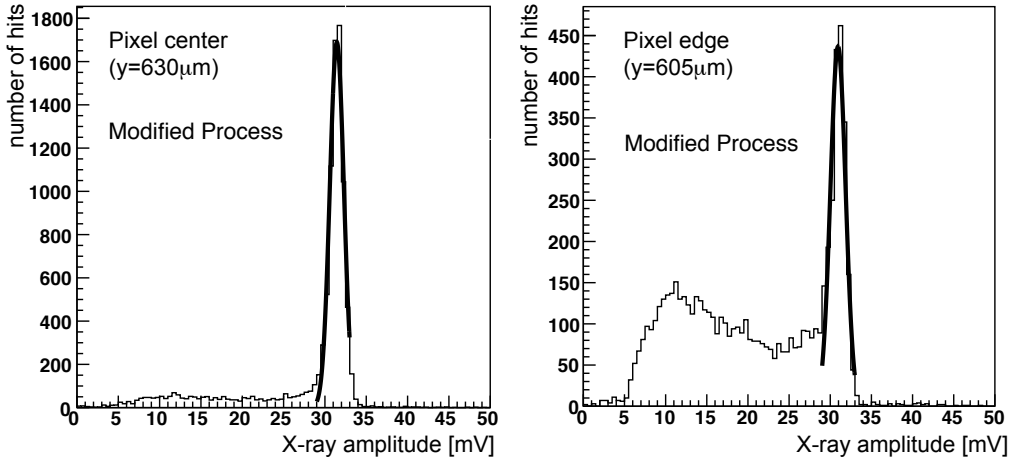


**(a)** *Single-pixel spectrum (pixel center)* **(b)** *Single-pixel spectrum (pixel edge)*

**Figure 7.10.** *Single-pixel spectra of the 15 keV beam at the center (a) and edge (b) of an unirradiated M129 structure. [39]*

The signal spectrum at the pixel edge in Figure 7.10b shows a significantly lower peak – only around 450 hits instead of around 1800 hits as peak maximum – and also a clear continuum of shared hits with the neighbouring pixel. The qualitative shape of the continuum agrees with previously observed spectra of smaller pixels as well as the charge sharing simulations presented in the previous chapter.

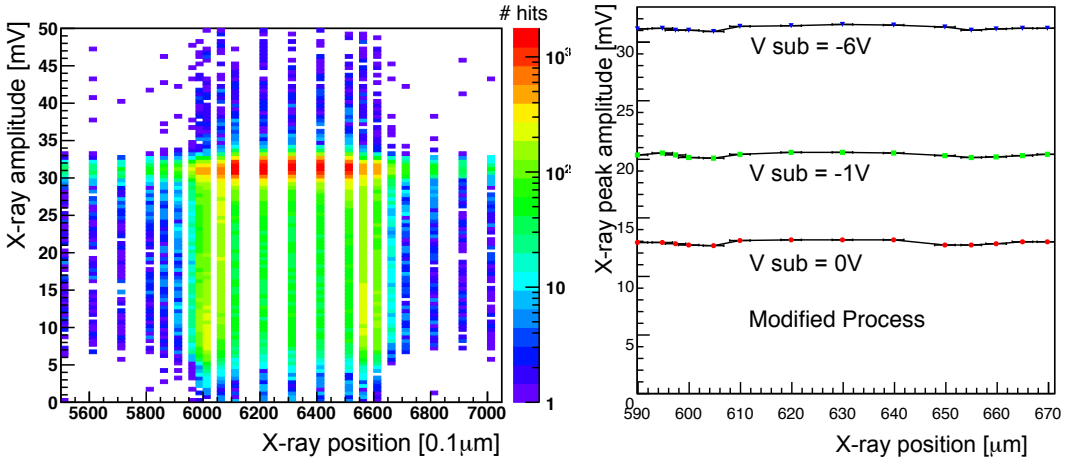


**(a)** *Single-pixel spectra for $HV = -6V$* **(b)** *Peak signal positions*

**Figure 7.11.** *Single-pixel spectra for $HV = -6\,\mathrm{V}$ depending on the position (a) and peak positions for different bias voltages (b) [39].*

An overview of the signal spectra depending on the beam position is given in Figure 7.11a. The 'center' behaviour is observed for most of the pixel area, approximately $\pm 20\,\mu\mathrm{m}$ around the center, the 'edge' behaviour is observed in an area close to the next pixel. Hits are also recorded when the beam position is in the area of a neighbouring pixel. In close proximity, charge is shared with the recorded pixel,

leading to smaller signals. In the case of further distance or when a signal of full energy is recorded, the photons originated from the beam halo [39].

The signal size of the monochromatic peak at each position is determined as before. The results for the different bias voltages is shown in Figure 7.11b. The peak position increases with higher reverse biasing voltage as expected and observed in previous measurements. Within each data set, the value varies less than 3 %, confirming full depletion already for HV= 0 V. This high level of uniformity in gain over the pixel results in only a small contributions to the resolution uncertainty of the obtained spectra. Furthermore, no charge loss and only a small dip around the edges of the pixel due to charge sharing with the neighbouring pixel is visible [39].

## 7.3. Sensor performance after irradiation

Before irradiation, both standard and Modified Process show clear and fast signals. The Modified Process shows less charge sharing and a more uniform signal rise time. At the same time, the increase in capacitance leads to a gain reduction of the pixel. For applications with low-radiation environment, the Standard Process can be the better choice. Whereas the results of the Standard Process in the CERN SPS testbeam failed to fulfil the requirements of the ATLAS ITk.

In order to test the expected improvement, sensors produced in the Modified Process were the main focus of the CERN SPS testbeam campaign 2016. Being the same campaign, setup, readout, and cooling were the same as described in the last chapter. The irradiation of sensors of the Modified Process were done in Ljubljana, equivalent to the irradiations of the Standard Process. During an earlier campaign, sensors of a higher doping concentration in the n-type implant – called 'Modified Process 1' before – were irradiated up to $1.0\times10^{15}\,\mathrm{n/cm^2}$. During a second campaign, sensors of a lower doping concentration – called 'Modified Process 2' before – were irradiated up to $1.0\times10^{16}\,\mathrm{n/cm^2}$.

### 7.3.1. Gain and charge collection after irradiation

Irradiated sensors of the Modified Process were tested in the same fashion as the ones of the Standard Process before. Unfortunately, no sensor of the Modified Process irradiated to $10^{15}\,\mathrm{n/cm^2}$ was included in the Glasgow X-ray fluorescence campaign. Similar to the Standard Process, a linear conversion is used between obtained signal spectra and energy spectra.

#### Measurements on 50 µm pixel structures

The first analysed structure was M129, measured at HV = −6 V. Single-pixel spectra for $^{55}$Fe and $^{90}$Sr before and after irradiation are given in Figure 7.12. The peak of $^{55}$Fe is clearly visible also after irradiation as well as a small component of shared hits.

Comparing the spectra of the unirradiated sample in black and of the one irradiated to $10^{15}$ n/cm$^2$ in red, a gain reduction of almost 20 % after irradiation is visible in Figure 7.12a. A reduction in gain was also observed for the Standard Process after $10^{14}$ n/cm$^2$ indicating an increase in capacitance. Assuming as before that both peaks correspond to a deposited charge of 1650 e, the FWHM of the peak increases from around 192 e to 307 e after irradiation, corresponding to an energy resolution rise from 5 % to 8 %.
The gain reduction observed in the spectrum of $^{55}$Fe is also present in the spectrum of $^{90}$Sr shown in Figure 7.12b. Both spectra, again unirradiated in black and irradiated in red, show the expected landau distribution.

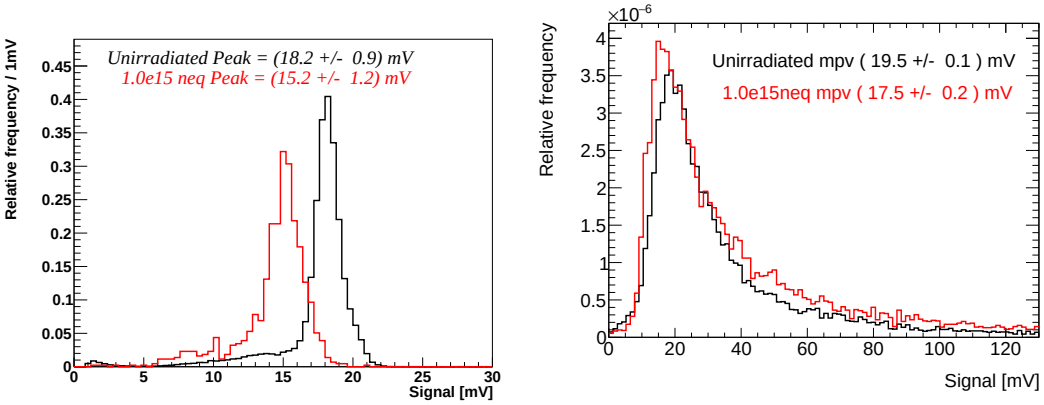


**(a)** *Single-pixel $^{55}$Fe spectrum [51]* **(b)** *Single-pixel $^{90}$Sr spectrum*

**Figure 7.12.** *Single-pixel signal spectra obtained for the source measurements using (a) $^{55}$Fe and (b) $^{90}$Sr sources: For both the unirradiated sample in black and the sample irradiated to 1.0×10$^{15}$ n/cm$^2$ in red, a clear $k_\alpha$ peak is visible in the $^{55}$Fe single-pixel signal spectrum (a). In the $^{90}$Sr signal spectrum (b), both distributions show the expected shape [51].*

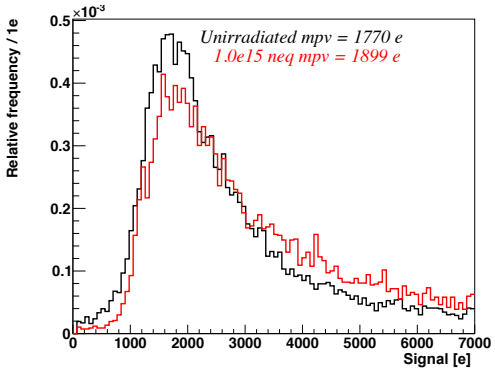


**Figure 7.13.** *Converted $^{90}$Sr energy spectra after 1.0×10$^{15}$ n/cm$^2$: The MPVs in the converted $^{90}$Sr spectra before irradiation in black and after 1.0×10$^{15}$ n/cm$^2$ in red agree well [51].*

As before, the conversion from signal spectra into energy spectra is performed using the $^{55}$Fe peak positions to investigate charge collection and potential charge loss. The converted $^{90}$Sr energy spectra are shown in Figure 7.13.

The obtained MPVs are 1770 e before and 1899 e after irradiation. With respect to the energy resolutions given by the $^{55}$Fe peaks – 5 % before and 8 % after irradiation – and by the limited statistics of the measurements, these values agree and the sensors shows no charge loss due to radiation damage.
No X-ray fluorescence measurement was performed on the irradiated sensor of the Modified Process but since the MPV signal is very close to the $^{55}$Fe peak signal, the evaluation of the MPV is within reason.

Concerning the extrapolation to the entire energy spectrum, a shape difference is visible: After irradiation, the distribution seem to be tilted, leading to a higher tail. Matrix M129 being a LG structure, this can be the effect of different saturations in the transfer function.

### Measurements on 30 µm pixel structures

The measurement was repeated for the 30 µm pixel structures M106. As mentioned, M106 is a HG structure with a significantly lower pixel capacitance. The obtained $^{55}$Fe single-pixel signal spectra are shown in Figure 7.14a.

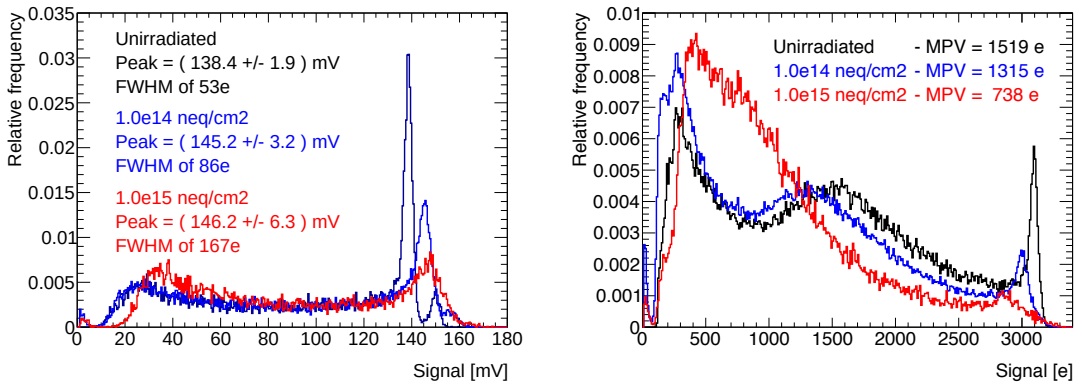


**(a)** *Single-pixel $^{55}$Fe spectrum [51]* **(b)** *Single-pixel $^{90}$Sr spectrum*

**Figure 7.14.** *Single-pixel signal spectra of $^{55}$Fe (a) and converted energy spectra for $^{90}$Sr (b). The shape of the distributions indicate an increase of charge sharing for higher fluences [51].*

Like for structure M129, the resolution in the $k_\alpha$ peak worsens with irradiation from a **F**ull **W**idth **H**alf **M**aximum (FWHM) of 53 e (unirradiated) to 86 e ($10^{14}$ n/cm$^2$) to even 167 e ($10^{15}$ n/cm$^2$).
Unlike structure M129, the gain seems to increase with irradiation damage. The increase is around 6 % after $10^{15}$ n/cm$^2$ and rather small compared to the 20 % of gain reduction for structure M129. The increase can have different reasons: On one hand, it is possible that the transfer function changes with irradiation differently for LG and HG structures. In such a case the observed discrepancies are caused by fixing the working point at $V_{\mathrm{RESET}} = 1$ V. On the other other hand, the pixel capacitance is the significant factor of the signal size. Both results combined indicate a capacitance increase for M129 and a decrease for M106.

The total capacitance of the pixel cell is determined by contributions, firstly between collection electrode and surrounding p-wells, secondly between deep p-wells and n-layer and thirdly between n-layer and p-substrate. The geometric differences between M129 and M106 could lead to different contributions being dominant for the total capacitance. Measurements on a higher selection of structures as well as simulations are needed to study this effect further.

The converted energy spectra of the $^{90}$Sr measurements are shown in Figure 7.14b. The comparison with irradiated samples of the Modified Process presented here show a visible increase of charge sharing with irradiation. Due to this, the peak position decreases from 1519 e (unirradiated) to 1315 e ($10^{14}$ n/cm$^2$) and to 738 e ($10^{15}$ n/cm$^2$). Again, the decrease together with the change of shape indicates stronger charge sharing but is no indication for charge loss in the pixel volume. A very rough estimation possible with the single-pixel spectra is based on the charge sharing simulations presented in the previous chapter. For a constant smearing, all energy spectra cross around 0.7 MPV. The spectra in Figure 7.14b cross around 1300 e, leading to an estimated cluster MPV of around 1857 e which is the in order of magnitude of previous measurements for M129.

## 7.3.2. Signal rise time after irradiation

Before irradiation, samples of the Modified Process show a more uniform and more narrow timing distribution than the Standard Process. In the case of the Standard Process, radiation damage and failing depletion were visible in complete distortion of the timing distributions. Any improvement in radiation hardness must be observable in a more uniform timing distribution even after this level of irradiation.

### Measurements on 50 µm pixel structures

The signal rise time distributions for structure M129 are shown in Figure 7.15. Having again unirradiated in black and irradiated in red, the comparison shows an increase in the signal rise time of around 15.5 % from (16.0 ± 3.2) ns to (18.5 ± 4.1) ns. With this increase the mean of the distribution still stays below one bunch crossing time of 25 ns. For the Standard Process, a decrease of the mean signal rise time was observed due to depletion problems. The increase observed in the Modified Process might be related to the increase of the pixel capacitance. The width of the timing distribution increases by around 32 % but still stays below 5 ns.

Correlations of the timing distributions and the $^{90}$Sr energy spectra are shown before irradiation in Figure 7.16a and after irradiation in Figure 7.16b. Unlike for the Standard Process, the triangular shape is preserved after $10^{15}$ n/cm$^2$. The increase in spread is visible but the signal distribution is well-defined and contained. The observed width increase in the timing distribution after irradiation affects hits of all amplitudes and not only a specific amplitude range, indicating not an effect at the edges of a depletion volume but in the entire pixel, such as a global increase of capacitance.

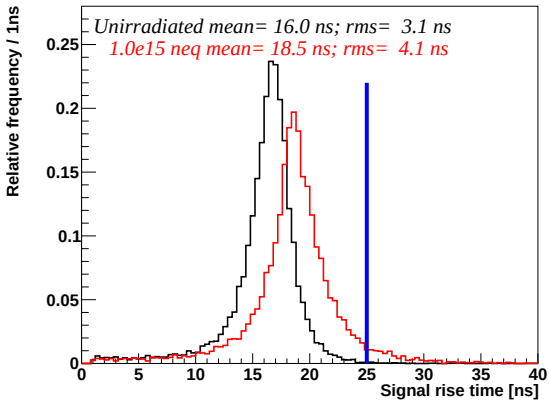


**Figure 7.15.** *The $^{90}Sr$ signal rise timing distributions before irradiation in black and after irradiation in red [51].*

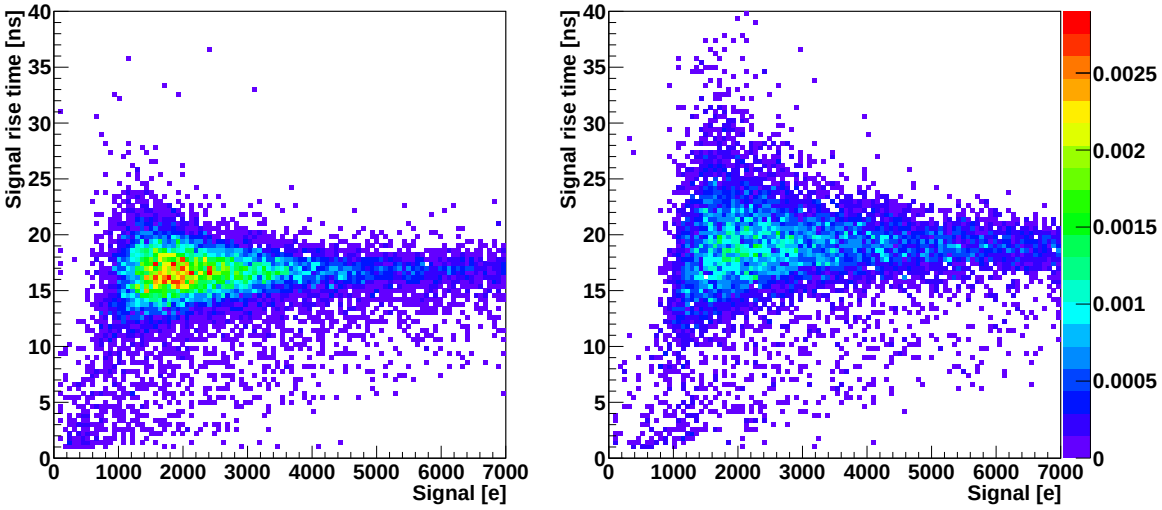


**(a)** *2d - unirradiated* **(b)** *2d - $10^{15}$ n/cm$^2$*

**Figure 7.16.** *Signal rise time plotted against the signal size of the $^{90}Sr$ spectra for the unirradiated sensor (a) and the sensor after 1.0×$10^{15}$ n/cm$^2$ (b) [51].*

### Measurements on 30 µm pixel structures

The distributions of signal rise time obtained for structure M106 are given in Figure 7.17a. As seen for M129, the width of the distribution increases with irradiation but unlike M129, the peak positions decrease. A reduction from (21.9 ± 0.6) ns (unirradiated) to (17.9 ± 0.8) ns ($10^{14}$ n/cm$^2$) to (14.3 ± 1.2) ns ($10^{15}$ n/cm$^2$) is observed. The behaviour contrary to M129 might be a second indication that the different pixel geometries led to different capacitance changes when exposed to neutron radiation.

The correlation between energy spectrum and rise time distribution for the unirradiated sensor is given in Figure 7.17b. The distribution is very narrow with a saturation peak around 3000 e and 21 ns.

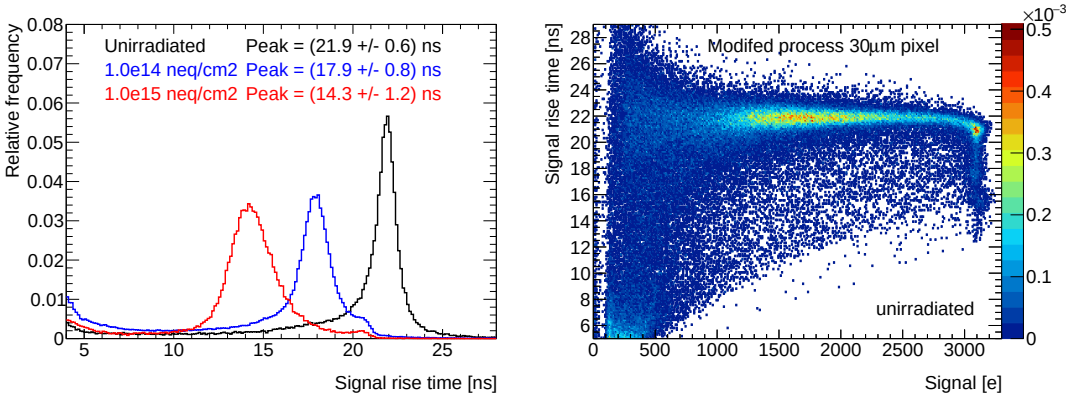


**(a)** *Rise time distributions M106* **(b)** *2d - unirradiated*

**Figure 7.17.** *$^{90}$Sr timing distributions before and after irradiation. The peak positions decrease with increasing radiation damage (a). The 2d correlation of the unirradiated sample shows the narrow peak and the continuum of the shared hits (b) as well as the saturation peak of the pixel cell on the right-hand side.*

There is also a triangular continuum of hits with lower signals and lower times visible as low contribution. The corresponding correlation plots for the irradiated samples are shown in Figure 7.18. The position of the saturation peak stays fairly constant whereas the shape of the distribution shows an increasing curvature. The distribution seems to move both towards lower signal rise times and lower signals. Regarding the observed increase of charge sharing, the movement indicates that shared hits tend to have a smaller signal rise time but previous measurements with $^{55}$Fe showed no similar indication for photons.
As mentioned, the presented single-pixel measurements are limited in distinguishing charge sharing and charge loss and furthermore provide no position information of the charge deposition. Position-sensitive multi-channel measurements are needed to investigate the observation further.

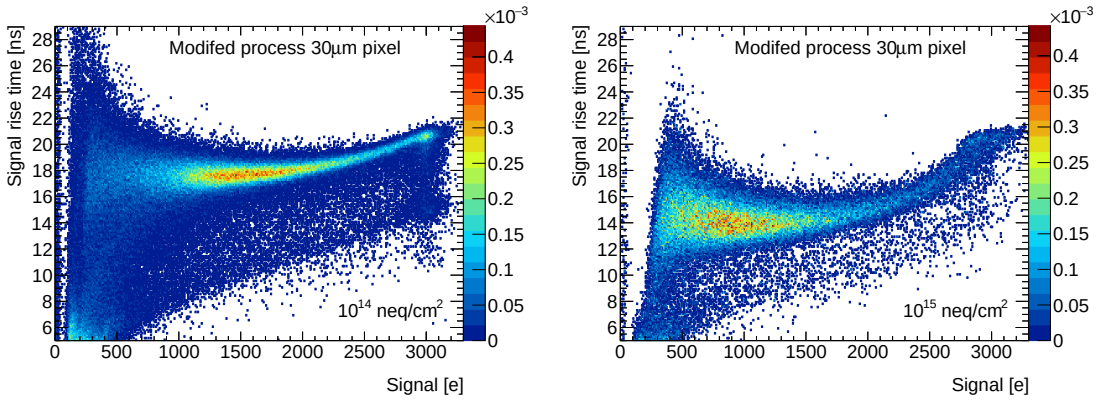


**(a)** *2d - $10^{14}$ n/cm$^2$* **(b)** *2d - $10^{15}$ n/cm$^2$*

**Figure 7.18.** *The 2d correlation of the sample irradiated to $1.0\times10^{14}$ n/cm$^2$ (a) and $1.0\times10^{15}$ n/cm$^2$ (b) for M106.*

### 7.3.3. Hit rates depending on pixel position

During the 2016 testbeam campaign at the DIAMOND synchrotron facility, only unirradiated sensors were measured due to the lack of cooling. During the 2017 campaign, cooling was realised with dry ice and the cooling box of the CERN SPS testbeam. An additional improvement was the parallel readout of multiple pixels to investigate charge sharing into neighbouring pixels while scanning over the surface. The scans were performed as explained earlier in section 7.2.1, recording hits for 30 s at each given position. Due to limitations of the available DRS4 firmware, no logical OR-combination of pixels could be used. Instead, the output of one specific pixel was used for triggering. This results in a significant drop of statistics outside of the trigger-pixel as expected by the effective pixel-widths recorded in 2016.

#### Charge sharing after $10^{15}$ n/cm$^2$ on 30 µm structure M106

As before, the structure in focus was the HG 30 µm structure M106. While scanning over the pixel selected for triggering, the waveforms in the neighbouring ones were also recorded. The 1d scan is shown in Figure 7.19.

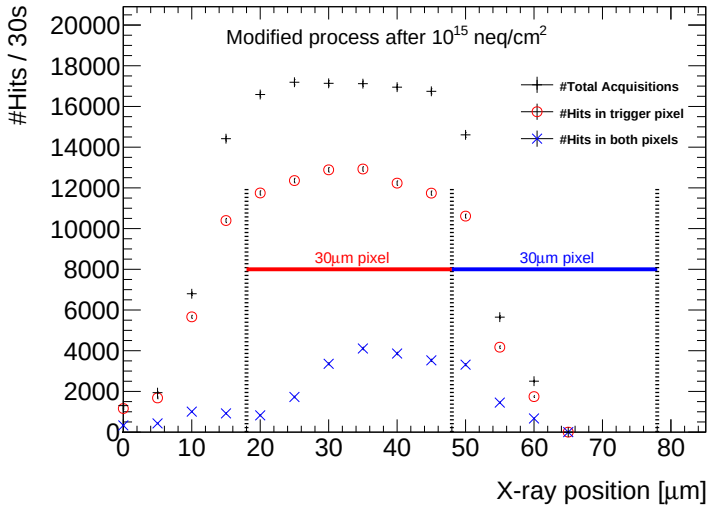


**Figure 7.19.** *1d scan over structure M106 after irradiation. The number of stored hits per 30 s are given in black, the number of hits in the trigger pixel in red and the number of common hits in both trigger and adjacent pixel in blue.*

The black data points represent the total number of stored hits per 30 s. As for the unirradiated sensor before, the effective pixel width of the trigger pixel is clearly visible as indicated. The red data points represent the number of valid hits in the trigger pixel, confirming the effective pixel width. The difference between the black and red points is caused by the high rate of the synchrotron beam and the time window of the reset-veto. If particles hit the pixel during the veto, the charge is collected and the trigger condition can become valid at the end of the veto. In this case the recorded interval does not contain a valid hit.

The blue data points represent the number of events with valid hits in both the trigger pixel and the adjacent pixel indicated by the blue line. Such events can be observed over the entire length of the trigger pixel. The decrease inside the adjacent pixel is caused by the decrease of recorded hits in the trigger pixel.

Given the fix triggering on one pixel, a suitable measure for the shared hits is a two-pixel cluster size, demanding one hit in the trigger pixel. It can be deducted from the presented data sets as $(1 + \frac{\#\text{Hits in both pixels}}{\#\text{Hits in trigger pixel}})$. The values per position are given in Figure 7.20, the center of the trigger pixel is indicated in green.

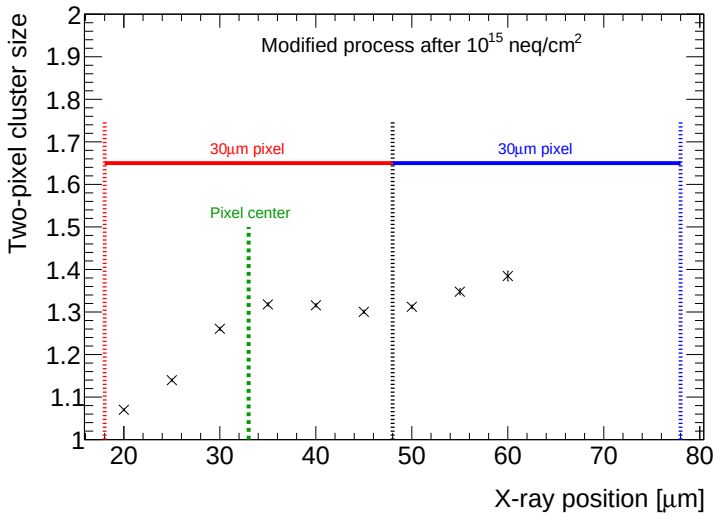


**Figure 7.20.** *Two-pixel cluster size for all events with a valid hit in the trigger pixel. The center of the trigger pixel is indicated in green.*

Scanning from left to right, the two-pixel cluster size rises until reaching a value of around 1.3 at the center of the trigger pixel. This means that around 30 % of the hits in the center also have a hit in one specific adjacent pixel. Towards the adjacent pixel, the value of around 1.3 stays relatively constant. Inside the adjacent pixel, it starts to rise again which is caused the triggering on the left pixel. Due to symmetry reasons, it is reasonable to assume the same trend as in the trigger pixel. Since the two-pixel cluster size does not drop to 1 left of the green line, an even higher multi-pixel cluster size for structure M106 after irradiation is to expect. In addition, the 1d scan was performed over the center of a pixel, not covering a pixel corner. A strong level of charge sharing agrees with the low MPV of 738 e in the $^{90}$Sr spectra after $10^{15}$ n/cm$^2$.

## 7.4. Efficiency measurements – Modified Process

The performance of unirradiated sensors showed a reduction of gain compared to the Standard Process and the measurements with position-resolved synchrotron radiation indicated depletion over the sensor area already for $HV = 0\,\mathrm{V}$.
Sensors of the Modified Process were the main focus of the CERN SPS testbeam campaign 2016. Charge map and cluster-size map of structure M129 for an unirradiated sensor are shown in Figure 7.21. The charge map shows the average cluster charge – calculated as the sum of all four pixels – as function of position. The obtained charge map shows a fairly homogenous charge collection as expected for the unirradiated sensor.
The cluster-size map shows the number of pixels above threshold. For the 50 µm pixels of M129, only small charge sharing was observed in the laboratory measurements. In the testbeam, charge sharing is only located at the pixel edges as expected [39].

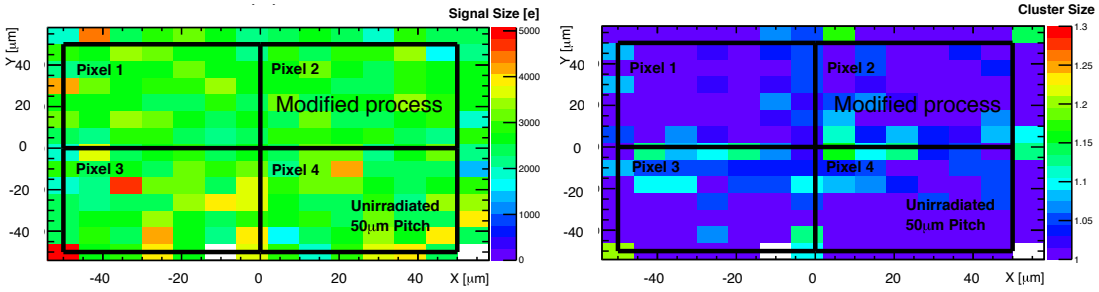


**(a)** *Charge map* **(b)** *Cluster-size map*

**Figure 7.21.** *Charge map (a) and cluster size map (b) of an unirradiated sensor of the Modified Process [39].*

The noise level during testbeam measurements was higher than during laboratory measurements, caused by the testbeam environment. Gaussian noise contributes the majority of this noise, the reception of harmonic noise induced by other devices was reduced as much as possible. Figure 7.22 shows the distributions of signal and noise. They are well separated for the LG structure. The signal MPV coincides with previous expectations and the S/N of MPV and noise is around 13:1 [39].

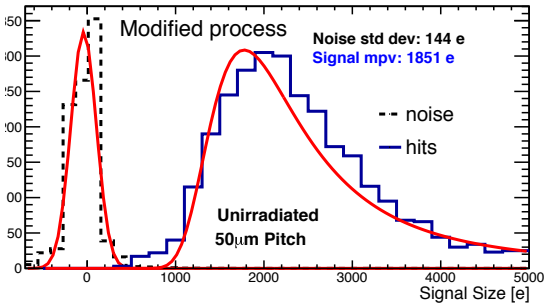


**Figure 7.22.** *Distributions of signal in blue and noise in black as measured in the CERN SPS testbeam for structure M129 [39].*

The high capacitance of the LG structure results in small signals and therefore a relatively small S/N. As mentioned before, structure M129 has a pixel size of 50 µm in combination with a relatively small collection electrode of 3 µm and a relatively large spacing of 40 µm. The structure was selected to test the depletion capabilities of the Modified Process in a significant distance from the collection electrode. The efficiency projections in both directions are given in Figure 7.23. Compared to the testbeam measurements of the Standard Process, a higher statistic was collected in these measurements. The overall efficiency is measured to be 98.5 % ± 0.5 % (stat.) ± 0.5 % (syst.). The efficiency is limited due to the noise present in the setup. As consequence, a higher threshold was chosen to cope with the noise. It is to expect that a chip which includes digital signal processing in a front-end suffers from less noise compared to the TJInv since no analogue waveforms are transported over several centimetres of cable.

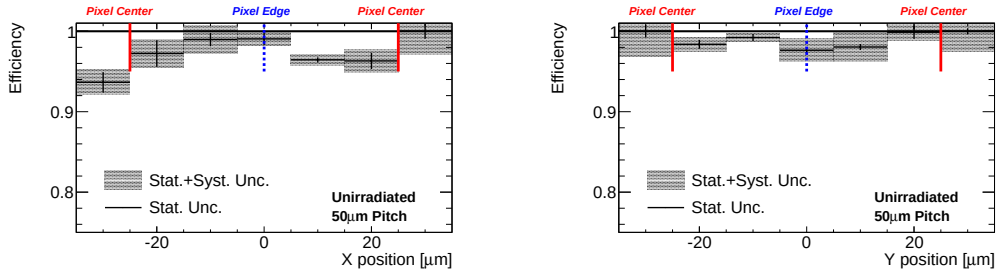


**(a)** *Efficiency projections in x (corrected)* **(b)** *Efficiency projections in y (corrected)*

**Figure 7.23.** *Efficiency projections in x-direction (a) and y-direction (b) after correction [39].*

### 7.4.1. Testbeam results of the Modified Process after irradiation

The 2016 CERN SPS testbeam campaign included irradiated sensors of the Modified Process. The results for M129 after $1.0\times10^{15}$ n/cm$^2$ are shown in Figure 7.24.
The corrected efficiency map shows values above 70 % for the central area. An efficiency drop in the middle of the active area (pixel edges) is visible in both the map and the projections. At the position of the collection electrodes, the measured efficiency is around 90 %. The overall efficiency over the central area is measured to be 87.9 % ± 1.4 % (stat.) ± 0.6 % (syst.) .
The improvement in performance of the Modified Process was already seen in laboratory measurements. The efficiency projections show the significant improvement in a more uniform depletion. The efficiency does not drop down to 40 %, even at the pixel edges far away from the collection electrodes. Instead, the efficiency is more constant over the pixel area and still around 90 % at the collection electrodes. Structure M129 of the Modified Process performs significantly better than the corresponding one of the Standard Process after irradiation but does not fulfil the minimum hit efficiency requirement of 97 % [29].

As mentioned before, this structure was selected at the very beginning of the project to test the TowerJazz technology and the designs implemented in the TJInv under difficult conditions. Regarding the obtained results, further structures on this chip were measured to study if the Modified Process is capable of fulfilling the requirements.

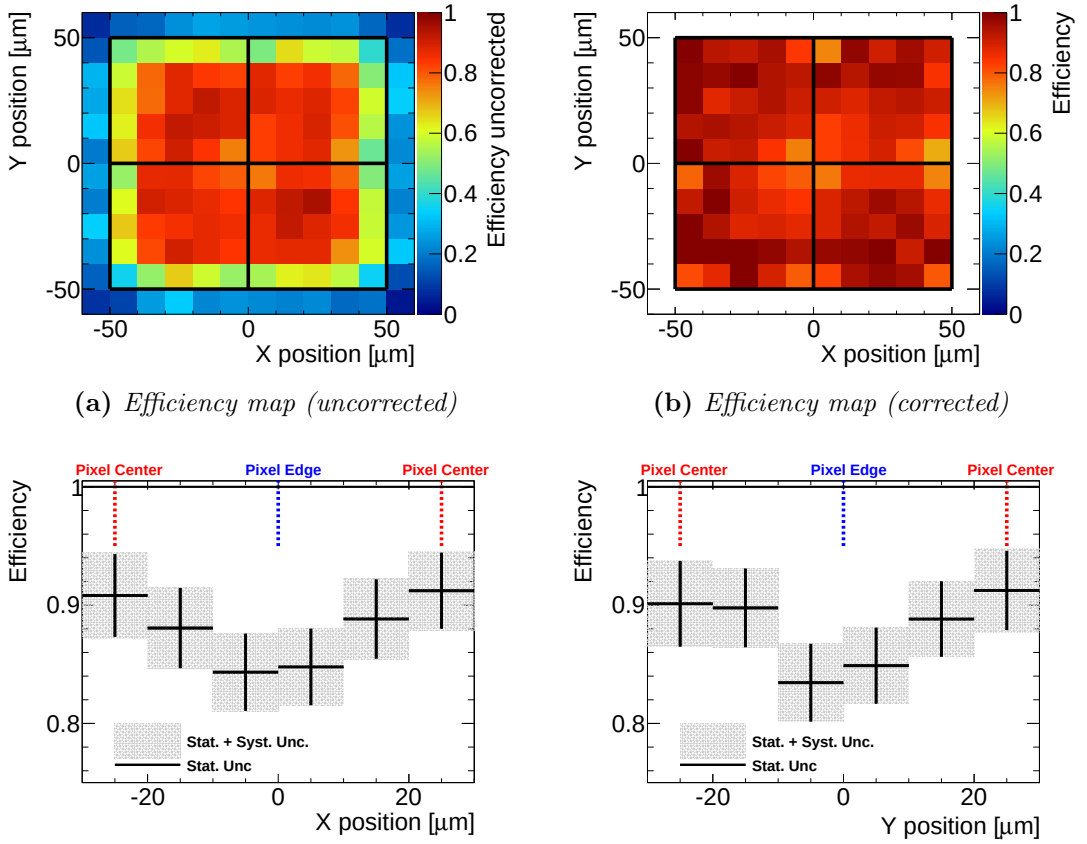


**(a)** *Efficiency map (uncorrected)*

**(b)** *Efficiency map (corrected)*

**(c)** *Efficiency projections in x (corrected)*

**(d)** *Efficiency projections in y (corrected)*

**Figure 7.24.** *Efficiency map over the entire four-pixel area before (a) and after applying the resolution correction (b) as well as efficiency projections of the central area in x-direction (b) and y-direction (c) for Modified Process 50 µm pixel after 1.0×10$^{15}$ n/cm$^2$.*

### Measurements on 25 µm pixel structures

As contrast to the big pixel structure M129 with a big pixel spacing, one other tested structure was M060. This structure has a pixel size of only 25 µm and a spacing of only 3 µm. The electrodes of both structures are 3 µm in size. The obtained corrected efficiency map and the projections are shown in picture 7.25.
The overall efficiency was measured to be 98.5 % ± 1.5 % (stat.) ± 1.2 % (syst) for this structure. The fluctuations in the efficiency map are within the resolution of the telescope. As for all measurements presented here, the statistics were limited due to the small dimensions of the analysed structures, in this case only 50 µm×50 µm total sensor four-pixel area and 25 µm×25 µm as center area. Regarding the uncertainties, full efficiency is observed over the central area.

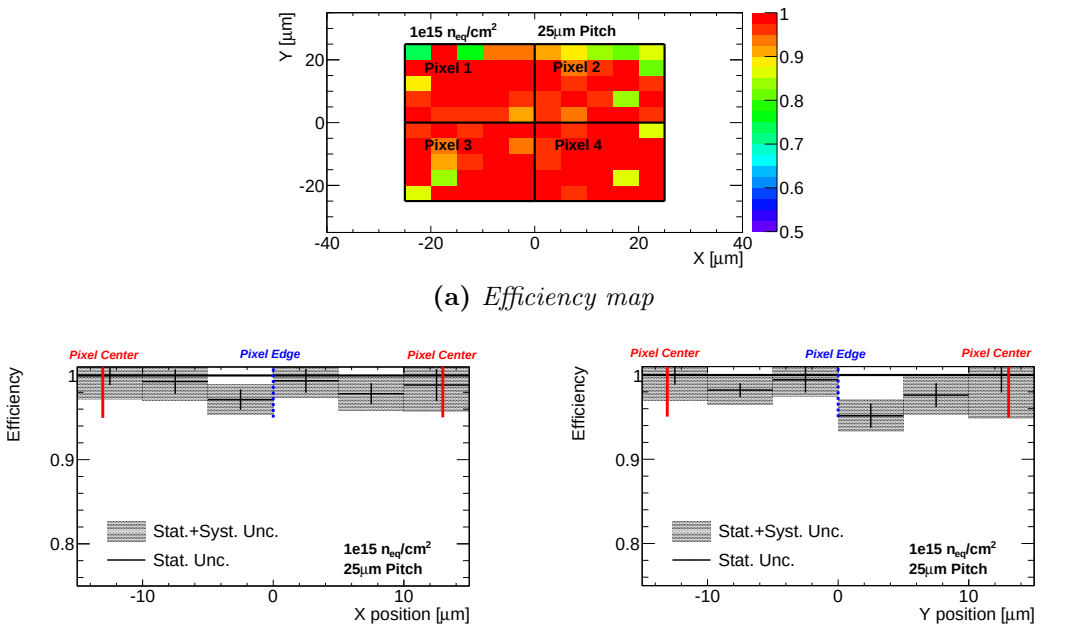


**(a)** *Efficiency map*

**(b)** *Efficiency projections in x (corrected)*

**(c)** *Efficiency projections in y (corrected)*

**Figure 7.25.** *Efficiency map over the entire four-pixel area (a) as well as efficiency projections of the central area in x-direction (b) and y-direction (c) for Modified Process 25 µm pixel after 1.0×10¹⁵ n/cm² [39].*

Compared to structure M129, the 25 µm pixel structure is a HG structure and therefore its performance is less affected by the higher noise level present in the testbeam environment. This was visible as larger S/N of around 39:1 [39]. Another difference between the structures is the strength of the electric field within the pixel. The reverse bias voltage of $HV = -6\,\mathrm{V}$ is applied to the deep p-wells and the substrate below the epitaxial layer. In a bigger structure – especially with a bigger spacing – a weaker field is created. After such a level of radiation damage, a weaker field in combination with a higher drift distance leads to an increased risk of charge trapping and charge loss.

### Measurements on 30 µm pixel structures

Structure M106 with 30 µm pixel size, 3 µm electrode size and 3 µm spacing differs from the previous M060 only in a bigger distance underneath the deep p-well. The obtained results are shown in Figure 7.26. The overall efficiency was measured as 97.4 % ± 1.5 % (stat.) ± 0.6 % (syst.). Within the uncertainties, the results for both M106 and M060 agree and show no significant loss of efficiency. Compared to the results obtained for the Standard Process, this proves a highly promising improvement by the planar junction below the additional n-type implant leading to a more homogenous performance.

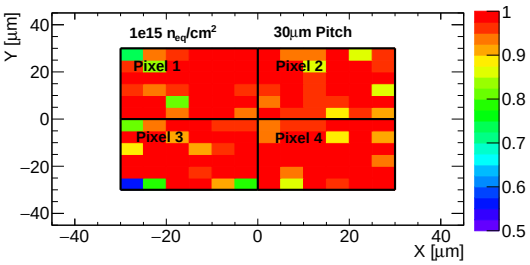


**(a)** *Efficiency map*

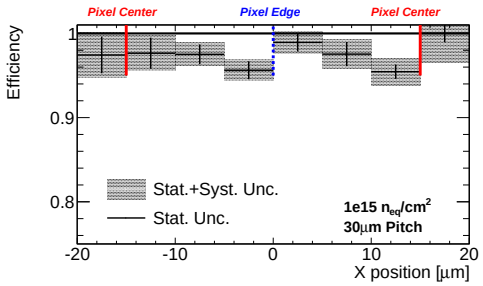


**(b)** *Efficiency projections in x (corrected)*

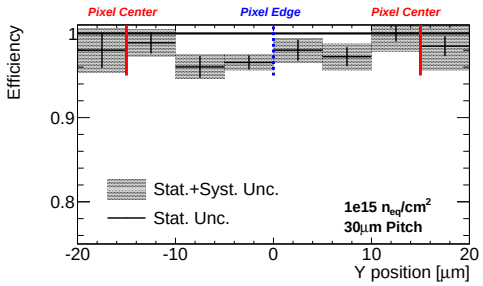


**(c)** *Efficiency projections in y (corrected)*

**Figure 7.26.** *Efficiency map over the entire four-pixel area (a) as well as efficiency projections of the central area in x-direction (b) and y-direction (c) for Modified Process 30 µm pixel after 1.0×10¹⁵ n/cm² [39].*

The next generation of the TJInv is designed to contain separate reverse biasing of deep p-well and substrate, expecting a further improvement in performance. By using separate reverse biasing of, for example, $HV_{DPW} = -6\,\mathrm{V}$ and $HV_{Subs} = -20\,\mathrm{V}$, the field in the pixel can be increased for enhancing charge collection in the epitaxial volume. This approach uses the benefit of increasing the bias voltage to increase radiation hardness while the CMOS circuitry is still protected.
Also a new test chip containing digital circuitry was produced in the Modified Process and will be tested in the laboratory and in the SPS testbeam starting in 2018. As mentioned, no analogue information will be transported over cables for this chip. Due to a significantly higher number of pixels, higher statistics can be collected without the systematic uncertainties of the resolution correction.

## 7.5. Charge collection

The testbeam results presented in the last section focused on hit-detection efficiency. Hit detection is given if at least one pixel at the location of the particle hit collects a charge signal above threshold. The presence of noise sets lower limits on possible threshold values while charge sharing at pixel boundaries leads to smaller signals per pixel. Charge loss in the pixel volume affects the hit-detection efficiency when the induced signal is below the set threshold.

For the presented measurement on the 30 µm pixel structure after irradiation to $1.0\times10^{15}$ n/cm$^2$, the map of collected charge in the four pixels is shown in Figure 7.27. The expected total charge of 1575 e is not reached over the active four-pixel area. The collected charge only goes up to around 1100 e at the position of the collection electrodes. At the center of the area the collected charge drops down to around 700 e - 800 e. In case of high noise, low amounts of charge collected per pixel MPV could be undetected.

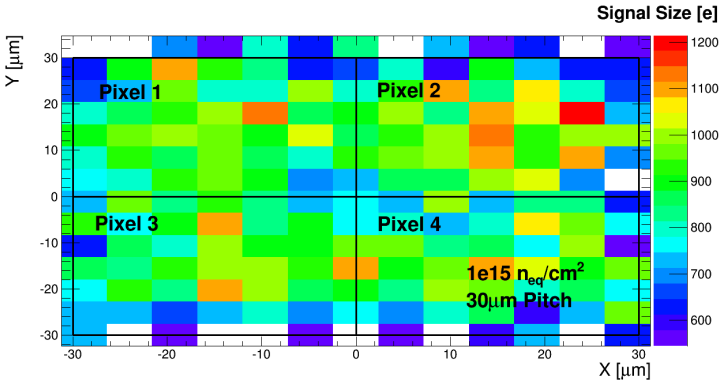


**Figure 7.27.** *Charge map over four-pixel area after irradiation.*

Compared to the $^{90}$Sr single-pixel energy spectra, the determination of total charge deposition in a testbeam measurement includes additional uncertainties. The first was mentioned earlier in the context of cluster measurements. The uncertainty of the energy resolution adds up when adding up charge contributions in several pixels, causing an additional smearing. Two additional uncertainties are caused by temperature and by linear conversion between signal and charge for multiple small signals.

### Temperature dependence of gain

Laboratory source scans were performed in a climate chamber set to −30 °C. The real temperature of the chip might be slightly higher due to the power consumption of the chip but the temperature reaches a stable value within ±1 °C.
The dry-ice cooling used during testbeam is less stable and can lead to temperature differences of around ±10 °C. The temperature dependence of the gain was tested in the climate chamber by recording $^{55}$Fe signal spectra at different temperatures. The measurement was performed with an unirradiated sensor so that a wide temperature range could be covered. The obtained signal spectra are shown in Figure 7.28. A linear correlation between the temperature and the peak position of the $^{55}$Fe spectrum is observed over the investigated range from −35 °C to −20 °C. The estimated slope in Figure 7.28b is (−1.3±0.7) mV/°C.
The size of the band gap is temperature dependent but decreases with increasing temperature which leads to the opposite effect. This dependence can be described by Varshni's equation [59] and its strength is added to Figure 7.28b, scaled to the size of −25 °C. The temperature dependence of the band gap is negligible. The behaviour is probably caused by a component in the internal amplifier chain.

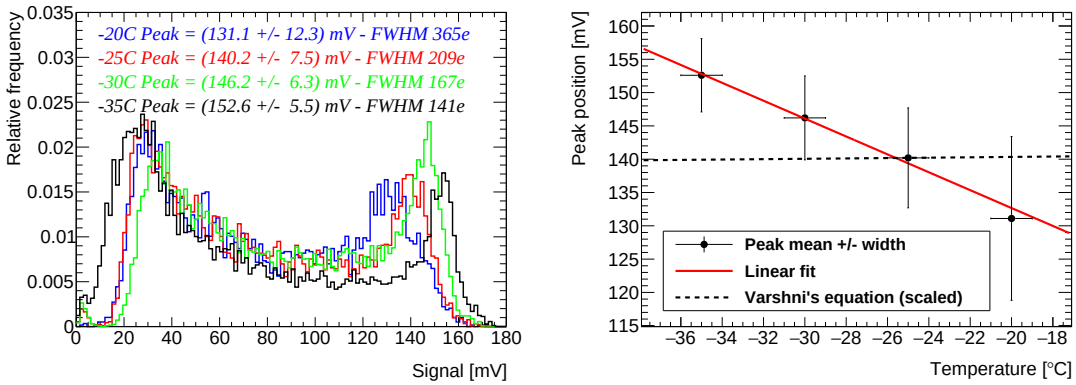


**(a)** $^{55}$*Fe spectra for M106 at different climate chamber temperatures [46]*

**(b)** *Temperature behaviour of peak positions*

**Figure 7.28.** *The effect of the ambient temperature on the $^{55}$Fe spectrum after $1.0\times10^{15}$ n/cm$^2$ has been tested (a). A linear correlation between temperature and gain (peak position) is visible (b).*

Assuming a temperature of $(-25\pm10)\,^{\circ}$C during the measurements, an additional uncertainty of around 11 % on the signal size has to be taken into account. Over the time of a data-taking run, this uncertainty leads to an additional smearing of the charge and – changing the gain of the pixel – affects large charge depositions stronger than small ones.

#### Underestimation of deposited charge - Energy calibration of HG structures

Another uncertainty on the total collected charge is based on the calibration from signal size to deposited charge. As described earlier, a linear correlation is assumed. Since the expected MPV for the analysed samples is very close to the $^{55}$Fe peak, the assumption is used successfully to investigate changes of the MPV qualitatively.
For the estimation of a total-charge map, multiple smaller signals are converted and added up. In the case of a LG structure, linearity is given over the energy range but in the case of a HG structure, saturation is visible at higher energies. The linear assumption can lead to an underestimation of low signals and to an overestimation of large signals.
This uncertainty can not be investigated or compensated in the context of this thesis. More precise X-ray measurements with low-energy lines are needed to determine the conversion function.

### 7.5.1. Influence of the deep p-well size

Despite the present uncertainties, a charge deficit was observed for irradiated sensors over the entire area and especially at the edges. One parameter not yet tested – the horizontal dimension of the deep p-well – and its potential influence in the collected charge was tested.

The deep p-well is needed to shield n-wells and p-type epitaxial layer to not create parasitic collection electrodes. This function defines a minimal size of the deep p-well as illustrated on the left-hand picture of Figure 7.29. The maximum size of the deep p-well is given by the opening as shown on the right-hand picture. In addition to these two pixel designs, the TJInv also contains pixels with a medium deep p-well size as shown in the middle picture [43].

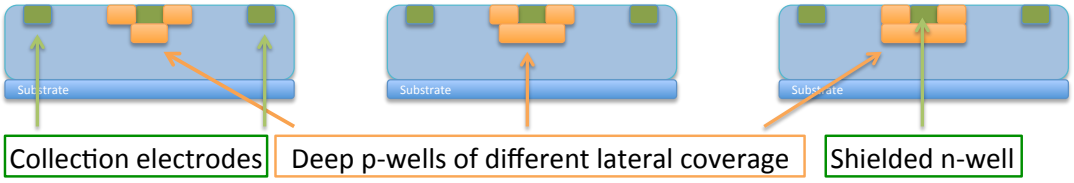


**Figure 7.29.** *The deep p-well is needed to shield n-wells from the p-type epitaxial layer. There are different options for the deep p-well size implemented in different matrices in the TJInv.*

The deep p-well is currently biased with the same potential of $HV$ as the substrate and the electric field below is relatively weak. The source measurements of M106 have proven charge sharing in combination with fast hits and the testbeam results show high efficiency but the mentioned reduction of charge. Structure M106 has a maximum deep p-well.

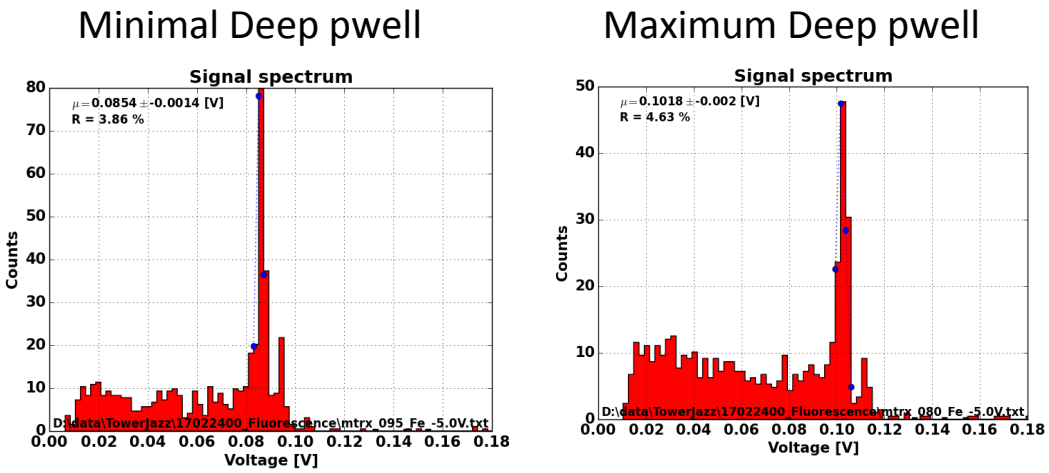


**(a)** *M95 - Minimum deep p-well* **(b)** *M80 - Maximum deep p-well*

**Figure 7.30.** *Single-pixel spectra for 28 µm matrices with minimum deep p-well (a) and maximum deep p-well (b) were recorded in Glasgow for $HV = -6$ V [60].*

In order to test the effect of the deep p-well size, structures of the TJInv with the same characteristics in terms of pixel size (28 µm), collection electrode size (3 µm), spacing (3 µm) and pixel circuit (active reset) but different deep p-well sizes were selected. Structure M95 has a minimum deep p-well and Matrix M80 has a maximum deep p-well size implemented.

The measurements were performed both at Glasgow using the fluorescence setup and at CERN using source scans. Both measurements used the Time-precision setup but the Glasgow setup contained a different oscilloscope than the DRS4 and the samples were biased with only $HV_{\text{Glasgow}} = -5\,\text{V}$. The $^{55}$Fe spectra generated by the fluorescence target in the Glasgow setup are shown in Figure 7.30 for an unirradiated sample. The deep p-well size influences the peak position. A higher signal and better energy resolution – visible also in a better separation of the $k_\alpha$ and $k_\beta$ lines – is obtained for the maximum deep p-well structure. The gain differences between the investigated structures again based on differences in the pixel capacitance. A visible difference in the single-pixel spectra is the contribution of hits with smaller amplitudes, indicating a stronger charge sharing for the maximum deep p-well structure.

In order to investigate this effect further – especially for sensors after irradiation – five pixels had been read out simultaneously in the source measurements at CERN. The cross-shaped configuration is shown in Figure 7.31a: One pixel was used as trigger pixel and the four adjacent pixels which share a side had been read out as well. As for testbeam measurements, the number of pixels was limited by the number of cividec amplifiers. These five-pixel measurements were performed at the very end during a short time window when five amplifier were available and not needed in other setups. Unfortunately, the time was insufficient to repeat the measurements presented earlier.

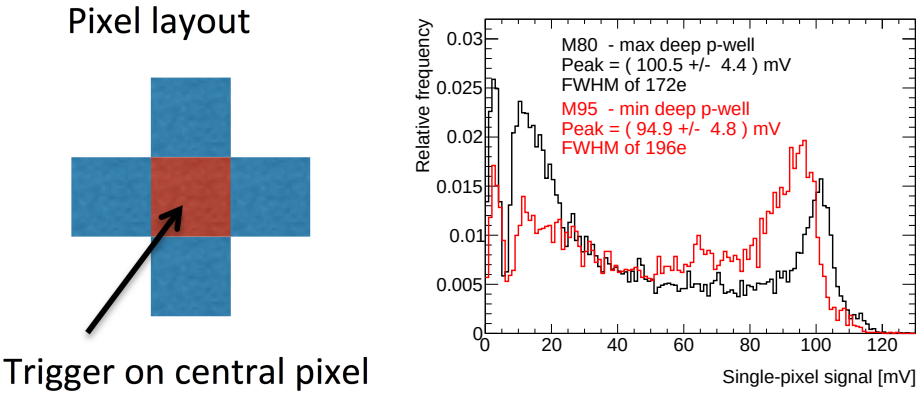


**(a)** *Pixel configuration* **(b)** $^{90}$*Sr energy spectra*

**Figure 7.31.** *Pixel configuration (a) and single-pixel spectra of $^{55}$Fe after $1.0\times10^{15}$ n/cm$^2$ (b).*

Single-pixel spectra were recorded for $^{55}$Fe on a sensor irradiated to $1.0\times10^{15}\,\text{n/cm}^2$. The spectra are shown in Figure 7.31b and agree with the results obtained for an unirradiated sample in Glasgow. The maximum deep p-well geometry shows a higher peak position and better energy resolution than the minimum deep p-well geometry. Like for the unirradiated sensor, the maximum deep p-well leads to a stronger charge sharing contribution.

In order to see the effect on MIP-like particles, the measurement has been repeated with a $^{90}$Sr source. The converted energy spectra are shown in Figure 7.32.

The red spectrum of the minimum deep p-well geometry in red contains the MPV peak of a MIP spectrum whereas the shape of the spectrum for the maximum deep p-well geometry in black equals a spectrum distorted by strong charge sharing as simulated before.

In order to prove this, the charges deposited in all five recorded pixels are summed up. The resulting spectra are given in Figure 7.32b. Since only five pixels are summed up, the presented spectrum does not equal the true 'cluster charge spectrum' of the MIP hits. But the comparison between five-pixel cluster spectra and single-pixel spectra still gives insight in the different performances.

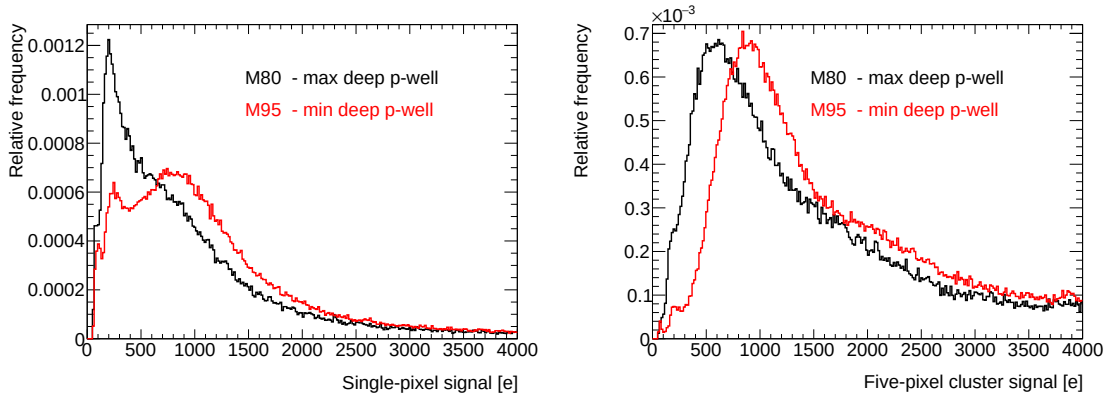


**(a)** $^{90}Sr$ *single-pixel spectra* **(b)** $^{90}Sr$ *five-pixel cluster spectra*

**Figure 7.32.** *Converted single-pixel (a) and five-pixel energy (b) spectra of* $^{90}Sr$ *after* $1.0\times10^{15}$ $n/cm^2$.

Both five-pixel spectra include a visible global maximum. The maximum deep p-well structure in black has a lower peak position around 662 e than the minimum deep p-well structure in red with a peak around 921 e. The spectra also appear to have additional contributions in the form of local maxima at higher values compatible with MPV positions around the expected value of 1575 e. If those peaks were to represent the true and only MPVs, the first peak would need to be a very high noise peak which is unlikely considering its dominance.
This leads to the assumption that the five-pixel cluster spectra contain two contributions with different MPVs. At the edges of the pixel, the thickness of the charge collection volume is reduced by the thickness of the CMOS circuitry. Assuming a thickness of a few micrometers, this can not explain the observed lower contribution.

Regarding the observed charge map of the 30 µm pixel structure, the contribution with higher MPV is mainly collected around the collection electrode. Since the peak is at a higher position than in the single-pixel spectrum, charge sharing is still present for these cases. The dominant contribution with lower MPV then represents events collected at different areas of the sensor which are subject to possible charge loss. Considering the amount of charge sharing and the limits of this five-pixel readout and the four-pixel readout in testbeam, the estimated MPVs are a lower limit to the true deposited cluster charge.

Based on the obtained results, a minimum deep p-well design is favourable to maximise the amount of collected charge. This holds valid for both local maxima in the five-pixel cluster spectrum. The downside is an almost 6 % gain reduction and a 14 % worse energy resolution in the $k_\alpha$ peak. The investigated 30 µm pixel structure M106 is a maximum deep p-well design.
Unfortunately, the TJInv does not contain an equivalent structure with minimum deep p-well but it is to expect that such a modification leads to an increase in collected charge and therefore in hit-detection efficiency.

## 7.6. Summary

In order to enhance depletion after radiation and therefore increase radiation hardness, a process modification was successfully developed and tested. Due to the nature of the process modification, the sensors could be glued and bonded to the same carrier boards and measured in the Time-precision setup.

X-ray fluorescence measurements showed the identical classification of structures as LG and HG and the direct comparison of unirradiated sensors revealed a reduction of gain caused by an expected increase in capacitance. The values of the reduction are different for the investigated structures but range from 20 % to 30 % and the Modified Process is still considered a low-capacitance design.
The horizontal p-n junction of the Modified Process also leads to a more narrow timing distribution, representing a more uniform charge collection across the epitaxial volume. The analysed single-pixel spectra indicate a reduced charge sharing between pixels compared to the Standard Process. This was confirmed by measurements performed with the ALICE multichannel setup.

The Time-precision setup was installed at a beamline of the DIAMOND synchrotron facility to obtain position-sensitive information with monochromatic photons. The performed measurements on an unirradiated sensor show the expected full depletion already at a bias voltage of $HV = 0\,\mathrm{V}$. The previously simulated effect of charge sharing on photon spectra could be confirmed by comparing measurements at the edge and at the center of the recorded pixel.

As for the Standard Process before, a neutron irradiation campaign was performed for sensors of the Modified Process. The process modification succeeded in maintaining good signals even after a NIEL fluence of $1.0\times10^{15}\,\mathrm{n/cm^2}$. In the case of the 50 µm pixels, an additional gain decrease and in the case of the 30 µm pixels a gain increase after irradiation was observed. It is assumed that this difference is caused by different capacitance components being dominant in the structures. The difference also leads to an increase in signal rise time for the 50 µm pixels and a decrease for the 30 µm pixels.

In 2017, the cooling box was included in the DIAMOND synchrotron testbeam and irradiated sensors were tested. A high level of charge sharing could be observed, around 30 % of the hits recorded in one pixel were also acknowledged as hits in one adjacent pixel.

While scanning, this value kept stable even when the X-ray beam was hitting the center of the trigger pixel and then decreased linearly beyond. Assuming this behaviour to be equal for all pixels, a high full cluster size is expected when reading out a full pixel grid.

Measurements with 180 GeV pions at the CERN SPS testbeam showed the significant improvement in hit-detection efficiency after irradiation. The obtained results were conclusive despite the limitation of a four-pixel readout and an active area in the order of magnitude of the telescope resolution.
For the 50 µm pixels, an overall efficiency over the central area was measured to be 87.9 % ± 1.4 % (stat.) ± 0.6 % (syst.). For the smaller 30 µm pixels, the overall efficiency was measured as 97.4 % ± 1.5 % (stat.) ± 0.6 % (syst.).
Due to the data transmission – analogue signals transported over several centimetres of cable – these efficiency values represent lower limits for the true efficiency of the pixel cell. A chip equipped with digital front-end functionality integrated in the pixels is expected to perform with a higher S/N, leading to lower thresholds and higher efficiency at areas with strong charge sharing.

The obtained $^{90}$Sr spectra indicated a potential increase of charge sharing or a charge loss for the smaller pixels after irradiation. The map of collected charge showed a lower value of collected charge than expected with exception of the area around the collection electrode. Investigations with radioactive sources and a five-pixel cluster readout provided further signs for charge loss in areas other than the collection electrode. By comparing structures with a minimum and a maximum deep p-well geometry, a beneficial effect of the minimum deep p-well pixel cell could be detected. These results can be used to decrease the radiation-damage induced charge loss and to support hit-detection efficiency.

# 8. Impact of the n-layer implant doping concentration

The additional n-layer implant proved to be a successful process modification to enhance depletion after irradiation and radiation hardness. The concentration of the n-layer directly affects the capacitance of the pixel cell. In the case of an extreme low n-type doping, the sensor behaves more similar to the Standard Process where this layer is p-doped equal to the epitaxial layer. This results in a very low capacitance but – as seen in the SPS testbeam measurements – also in an insufficient radiation hardness. In the case of a very high n-type doping, the sensor is more radiation hard but its capacitance rises until the point where the design gets closer to a high fill-factor approach instead of a low capacitance one.
The design aim is a beneficial balance, i.e. lowering the doping concentration as far as possible without loosing radiation hardness for the specific application. As mentioned earlier, the Standard Process might provide the best option for a low-radiation environment but fails to fulfil the requirements of the ATLAS ITk.
TJInv chips were produced on wafers with two different doping concentrations, previously referred to as **M**odified **P**rocess **1** (MP1) in case of a higher doping concentration and **M**odified **P**rocess **2** (MP2) in case of a lower doping concentration. All results presented up to this point were obtained with MP1 unless stated otherwise.

## 8.1. Sensor performance before irradiation

Measurements for unirradiated 28 µm pixels performed in the multi-channel setup have been previously shown on page 84. The results agree with the expectation that a low doping concentration leads to a performance between the Standard Process and the higher doping Modified Process. Due to the lower capacitance of MP2, the obtained gain is almost in the order of the Standard Process. On the other hand, MP2 has a charge sharing comparable with MP1. The benefits of a lower and more uniform signal rise time are also visible.

### Measurements on 30 µm pixel structures

Measurements of the 30 µm pixel structure M106 on unirradiated MP2 were performed. Regarding its high gain, it is expected to be sensitive to potential effects. The signal spectra of $^{55}$Fe are shown in Figure 8.1a. The gain of MP2 is very close to the one of the Standard Process and almost 28 % higher than the one of MP1. It slightly surpasses the one of the Standard Process.

This increase of 4 % is not understood as result of the process modification. It might be caused by production differences between wafers or by shifts in the transfer functions which affects the HG structures.

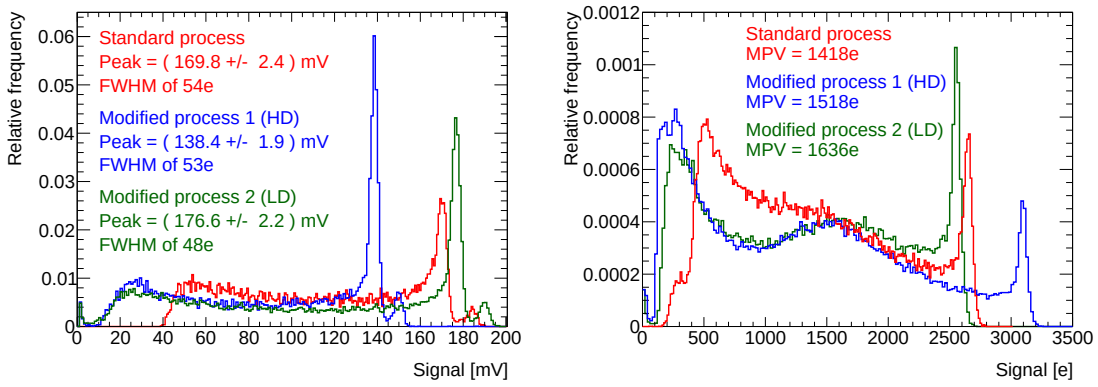


**(a)** *$^{55}$Fe signal spectra* **(b)** *$^{90}$Sr energy spectra*

**Figure 8.1.** *Signal spectra of $^{55}$Fe (a) and $^{90}$Sr (b) for the 30 µm pixel structure M106 produced in the Standard Process and the two Modified Processes.*

The converted energy spectra of $^{90}$Sr are shown in Figure 8.1b. As seen previously for 28 µm pixels, the Modified Processes of both doping concentrations have a similar level of charge sharing and a similar value for the peak of the distribution. The higher gain of MP2 causes a lower saturation energy of around 2550 e compared to around 3100 e for MP1. The spectra show the expected benefits of a lower doping concentration. Pixel capacitance and gain are comparable to the Standard Process, whereas charge sharing and charge-collection behaviour are comparable to the performance of MP1.

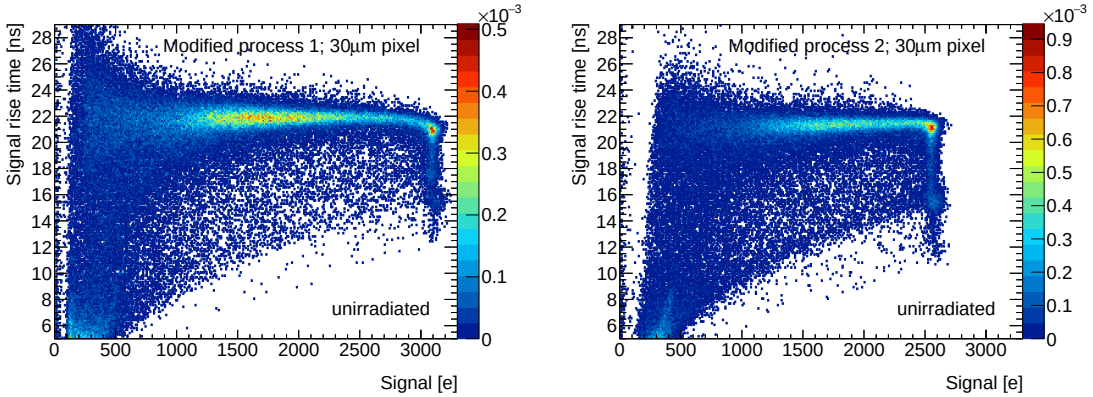


**(a)** *MP1 – high doping* **(b)** *MP2 – low doping*

**Figure 8.2.** *2d correlations of MP1 (a) and MP2 (b) on structure M106. The higher gain of the lower doping profile on the right-hand side results in a lower saturation energy.*

The correlations of signal rise time and converted energy spectra are compared in Figure 8.2. Both correlations show a narrow signal rise time distribution, and agree apart from the mentioned difference in saturation energy.

### Measurements on 50 µm pixel structures

Comparing measurements were also performed for M129. This structure also has a maximum deep p-well size. The signal spectra of $^{55}$Fe are shown in Figure 8.3a. For the bigger pixels, the gain of MP2 is comparable to the gain of MP1. This indicates that in this case the total pixel capacitance is dominated by another contribution less dependent of the doping concentration. Peak width and therefore energy resolution of MP1 and MP2 also coincide at around 200 e. The converted energy spectra of $^{90}$Sr are shown in Figure 8.3b and the three distributions agree within the resolution.

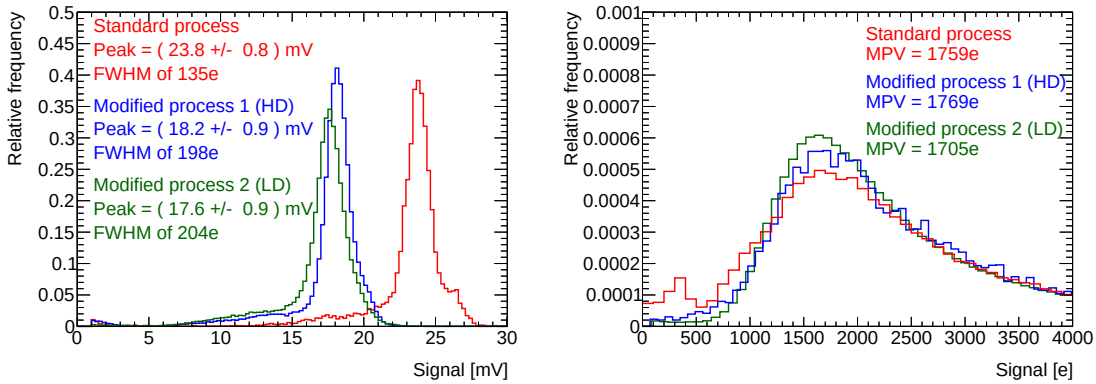


**(a)** *$^{55}$Fe signal spectra* **(b)** *$^{90}$Sr energy spectra*

**Figure 8.3.** *Signal spectra of $^{55}$Fe (a) and $^{90}$Sr (b) for the 30 µm pixel structure M129 produced in the Standard Process and the two Modified Processes.*

The correlations of signal rise time and converted energy spectra are compared in Figure 8.4. As observed before, the distributions agree regarding the energy spectrum but the one of MP2 seems to be slightly shifted towards higher signal rise times.

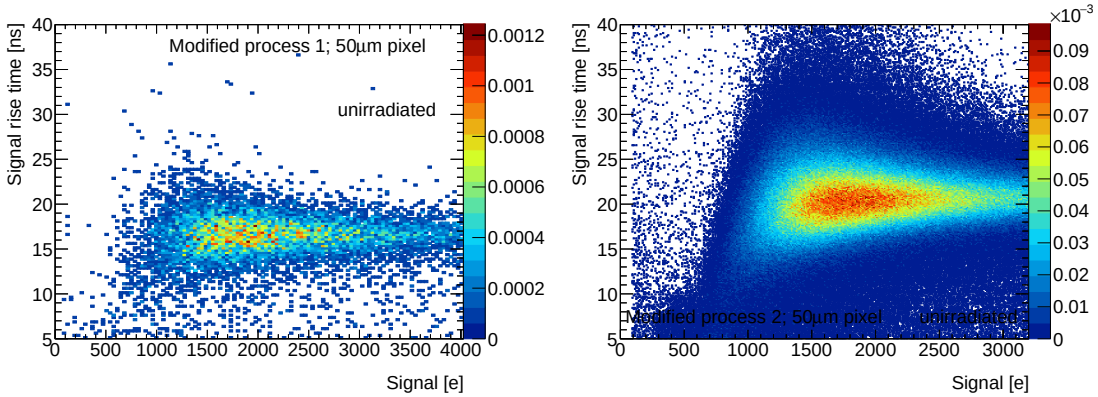


**(a)** *MP1 – high doping* **(b)** *MP2 – low doping*

**Figure 8.4.** *2d correlations of MP1 (a) and MP2 (b) on structure M129. (The presented data sets contain different levels of statistics.)*

## 8.2. Sensor performance after irradiation

Before irradiation, MP2 showed the expected higher gain due to a lower pixel capacitance for the 30 µm pixel structure M106. In the case of the 50 µm pixel structure M129, the performance was more comparable to MP1.
The critical point is the performance after irradiation and if a higher gain and S/N can be achieved while obtaining a hit-detection efficiency comparable to MP1.

### Measurements on 30 µm pixel structures

The results for the 30 µm pixel structure M106 are shown in Figure 8.5. For MP2, the shape of the distribution is comparable with the one of MP1. It contains a clear $k_\alpha$ of $^{55}$Fe and no shape difference indicating a stronger charge sharing than MP1 is observed. The advantage in gain of MP2 compared to MP1 is still present but reduced to around 11 %.

The converted energy spectra of $^{90}$Sr in Figure 8.5b show differences between both doping Modified Processes. The peak is at a lower value of 567 e for the lower doping concentration than 738 e for the higher doping concentration. Since in the first case, the peak seems to have further fused with the distribution, the true MPV might be even lower. Such a shift can be caused by either a higher level of charge sharing or by actual charge loss due to reduced depletion. Unfortunately, no MP2 sensor was included in the CERN SPS testbeam campaign.

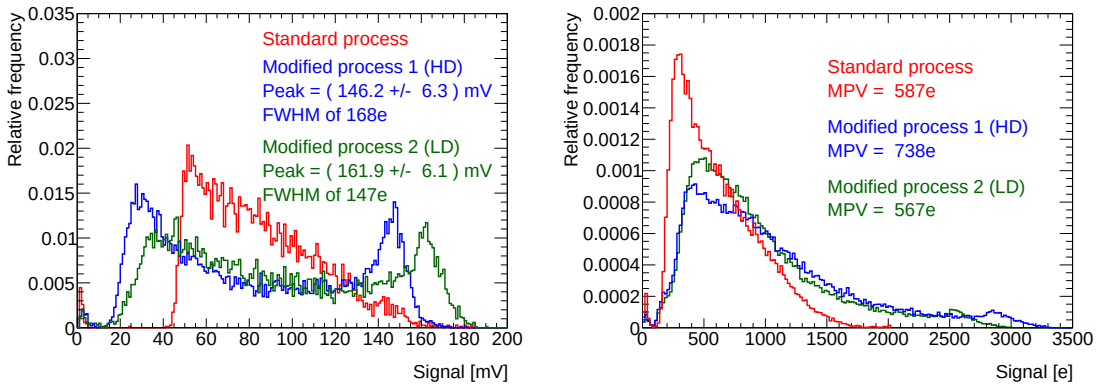


**(a)** *$^{55}$Fe signal spectra* **(b)** *$^{90}$Sr energy spectra*

**Figure 8.5.** *Signal spectra of $^{55}$Fe (a) and converted energy spectra $^{90}$Sr (b) for the 30 µm pixel structure M106 produced in the Standard Process and the two Modified Processes irradiated to $1.0\times10^{15}$ n/cm$^2$.*

The correlations of signal rise time and converted energy spectra are compared in Figure 8.6. Both irradiated sensors show a better performance after $1.0\times10^{15}$ n/cm$^2$ than the corresponding sensor of the Standard Process presented earlier. The improvement in radiation hardness is therefore successful for both levels of doping concentration.

The comparison between MP1 in Figure 8.6a and MP2 in Figure 8.6b shows a wider distribution in signal rise time and also a shift to lower values of collected charge for MP2. As seen in the converted $^{90}$Sr energy spectrum, it might also be that the true distribution peak is lower and cut away by the threshold.

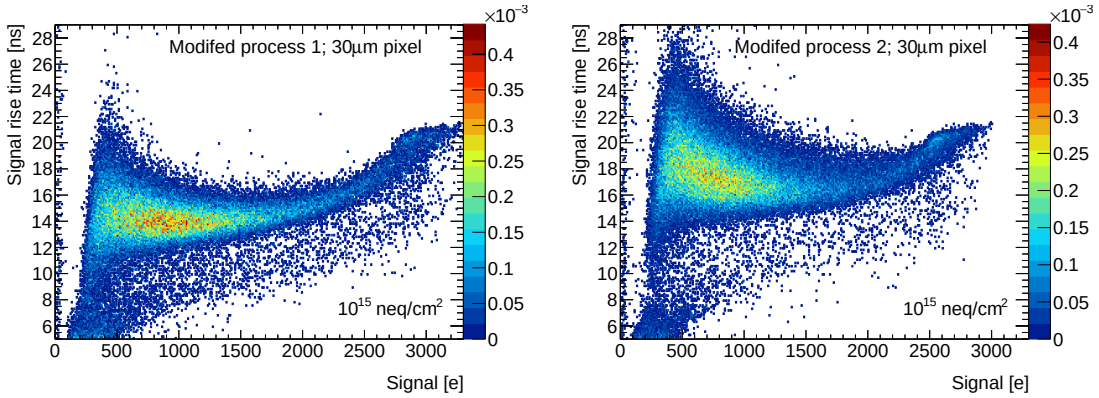


**(a)** *MP1 – high doping* **(b)** *MP2 – low doping*

**Figure 8.6.** *2d correlations of MP1 (a) and MP2 (b) on structure M106 after $1.0\times10^{15}$ n/cm$^2$*

For structure M106, a higher doping concentration of the n-type implant leads to more narrow and uniform results after $1.0\times10^{15}$ n/cm$^2$.

### Measurements on 50 µm pixel structures

Reducing the doping concentration did not improve the performance of structure M129 before irradiation. Being closer to the Standard Process, no improvement is expected to be observed after irradiation. The signal spectra of $^{55}$Fe after $1.0\times10^{15}$ n/cm$^2$ are shown in Figure 8.7a. The positions of the $k_\alpha$ peaks indicate a huge gain difference of a factor of 2 between MP1 and MP2 but the width of the MP2 peak and the corresponding energy resolution show severe degradation.

The converted energy spectra in Figure 8.7b show no sign of degradation, all three distributions agree very well with each other.
As before for the comparison of Standard Process and MP1, the degradation is not visible in the $^{90}$Sr spectrum but in the distribution of signal rise time and the 2d correlation presented in Figure 8.7.
While only a slight increase in time is visible for MP1, the sensor of type MP2 with lower doping concentration shows no narrow distribution after irradiation to $1.0\times10^{15}$ n/cm$^2$. It spans in both directions, similar to the corresponding performance presented of the Standard Process presented earlier. The difference to MP1 and similarity to the Standard Process is probably the effect of type-inversion in the n-layer. Since type inversion is observed to start around $10^{14}$ n/cm$^2$, it can also affect the measured sensors.

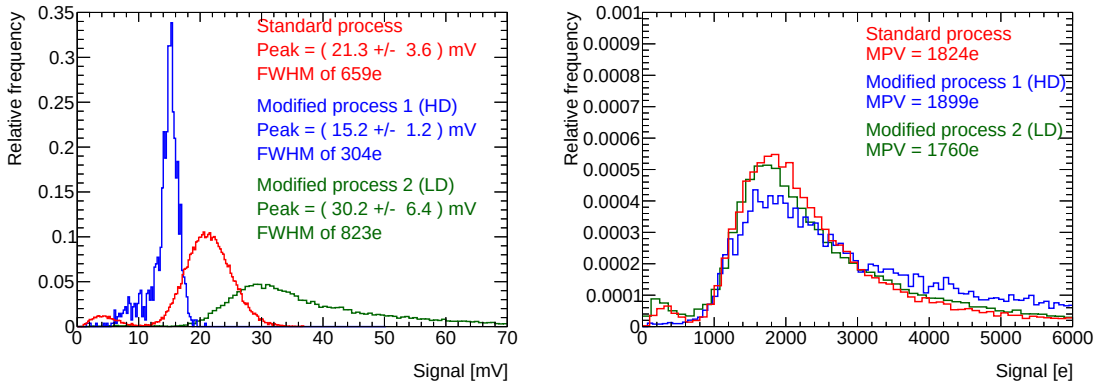


**(a)** *$^{55}Fe$ signal spectra* **(b)** *$^{90}Sr$ energy spectra*

**Figure 8.7.** *Signal spectra of $^{55}Fe$ (a) and converted energy spectra $^{90}Sr$ (b) for the 50 µm pixel structure M129 produced in the Standard Process and the two Modified Processes irradiated to $1.0\times10^{15}$ n/cm$^2$.*

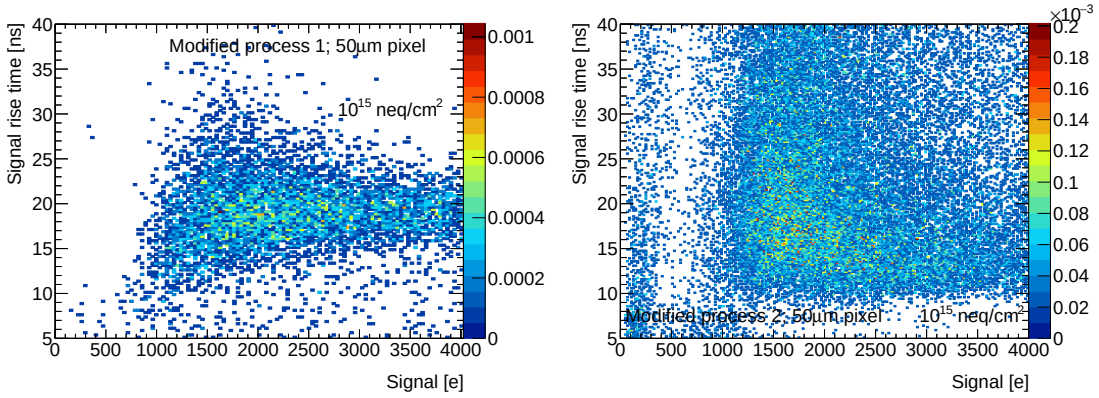


**(a)** *MP1 – high doping* **(b)** *MP2 – low doping*

**Figure 8.8.** *2d correlations of MP1 (a) and MP2 (b) on structure M129. The higher gain of the lower doping profile on the right-hand side results in a lower saturation energy.*

Type inversion being a continuous effect, the n-type layer with higher doping concentration remains a higher concentration after $1.0\times10^{15}$ n/cm$^2$ than the one with the lower doping concentration. In the latter case, the n-type layer has inverted closer to the properties of the Standard Process. The effect is more visible in the structure with larger pixels due to failing depletion far away from the collection electrodes.

## 8.3. Summary

Sensors of the Modified Process are equipped with an additional n-type layer in the p-type epitaxial layer to create a horizontal p-n junction and enhance depletion after irradiation. Since the doping concentration of this layer is an open parameter with strong potential impact on the performance, TJInv chips were produced with two different values of doping concentration.

Before irradiation, the sensor of type MP2 – lower doping concentration – showed the expected higher gain in case of the 30 µm structure M106, similar to the Standard Process. This gain difference could not be observed for the 50 µm pixel structure M129. For different structures, different components dominate the total pixel capacitance and thus the gain.
Investigations with $^{90}$Sr proved both Modified Process types to work comparably in terms of charge collection and signal rise time before irradiation.

After irradiation to $1.0\times10^{15}\,\mathrm{n/cm^2}$, differences between both doping concentrations became visible. On one hand, the measurement with M129 implies that the n-type layers of both doping concentrations are affected by changes of their effective doping concentration. Due to the different initial concentration, the n-type layer in MP2 reduces sooner and the sensor looses the additional implant and resulting horizontal p–n junction. Its performance is then expected to be similar to the Standard Process which was observed.

On the other hand, the measurement with M106 shows a stronger degradation for MP2 than for MP1 but both perform significantly better than the Standard Process after irradiation to $1.0\times10^{15}\,\mathrm{n/cm^2}$. This difference is a sign that the type inversion is not complete and that the n-layer of remaining concentration in MP2 is still capable of depleting the smaller pixel structure. A stronger degradation is observed in higher signal rise times and less collected charge. Whether the reduced collection is caused by charge sharing or actual charge loss in the pixel volume could not be determined.

All results agree that a lower doping concentration might be a beneficial option for a low-radiation environment since a higher doping concentration increases the pixel capacitance and therefore reduces the advantages of the low-capacitance design in terms of power consumption and S/N.
After irradiation damage expected in the outer layers of the ATLAS ITk, the lower doping concentration leads to a worse results in the case of both investigated structures. Since a higher doping concentration can improve radiation hardness and signal conformity, the overall optimum regarding charge-collection efficiency and hit-detection efficiency might be higher than for the investigated MP1.

# 9. Summary and Outlook

The HL-LHC upgrade will enhance the instantaneous luminosity of the LHC and provide the experiments with a significant amount of recorded data for the ambitious physics programs to come. The ATLAS experiment has launched intensive R&D programs to upgrade detector components with the increasing challenges in mind. One R&D program is the new ATLAS ITk containing several square metres of silicon detectors in five layers of silicon pixel sensors. The detectors have to perform under high requirements regarding hit rate, readout time and radiation hardness over several years of planned lifetime.

Depleted Monolithic Active Pixel Sensors produced in a commercial CMOS imaging process are investigated as promising alternative to more expensive and power consuming hybrid pixel sensors. In the context of this thesis, sensors produced in the TowerJazz 180 nm technology were studied. Its capabilities for tracking devices had been proven and sensors are currently in production for the Inner Tracker Upgrade of the ALICE detector. Encouraged by the results, performance tests regarding the requirements of the ATLAS ITk were started.

A test chip designed during the ALICE R&D program – the TowerJazz Investigator – was used for the measurements presented in this thesis. The chip consists of 134 substructures with different geometric properties of the pixel cell. The pure analogue readout enables studies of the charge collection in the pixel volume. Per structure, a maximum of 64 pixels are available to be read out simultaneously.

A dedicated new setup for the ATLAS Investigator program was planned, built and operated in the context of this thesis. The focus of the setup was a high timing resolution and a compact design to enable operation at low temperatures in the laboratory as well as at testbeam facilities inside and outside of CERN. This Time-precision setup has continuously been improved to maximise signal-to-noise ratio and readout capabilities. The recorded waveforms are analysed by a software framework adapted to the setup and its properties. The used fit was validated and the robustness against Gaussian and harmonic noise was shown.

Sensors of the Standard Process were successfully tested, confirming the good results obtained by the ALICE group. Further tests using X-ray fluorescence photons and highly-focused synchrotron beams were performed and added to the portfolio of procedures. The test indicated the influence of geometric parameters on the pixel performance and the potential for optimisation. The shape of the obtained spectra and the effect of charge sharing were motivated by simulations based on simple assumptions. Further measurements of irradiated samples and the comparison of different substructures agreed with the qualitative statements of the simulations.

The sensors of the Standard Process showed good performance before neutron irradiation. Unfortunately, after fluences comparable to the expectations in the outer layers of the ATLAS ITk, the sensor performance worsened drastically, showing severe radiation damage in the charge collection volume. The sensor irradiated to $1.0\times10^{14}\,\mathrm{n/cm^2}$ was functioning but the results of a performed CERN SPS testbeam showed beginning degradation of hit-detection efficiency. The sensor irradiated to $1.0\times10^{15}\,\mathrm{n/cm^2}$ was barely capable of providing reliable signals and the signals failed the requirements in terms of charge collection, signal rise time and hit-detection efficiency.

A new sensor design included an additional n-layer. Motivation was the enhancement of depletion in the epitaxial volume by creating a horizontal p–n junction. The process modification did not cause additional changes to the pixel design. This way, the same setup and measurement procedures could be used for comparisons between both processes.
The process modification led to an increase of capacitance for the unirradiated sensors of 20 % to 30 % – depending on the substructure – which was detected as reduction in gain. A more uniform depletion and a more uniform signal rise time were visible over the sensor. The charge collection properties after gain calibration were comparable to the ones of the Standard Process. Measurements at the DIAMOND synchrotron facility showed full depletion already at a bias voltage of $HV = 0\,\mathrm{V}$.
After neutron irradiation, the process modification showed its successful enhancement of depletion and sensor performance. Even after $1.0\times10^{15}\,\mathrm{n/cm^2}$, reliable and fast signals were recorded.

During a CERN SPS testbeam, the irradiated sensors showed a high hit-detection efficiency, depending on the pixel size of the structure under test. An overall efficiency of $98.5\,\% \pm 1.5\,\%$ (stat.) $\pm$ $1.2\,\%$ (syst) after irradiation to $1.0\times10^{15}\,\mathrm{n/cm^2}$ was obtained for the investigated $25\,\mu\mathrm{m}$ pixel structure. The measurement could be performed with an active area of only $2\times2$ pixels and effects caused by the telescope resolution were corrected. The estimated efficiencies are lower limits to the efficiencies of the sensors, affected by a high noise level in the testbeam environment and charge sharing at the pixel boundaries. The transmission of analogue signals over several centimetres of cable is a weak point of the setup but could not be avoided.
Charge sharing and potential charge loss were further investigated in a five-pixel cluster measurement in the climate chamber. The obtained results proved a beneficial effect of a minimum deep p-well size. Since the structures tested in the SPS testbeam were of a maximum deep p-well design, a further increase of charge collection and hit-detection efficiency is expected for a corresponding design adaptation.

One last parameter under investigation was the doping concentration of the additional n-layer in the Modified Process. A lower doping concentration than previously measured was tested in the hope of reducing the pixel capacitance and increasing the gain to a level comparable to the Standard Process. Unirradiated sensors fulfilled this expectation, showing an excellent performance of high gain and uniform charge collection, proving this doping concentration to be a promising option for low-irradiation applications.

The performance of the corresponding irradiated sensors showed degradations, concluding the higher doping concentration to be beneficial.

Based on these results, the next generation of Investigator test chips was produced with the high doping concentration of MP1 and an even higher option. This new concentration might protect the sensor even further against radiation damage at the cost of a higher capacitance and a reduced gain. Future measurements in laboratory and testbeam will show if a higher charge collection leads to an improved overall performance.

## 9.1. Outlook

The ATLAS ITk CMOS community followed the R&D process presented in this thesis – and especially the significant improvements of the Modified Process – with great interest. The first results of the Standard Process proved the principles of the technology, especially the capability of fast charge collection. The first results of the Modified Process after irradiation proved that DMAPS technologies might soon enter applications in high-radiation environments.
Alongside understanding, the investigations were also serving the purpose of helping the chip designers creating a new generation of chips. These chips contain the TowerJazz 180 nm technology with process modification in a full-size pixel array including digital circuitry. The new **M**onolithic from **AL**ICE **T**o **A**TLAS (MALTA) chip has a full ITk size of 20 mm×22 mm, containing 512×512 pixels of 36.4 µm pixel size. The presented investigations of the 30 µm structure M106 delivered important input. More information concerning MALTA can be found in Ref. [61].
Using the knowledge gained, these chips are a huge step closer to final sensors. The signals are processed directly in each pixel cell, removing limiting factors for the hit-detection efficiency. A full pixel array allows for deeper investigations of cluster sizes and cluster charges. It also increases the collected statistics in laboratory and testbeam measurements. Measuring an entire array also reduces the effect of finite telescope resolution significantly.
The measurements on the TowerJazz Investigator contributed valuable input and had great impact on the CMOS R&D program for the ATLAS ITk. Groups of several institutes joined the ATLAS Investigator program, using provided replica of the Time-precision setup or adapting their setups based on the experiences obtained in the context of this thesis. The local CERN group designed and constructed a fluorescence setup to include this measurement method into its portfolio.
The next generation of test chips are expected to continue this effort in the direction of such a modern and promising technology.

# Bibliography

[1] American Physics Society, *APS NEWS - October 1897: The Discovery of the Electron* Series 2, **9**, No. 9 (2000).

[2] **DONUT** Collaboration, K. Kodama et al., *Observation of tau neutrino interactions*, Phys. Lett. B, **504** (2001), FERMILAB-PUB-00-335-E.

[3] `https://commons.wikimedia.org/wiki/File:Standard_Model_of_Elementary_Particles.svg`, Accessed: 2018-03-07.

[4] P. W. Higgs, *Broken Symmetries and the Masses of Gauge Bosons*, Phys. Rev. Lett., **13** (1964), 508–509.

[5] **ATLAS** Collaboration, *Observation of a new particle in the search for the Standard Model Higgs boson with the ATLAS detector at the LHC*, Phys. Lett. B, **716** (2012), CERN-PH-EP-2012-218.

[6] **CMS** Collaboration, *Observation of a new boson at a mass of 125 GeV with the CMS experiment at the LHC*, Phys. Lett. B, **716** (2012), CMS-HIG-12-028, CERN-PH-EP-2012-220.

[7] L. Evans and P. Bryant, *LHC Machine*, *JINST*, **3** (2008), S08001.

[8] **ATLAS** Collaboration, *The ATLAS Experiment at the CERN Large Hadron Collider*, *JINST*, **3** (2008), S08003.

[9] C. Pralavorio, *Record luminosity: well done LHC*, CERN Press release (2017), `https://cds.cern.ch/record/2295027`.

[10] E. A. Mobs, The CERN accelerator complex. Complexe des accÃ©lÃ©rateurs du CERN, OPEN-PHO-ACCEL-2016-013 (2016).

[11] Particle Data Group Collaboration, K. Nakamura et al., *Review of particle physics*, J. Phys. G, **37** (2010), 277.

[12] C. Gemme on behalf of the ATLAS Collaboration, *The ATLAS tracker Pixel detector for HL-LHC*, Proceedings of the 25th International workshop on vertex detectors, Elba, Italy (2016).

[13] **ALICE** Collaboration, *The ALICE experiment at the CERN LHC*, *JINST*, **3** (2002), S08003.

[14] F. Hartmann, *Evolution of silicon sensor technology in particle physics; 2nd ed.*, Springer, Berlin (2017).

[15] H. Kolanski, N. Wermes, *Teilchendetektoren*, Springer, Berlin (2016).

[16] S. Fernandez-Perez, *A novel Depleted Monolithic Active Pixel Sensor for future High Energy Physics Detectors*, CERN-THESIS-2016-042 (2016).

[17] C. Patrignani et al. (Particle Data Group), Chin. Phys. C, **40**, 100001 (2016), Table 38.1, 441.

[18] A. Rivetti, *CMOS: Front-End Electronics for Radiation Sensors*, CRC Press, Boca Raton (2015), 83–87.

[19] N. Weste, D. Harris, *CMOS VLSI Design: A Circuits and Systems Perspective, 3rd Edition*, Pearson, Boston (2005).

[20] M. Huhtinen; *Simulation of non-ionising energy loss and defect formation in silicon*, Nucl. Instrum. Methods Phys. Res. A, 491 (2002), 194–215.

[21] J. Lindhard, V. Nielsen, Nuclear collisions and ionisation fluctuations in charged particle detectors, Phys. Lett., 2 (1962), 209–211.

[22] M. Garcia-Sciveres, N. Wermes, *Advances in pixel detectors for experiments with high rate and radiation*, (2017), arXiv:1705.10150v1.

[23] F. Faccio et al., *Radiation-induced edge effects in deep submicron CMOS transistors*, IEEE Trans. Nucl. Sci., 52 (2015), 2413.

[24] F. Faccio et al., *Total ionizing dose effects in shallow trench isolation oxides*, Microelectron. Reliab., **48** (2008), 1000–1007.

[25] A. Rozanov, *Status and future of the ATLAS Pixel Detector at the LHC*, ATL-INDET-PROC-2013-003 (2013).

[26] A. Andreazza, *The ATLAS Pixel Detector operation and performance*, Proceedings of 19th International Workshop on Vertex Detectors - VERTEX (2010).

[27] K. Potamianos, *The upgraded Pixel detector and the commissioning of the Inner Detector tracking of the ATLAS experiment for Run-2 at the Large Hadron Collider*; EPS-HEP 2015 Proceedings , ATL-PHYS-PROC-2016-104 (2016).

[28] B. Abbott et al., *Production and Integration of the ATLAS Insertable B-Layer JINST*, **13** (2018), T05008.

[29] **ATLAS** Collaboration, *Technical Design Report for the ATLAS Inner Tracker Pixel Detector*, CERN-LHCC-2017-021. ATLAS-TDR-030 (2017).

[30] **ATLAS** Collaboration, *Letter of Intent for the Phase-II Upgrade of the ATLAS Experiment*, CERN-LHCC-2012-022 (2012), pp. 1, pp. 57, p. 72.

[31] M. Backhaus, *Radiation-hard active CMOS pixel sensors for HL-LHC detector upgrades*, *JINST*, **10** (2015), C02031.

[32] J. Schambach et al., *A MAPS Based Micro-Vertex Detector for the STAR Experiment*, The 23rd International Conference on the Application of Accelerators in Research and Industry - CAARI 2014, Phys. Procedia, 66 (2015), 514–519.

[33] M. Šuljić on behalf of the ALICE collaboration, *ALPIDE: the Monolithic Active Pixel Sensor for the ALICE ITS upgrade*, *JINST*, **11** (2016), C11025.

[34] L. Musa, *ALICE Inner Tracking System Upgrade*, 2016 ECFA workshop, Aix-Les-Bains, https://indico.cern.ch/event/524795/contributions/2236600/attachments/1348153/2033839/ECFA_OCT_2016_ALICE_ITS.pdf.

[35] N. Wermes, *Depleted CMOS pixels for LHC proton-proton experiments*, Nucl. Instr. Meth. Phys. Res. A, **824** (2016), 483–486.

[36] W. Snoeys, *Monolithic pixel detectors for high energy physics*, Nucl. Instr. Meth. Phys. Res. A, **731** (2013), 125.

[37] Z.Y. Chang, W.M.C. Sansen, *Low-noise wide-band amplifiers in bipolar and CMOS technologies*, Kluwer Academic Publishers, Dordrecht, The Netherlands, (1991).

[38] **ALICE** Collaboration, *Technical Design Report for the Upgrade of the ALICE Inner Tracking System* (2013), CERN-LHCC-2013-024. ALICE-TDR-017.

[39] H. Pernegger et al., *First tests of a novel radiation hard CMOS sensor process for Depleted Monolithic Active Pixel Sensors*, *JINST*, **12** (2017), P06008.

[40] C. Gao et al., *A Novel Source-Drain Follower for Monolithic Active Pixel Sensors*, Proceedings of the 10th International "Hiroshima" Symposium on the Development and Application of Semiconductor Tracking Detectors, Elsevier, 831 (2016), 147–155.

[41] S. Senyukov, et al., *Charged particle detection performances of CMOS pixel sensors produced in a 0.18*µ*m process with a high resistivity epitaxial layer*, Nucl. Instr. Meth. Phys. Res. A, **730** (2013), 115–118.

[42] *Manual Investigator1, Version 2*, Internal communication

[43] Jerome Rousset, Jerome.Rousset@cern.ch, personal communication.

[44] Thanushan Kugathasan, Thanushan.Kugathasan@cern.ch, personal communication.

[45] W. Snoeys et al., *A process modification for CMOS monolithic active pixel sensors for enhanced depletion, timing performance and radiation tolerance*, Nucl. Instr. Meth. Phys. Res. A, **871** (2017), 90–96.

[46] C. Riegel, *Recent developments on monolithic CMOS pixel sensors in TowerJazz 180nm technology*, 13th Trento Workshop on Advanced Silicon Radiation Detectors, Munich (2018), https://indico.cern.ch/event/666427/contributions/2881304/attachments/1603219/2542430/Riegel_13thTrento.pdf.

[47] Enrico Junior Schioppa, Enrico.Junior.Schioppa@cern.ch, personal communication.

[48] J. Willem van Hoorne, *Study and Development of a novel Silicon Pixel Detector for the Upgrade of the ALICE Inner Tracking System*, CERN-THESIS-2015-255 (2015), 61.

[49] S. Ritt, *Development of high speed waveform sampling ASICs*, Proceedings of DAE-BRNS national symposium on nuclear instrumentation - 2010, `https://www.psi.ch/drs/evaluation-board`.

[50] CIVIDEC Instrumentation GmbH, `www.cividec.at`.

[51] C. Riegel et al., *Radiation hardness and timing studies of a monolithic TowerJazz pixel design for the new ATLAS Inner Tracker*, Proceedings of the 18th International Workshop on Radiation Imaging Detectors, Barcelona, Spain, *JINST*, **12** (2016), C01015.

[52] `http://ade-pixel-group.web.cern.ch/ade-pixel-group/Software/tbconverter.php`.

[53] S. Fernandez-Perez et al., *Charge Collection Properties of a depleted monolithic active pixel sensor using a HV-SOI process*, *JINST*, **11** (2016), C01063.

[54] K. G. McKay, K. B. McAfee, *Electron Multiplication in Silicon and Germanium*, *Phys. Rev.*, **91** (1953), 1079–1084.

[55] S. Meroli, D. Passeri and L. Servoli, *Energy loss measurement for charged particles in very thin silicon layers*, *JINST*, **6** (2011), P06013.

[56] M. Suljic, *Study of Monolithic Active Pixel Sensors for the Upgrade of the ALICE Inner Tracking System*, CERN-THESIS-2017-304 (2017), 49.

[57] K. Ambrožič, G. Žerovnik, L. Snoj, *Computational analysis of the dose rates at JSI TRIGA reactor irradiation facilities*, Appl. Radiat. Isot., **130** (2017), 140.

[58] D. Dannheim on behalf of the CLICdp Collaboration, *Silicon pixel-detector RD for CLIC*, 11th International "Hiroshima" Symposium on the Development and Application of Semiconductor Tracking Detectors (2017).

[59] Y. P. Varshni, *Temperature dependence of the energy gap in semiconductors*, Physica, **34** (1967), 149–154.

[60] Dzmitry Maneuski, `Dima.Maneuski@glasgow.ac.uk`, personal communication.

[61] H. Pernegger, *Monolithic Pixel Development in TowerJazz 180nm CMOS for the outer pixel layers in the ATLAS experiment*, 11th International "Hiroshima" Symposium on the Development and Application of Semiconductor Tracking Detectors (2017).

# List of Abbreviations

**ALICE** **A** **L**arge **I**on **C**ollider **E**xperiment ..... 7
**CMOS** **C**omplementary **M**etal-**O**xide **S**emiconductor ..... 1
**DMAPS** **D**epleted **M**onolithic **A**ctive **P**ixel **S**ensor ..... 1
**DUT** **D**evice **U**nder **T**est ..... 71
**FE** **F**ront-**E**nd
**FPGA** **F**ield **P**rogrammable **G**ate **A**rray ..... 37
**FWHM** **F**ull **W**idth **H**alf **M**aximum ..... 92
**GPAC** **G**eneral **P**urpose **A**nalog **C**ard ..... 37
**HEP** **H**igh **E**nergy **P**hysics ..... 3
**HG** **H**igh **G**ain ..... 58
**HL-LHC** **H**igh **L**uminosity **L**arge **H**adron **C**ollider ..... 6
**HV** **H**igh **V**oltage ..... 24
**IBL** **I**nsertable **B**-**L**ayer ..... 6
**ID** **I**nner **D**etector ..... 6
**IEL** **I**onizing **E**nergy **L**oss ..... 16
**ITk** **I**nner **Tr**ac**k**er ..... 1
**ITS** **I**nner **T**racking **S**ystem ..... 7
**LEP** **L**arge **E**lectron-**P**ositron Collider ..... 4
**LG** **L**ow **G**ain ..... 57
**LHC** **L**arge **H**adron **C**ollider ..... 4
**LS** **L**ong **S**hutdown ..... 6
**MALTA** **M**onolithic from **AL**ICE **T**o **A**TLAS ..... 121
**MAPS** **M**onolithic **A**ctive **P**ixel **S**ensor ..... 25
**MIO** **M**ulti-**IO** board ..... 37
**MIPs** **M**inimum **I**onizing **P**articles ..... 13
**MOS** **M**etal **O**xide **S**emiconductor ..... 15
**MP1** **M**odified **P**rocess **1** ..... 111
**MP2** **M**odified **P**rocess **2** ..... 111
**MPV** **M**ost **P**robable **V**alue ..... 13
**NIEL** **N**on-**I**onizing **E**nergy **L**oss ..... 16
**PCBs** **P**rinted **C**ircuit **B**oards ..... 37
**PSI** **P**aul **S**cherrer **I**nstitute ..... 37
**ROI** **R**egion **O**f **I**nterest ..... 72
**SCR** **S**pace **C**harge **R**egion ..... 11
**SCT** **Semi**conductor **T**racker ..... 6
**SPS** **S**uper **P**roton **S**ynchrotron ..... 4
**SM** **S**tandard **M**odel of Elementary Particle Physics ..... 3
**S/N** **S**ignal-to-**N**oise ratio ..... 19
**TID** **T**otal **I**onising **D**ose ..... 20
**TJInv** **T**ower**J**azz **Inv**estigator ..... 33
**TRT** **T**ransition **R**adiation **T**racker ..... 6

# List of Figures

# List of Tables

# A. Additional results and information

**Table A.1.** *The table lists supplies and control signals to operate the Investigator. The **IFOLx** current and the supply voltage are required with a certain value. The signals **SELECT[0..8]** and **RESET** are logic levels of 0 V or 1.8 V. Reset voltage and backbias HV voltage should not exceed a certain range.*

| Signal name | Description | Value | Comment |
|---|---|---|---|
| **IFOL1** | Pixel current | 500 nA | Created by pulldown to DAC |
| **IFOL2** | Mini-Matrix current | 60 µA | Created by pulldown to DAC |
| **IFOL3** | Column current | 60 µA | Created by pulldown to DAC |
| **IFOL4** | Output Buffer current | 60 µA | Created by pulldown to DAC |
| **1V8A** | Supply Voltage | 1.8 V | |
| **SELECT[0..8]** | Matrix Selection | 0 V or 1.8 V | Bit pattern for matrix selection |
| **VRESET** | Reset Voltage | up to 1 V | 1 V recommended |
| **RESET** | Reset pulse | 0 V or 1.8 V | Active low, 200 ns pulse width |
| **HV** | Backbias voltage | 0 V to -6 V | Current limit at -10 mA |

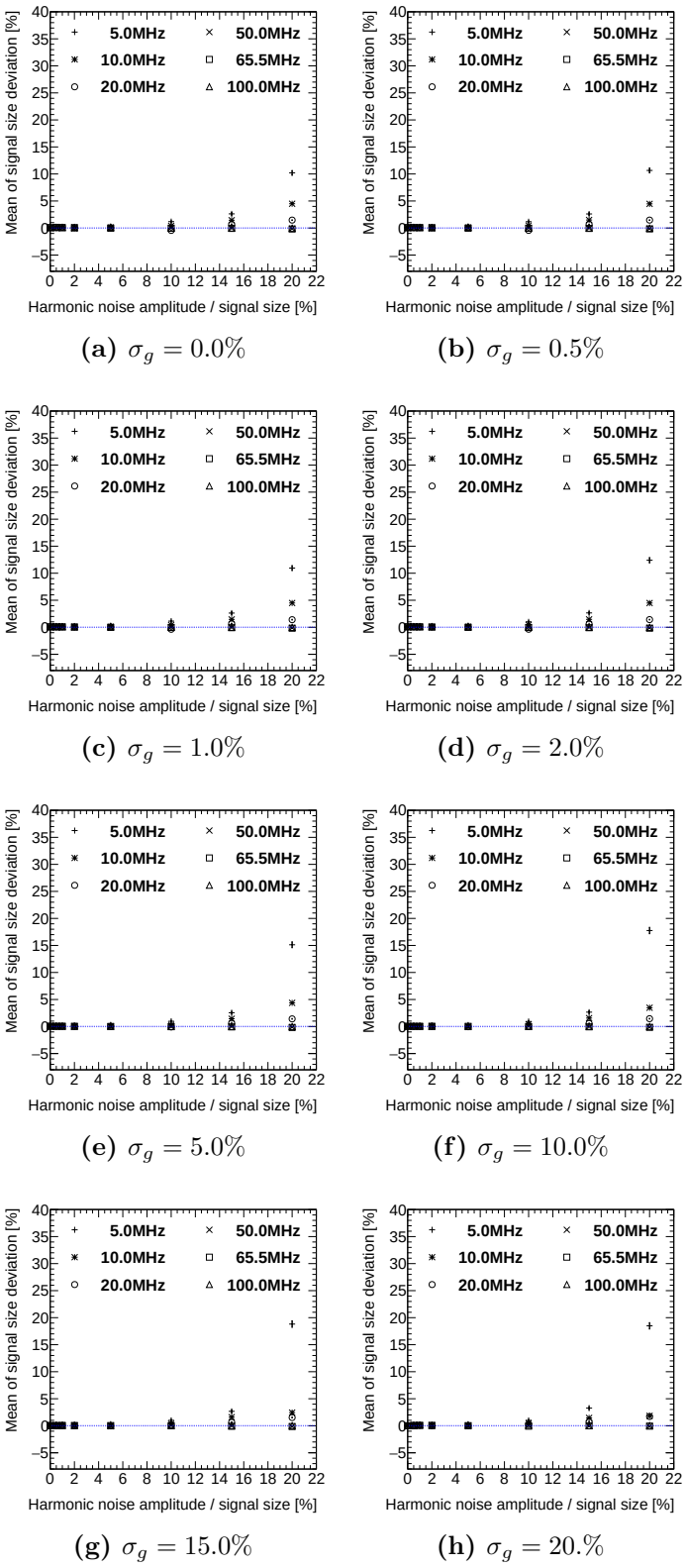


**(a)** $\sigma_g = 0.0\%$ **(b)** $\sigma_g = 0.5\%$

**(c)** $\sigma_g = 1.0\%$ **(d)** $\sigma_g = 2.0\%$

**(e)** $\sigma_g = 5.0\%$ **(f)** $\sigma_g = 10.0\%$

**(g)** $\sigma_g = 15.0\%$ **(h)** $\sigma_g = 20.\%$

**Figure A.1.** *Mean of the deviations between ideal step size and step size obtained by fit after adding Gaussian and Harmonic noise as described in section 5.2. The figures (a) to (h) represent cases of different Gaussian noise intensities from* $\sigma_g = 0.5\%$ *to* $\sigma_g = 20\%$ *of the step size.*

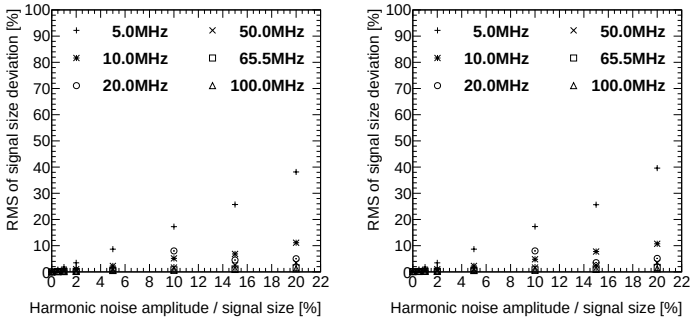


**(a)** $\sigma_g = 0.0\%$ **(b)** $\sigma_g = 0.5\%$

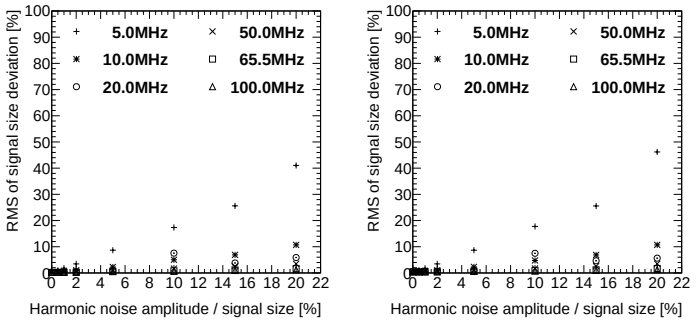


**(c)** $\sigma_g = 1.0\%$ **(d)** $\sigma_g = 2.0\%$

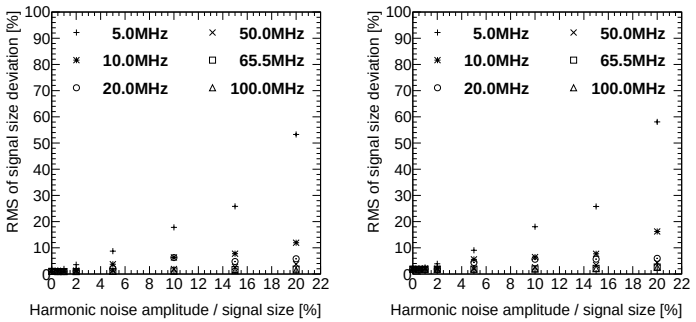


**(e)** $\sigma_g = 5.0\%$ **(f)** $\sigma_g = 10.0\%$

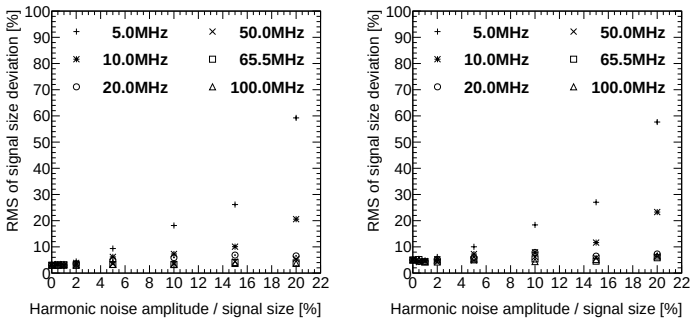


**(g)** $\sigma_g = 15.0\%$ **(h)** $\sigma_g = 20.0\%$

**Figure A.2.** *RMS of the deviations between ideal step size and step size obtained by fit after adding Gaussian and Harmonic noise as described in section 5.2. The figures (a) to (h) represent cases of different Gaussian noise intensities from* $\sigma_g = 0.5\%$ *to* $\sigma_g = 20\%$ *of the step size.*

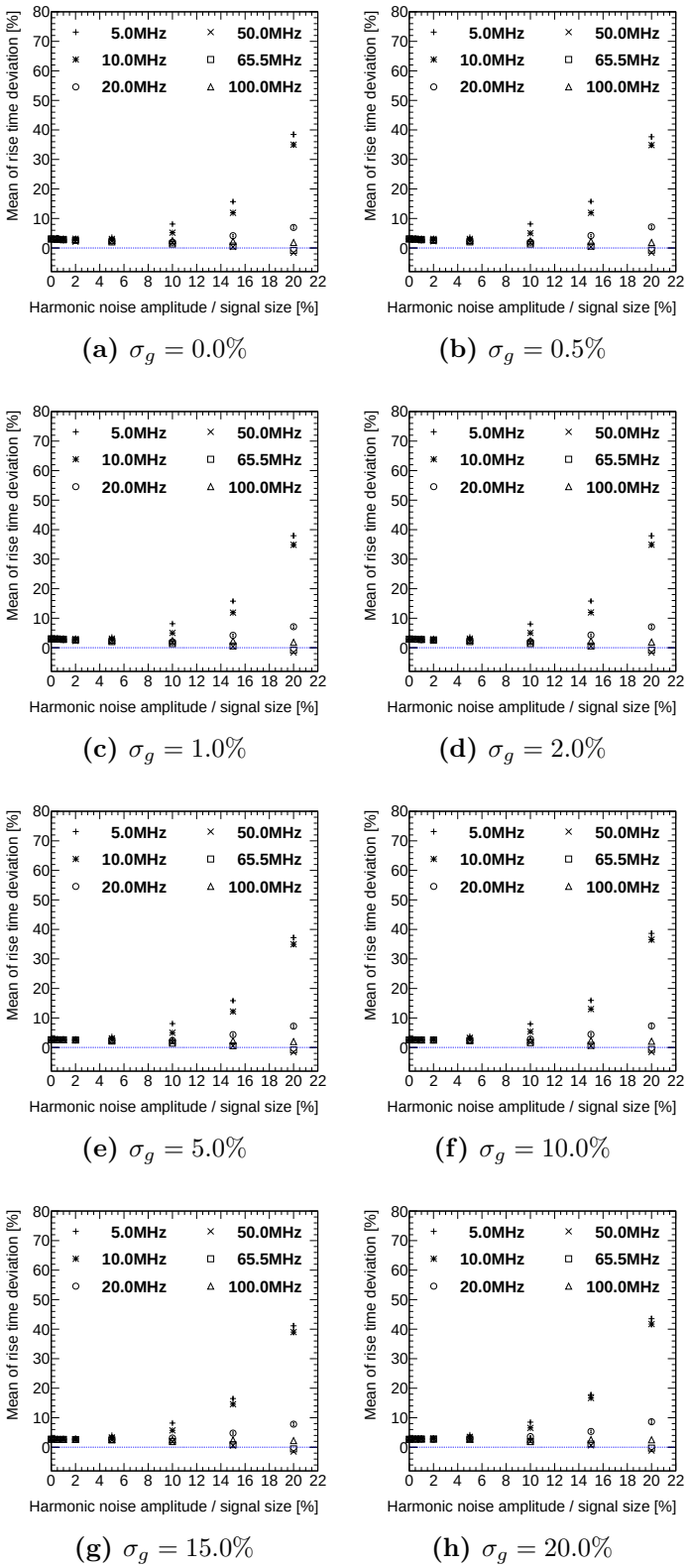


**(a)** $\sigma_g = 0.0\%$ **(b)** $\sigma_g = 0.5\%$

**(c)** $\sigma_g = 1.0\%$ **(d)** $\sigma_g = 2.0\%$

**(e)** $\sigma_g = 5.0\%$ **(f)** $\sigma_g = 10.0\%$

**(g)** $\sigma_g = 15.0\%$ **(h)** $\sigma_g = 20.0\%$

**Figure A.3.** *Mean of the deviations between ideal signal rise time and signal rise time obtained by fit after adding Gaussian and Harmonic noise as described in section 5.2. The figures (a) to (h) represent cases of different Gaussian noise intensities from $\sigma_g = 0.5\%$ to $\sigma_g = 20\%$ of the step size.*

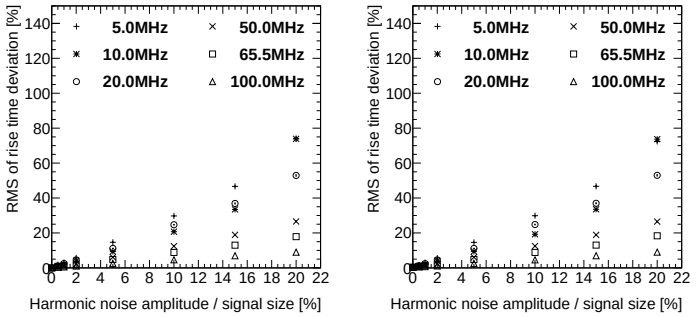


**(a)** $\sigma_g = 0.0\%$ **(b)** $\sigma_g = 0.5\%$

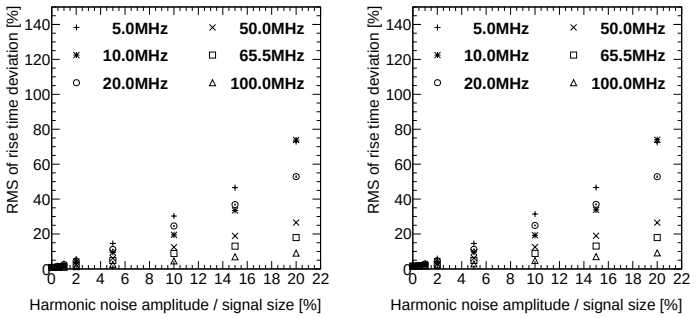


**(c)** $\sigma_g = 1.0\%$ **(d)** $\sigma_g = 2.0\%$

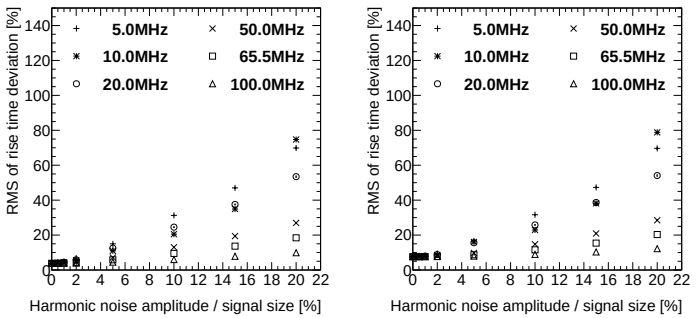


**(e)** $\sigma_g = 5.0\%$ **(f)** $\sigma_g = 10.0\%$

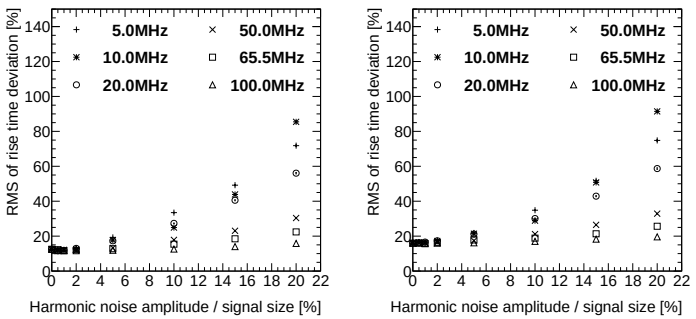


**(g)** $\sigma_g = 15.0\%$ **(h)** $\sigma_g = 20.0\%$

**Figure A.4.** *RMS of the deviations between ideal signal rise time and signal rise time obtained by fit after adding Gaussian and Harmonic noise as described in section 5.2. The figures (a) to (h) represent cases of different Gaussian noise intensities from* $\sigma_g = 0.5\%$ *to* $\sigma_g = 20\%$ *of the step size.*

*Look around just people, can you hear their voice Find the one[s] who'll guide you to the limits of your choice.*

*Enigma – Gravity Of Love*

My years at CERN which found their conclusion in this thesis were more than science. I moved to a different country, searching for a change, a next project and a direction. I was gifted with fun and curiosity, with stress and relaxation, with laughter and testbeam. There are many people who accompanied me and helped on my way. As much as I am grateful to all of them, I can only mention a few of them here.

First of all, I want to thank my supervisors. I have to thank Wolfgang Wagner for many years of guidance, advice, and an optimism even in the face of challenges. And most of all, I am grateful for his understanding and unbroken support when I revised my direction of travel. Having set a new course, I have to thank Heinz Pernegger, who forced me more than once to call people, knock on doors, and beg to make things that need three days happen in less than one. I guess you can say he taught a German how to be faster than the textbook.

Going way back to my first memories of CERN, thanks must be given to Jenny, Timon and Jens for introducing me to the IBL and to CERN, planting the seed of being an ID guy. Karo, after all those years I still discover sides of you that seem to not fit the picture and then just fit perfectly, casting a wonderful rainbow over a chainsaw-armed unipaca.

Over the time of the project, I feel like having burnt through a lot of postdocs. Malte, thank you for showing me when science needs my full attention and when I just need a full beer. Doug, all those nights at testbeam, all the dry ice refills and all the noise we couldn't understand but might one day turn out to be alien messages; it was adrenaline and it was my honour. Enrico, I still don't have the faintest understanding of the Italian way to deal with problems. I respect its success and want to thank you for all the occasions you used that skill to rescue us.

Mathieu, 10 more years and your telescope will beat world champions in chess. Thank you for your lessons during testbeam. I will always remember the important one! May the beam be with you! Sarah, you find optimism in pessimism and pessimism in optimism. And then you go to work and get things done. Thank you for your impressive enthusiasm in every situation. Bane, among all people, you've been the closest to a brother in this foreign country. I'm trying to put it in more words but I'm running blank at the end of language. Thank you.

Sven, every journey has a beginning but every day has to option to change course. Thank you for teaching me baby steps that crossed borders. Mario, having a friend like you back home always grounds me, giving rise to dreams of new adventures. Kathrin, I seem to follow you (now it's the south of Germany). It makes me smile to wonder where this might lead. James, your incredible pictures will always remind me of my time in Pays-de-Gex. Viki and Daire, having lunch with you always feels like vacation. Alex and Julia, see you on Mars! Lydia, you fight to be a successful woman in science, and with you, science is in good hands. The irony that we met in a kitchen while cooking still amuses me. Vince, you walk the earth like a playground, hunting for excitement. You don't need a cape to be a hero. If you ever need a sidekick, give me a call!

Sharing your flat can mean sharing your life and heart, creating 'home'. David, I can say that we lived the sitcom and that you entered without knocking to drink on my couch. Elisabeth, you taught me what Tartiflette and Hausfrauenwein are and that questioning pasta is futile. Bilal my friend, we laughed so often and so much, it might have saved my sanity. Jaakko, you've got a first-row seat in this drama of physicists. It was a pleasure to drag you on stage!

Life is comedy, and quite rarely has a script. Making that fact my hobby was the unhidden bless of the past years. I want to thank all Catalysts of creativity, all Sharks and their Pockets, all Renegades and all Saints. Adria, your welcoming self never ceases to attract amazing people. Thanks to Sam for the opportunity to start a community and thanks to Salvatore for filling it with life.

Thank you, Christa, for being pure inspiration. You teach me again and again that we must all aim for the focal point of our true passion. Emma, you inspire to make the earth a nicer place. I hear your call and promise to pass it on. Stuart, thank you for keeping me sane and safe and smiling when stress reached its peak. After years in France, you teach me how to be German. Pure joy and comedy on my side.

Last, I want to thank my parents and my family. Not because they are least on my list but because in addition to constantly supporting me, they always had to endure me in sight of finish line. I travel this world out of curiosity and exploration, due to always knowing where to have a home.